Doctorate Dissertation

博士論文

Development of an optical absorption measurement system to characterize KAGRA sapphire mirrors and new high-reflectivity crystalline coatings.

(KAGRA サファイア鏡及び新たな高反射性結晶コーティングの評価のための光吸収測定システムの開発)

A Dissertation Submitted for Degree of Doctor of Philosophy

December 2018

平成 30 年 12 月博士（理学）申請

Department of Astronomy, Graduate School of Science,

The University of Tokyo

東京大学大学院理学系研究科天文学専攻

Manuel Marchiò

マヌエル　マルキオ

論文の内容の要旨

Development of an optical absorption measurement system to characterize KAGRA sapphire mirrors and new high-reflectivity crystalline coatings.

(KAGRA サファイア鏡及び新たな高反射性結晶コーティングの評価のための光吸収測定システムの開発)

Manuel Marchiò
マヌエル　マルキオ

Abstract

KAGRA is the Japanese interferometric gravitational wave detector. It employs sapphire test masses and operates at cryogenic temperatures to reduce mirror thermal noise. Sapphire substrates optical absorption needs to be minimized to reduce the heat deposited in the mirrors and to make the cryogenic operation possible.

We developed and tested an optical absorption measurement system based on the so-called Photo-thermal Common-path Interferometer (PCI) technique: a high-power laser at 1064 nm periodically heats up the sample that we want to test; then a probe laser at 633 nm crosses the sample, and it is used to measure the absorption rate inside and on the surface of the sample.

For a better understanding of the system, its calibration, and alignment, we made some numerical simulations that reproduce the absorption signal readout. The simulations results are in good agreement with the measurements and can predict the absorption signal behavior when changing the experimental parameters.

We further improved the setup by designing, assembling and testing an upgraded version of the system. We set a large translation stage to measure KAGRA sapphire mirrors (22 cm in diameter and 15 cm in thickness). We made maps and studied the absorption structures inside the sapphire substrates. The sensitivity on sapphire bulks is better than 2 ppm/cm and the calibration is compliant with other laboratories. We are now able to measure the absorption continuously along the depth of the sample and to make 3D absorption maps. We found interesting absorption structures inside the crystal. This new information will help the maker to improve the quality of future sapphire crystals.

For future upgrades of KAGRA, high-reflectivity substrate-transferred AlGaAs crystalline coatings have been proposed. This new type of coatings will contribute to reducing the coating thermal noise, which is currently a limitation at mid frequencies in the sensitivity curve.

In order to investigate the possibility to apply this new material to KAGRA, we characterized the optical performances of new large-area (2 inches-diameter) AlGaAs crystalline coatings. To measure the absorption map of the coating, we assembled and tested an additional infrared probe (1310 nm) in our PCI system, reaching a sensitivity better than 0.2 ppm. We found that the crystalline coating absorption is very uniform except some point defects. In collaboration with CNRS/LMA, we measured absorption, transmission, defects number, scattering maps, and surface roughness. We measured 2 samples, one is AlGaAs transferred on a fused silica substrate, and the other is AlGaAs transferred on a sapphire substrate. The coatings show excellent optical performances, in particular, the absorption (below 1 ppm) and the scattering (below 10 ppm) fulfill the requirements for KAGRA, but the defects number is higher than current amorphous coatings. In collaboration with MIT, we did a direct thermal noise measurement at room temperature. The result is that the crystalline coating thermal noise is a factor of 2 lower than the amorphous coatings used in present gravitational wave detectors.

Contents

Abstract i

Contents vi

Abbreviations vii

Introduction 3

1 Theory and experiments of gravitational wave detection 5

1.1 Gravitational waves theory 5

1.1.1 The metric tensor and the Einstein equations 5

1.1.2 The linearized theory of gravity 6

1.1.3 Propagation of gravitational waves 7

1.1.4 Generation of gravitational waves 9

1.2 Sources of gravitational waves 10

1.2.1 Neutron stars 10

1.2.2 Binary systems 10

1.2.3 Supernovae 11

1.2.4 Stochastic background 13

1.3 Interferometric detectors 13

1.3.1 Simple Michelson 13

1.3.2 Fabry-Pérot cavity 15

1.3.3 Power recycling 17

1.4 Noise sources 18

1.4.1 Shot noise 19

1.4.2 Radiation pressure noise 20

1.4.3 Seismic noise 22

1.4.4 Newtonian noise 22

1.4.5 Thermal noise 23

1.5 Detectors network . . . 29
1.5.1 First generation gravitational wave detectors . . . 29
1.5.2 Second generation gravitational wave detectors . . . 30

2 KAGRA **35**
2.1 Detector configuration . . . 36
2.2 KAGRA cryogenic operation . . . 37
2.2.1 Thesis motivation: sapphire absorption . . . 40
2.3 R&D for KAGRA . . . 41
2.3.1 Sensitivity improvement . . . 42
2.3.2 Thesis motivation: crystalline coatings . . . 43

3 Optical absorption measurement system **45**
3.1 Introduction . . . 45
3.2 Working principle of the PCI . . . 46
3.2.1 Simple model . . . 47
3.3 Experimental setup . . . 50
3.3.1 Alignment procedures . . . 53
3.4 Calibration . . . 53
3.5 Thick sample issues . . . 54
3.6 Absorption test measurements . . . 58
3.6.1 LMA Samples . . . 58
3.6.2 Sapphire sample . . . 61
3.7 Noise . . . 64
3.8 Numerical simulations . . . 66
3.8.1 Temperature distribution . . . 66
3.8.2 Optical simulation . . . 74
3.8.3 Sample scan . . . 77
3.9 Simulation results and applications . . . 77
3.9.1 Comparison with the measurements . . . 77
3.9.2 Parameters variations . . . 78
3.9.3 Prediction of calibration factor for thin GaAs samples . . . 81
3.10 Conclusions . . . 83

4 Experimental setup upgrade **85**
4.1 Large translation stage . . . 85
4.2 Setup design . . . 86

4.3 Laser beams profile . . . 87
4.4 Pump reflections . . . 90
4.5 Demodulation and measurement control . . . 91
4.6 Alignment and calibration . . . 93
4.7 Noise . . . 98
4.7.1 Chopper vibrations . . . 98
4.7.2 Probe reflection . . . 98
4.7.3 Cleanness . . . 98
4.7.4 Airflow . . . 99
4.7.5 1310 nm probe intensity stabilization . . . 99
4.8 Calibration validation . . . 101
4.9 Conclusion . . . 103

5 Sapphire absorption measurements 101
5.1 Sapphire . . . 101
5.2 Samples . . . 102
5.3 Absorption measurements . . . 102
5.3.1 Calibration . . . 103
5.3.2 Small size substrate . . . 103
5.3.3 Tama300 mirror size substrate . . . 107
5.3.4 KAGRA test mass substrate . . . 112
5.3.5 Discussion and conclusions . . . 119

6 Crystalline high-reflectivity coatings characterization 121
6.1 Introduction . . . 121
6.2 Large-area crystalline coatings . . . 123
6.3 Absorption measurements . . . 124
6.3.1 Measured at LMA . . . 124
6.3.2 Measured with PCI at NAOJ . . . 127
6.3.3 Discrepancy between LMA and NAOJ results . . . 127
6.4 Optical characterization measurements . . . 132
6.4.1 Transmission . . . 132
6.4.2 Scattering . . . 133
6.4.3 Roughness . . . 134
6.5 Thermal noise measurement . . . 139
6.5.1 Working principle . . . 139

6.5.2 Experimental setup 140
6.5.3 Noises 143
6.5.4 Results 144
6.5.5 Future plan for the estimation of coating thermal noise 146
6.6 Conclusion 149

Conclusions **152**

Bibliography **153**

Abbreviations

GR	**G**eneral **R**elativity
TT	**T**ransverse-**T**raceless gauge
GW	**G**ravitational **W**ave
FSR	**F**ree **S**pectral **R**ange
FWHM	**F**ull **W**idth at **H**alf **M**aximum
MI	**M**ichelson **I**nterferometer
FP	**F**abry-**P**érot
FPMI	**F**abry-**P**érot **M**ichelson **I**nterferometer
PR	**P**ower **R**ecycling
PSD	**P**ower **S**pectral **D**ensity
PD	**P**hoto **D**iode
SNR	**S**ignal to **N**oise **R**atio
QL	**Q**uantum **L**imit
RMS	**R**oot **M**ean **S**quare
LCGT	**L**arge **C**ryogenic **G**ravitational **T**elescope
IM	**I**ntermediate **M**ass
TM	**T**est **M**ass
ITM	**I**nput **T**est **M**ass
ETM	**E**nd **T**est **M**ass
BBH	**B**inary **B**lack **H**hole
BNS	**B**inary **N**eutron **S**tar
NAOJ	**N**ational **A**stronomical **O**bservatory of **J**apan

LMA	**L**aboratoire des **M**atériaux **A**vancés
BRSE	**B**roadband **R**esonant **S**ideband **E**xtraction
DRSE	**D**etuned **R**esonant **S**ideband **E**xtraction
PCI	**P**hoto-thermal **C**ommonpath **I**nterferometer
SPTS	**S**tanfor **P**hoto-**T**hermal **S**olutions (Company)
CMS	**C**rystalline **M**irror **S**olutions (Company)
OD	**OD** **O**ptical **D**ensity
PBS	**P**olarizing **B**eam **S**plitter
OPL	**O**ptical **P**ath **L**ength
VI	**V**irtual **I**nstrument (LabVIEW)

Introduction

Gravitational waves were predicted by Albert Einstein in the context of General Relativity. According to this theory, accelerating masses generate ripples in the space-time that propagate at the speed of light. The most intense gravitational waves are those coming from violent astronomical events. However, even the strain produced by these waves is extremely tiny, of the order of 10^{-21}. It took a great effort to realize detectors that are sensitive enough to observe a gravitational wave. On September 14th, 2015, the two Advanced LIGO detectors observed for the first time a gravitational wave from the coalescence and merger of a binary black hole [1]. This detection marked the beginning of a new era for astronomy. Later, the detector Advanced Virgo joined the second generation network. On August 16th, 2017 the three detectors (the two Advanced LIGO and Advanced Virgo) detected for the first time the gravitational wave emitted during the inspiral and merger of a binary neutron star. Thanks to the observations of the electromagnetic counterpart, an impressive amount of scientific information has been produced. Increasing the number of detectors improves the signal-to-noise ratio and the localization precision.

KAGRA is the Japanese interferometric gravitational wave detector. To reduce mirror thermal noise it operates at cryogenic temperatures (20K) and to reduce seismic noise it is built underground. It employs sapphire test masses because of its good thermal conductivity and excellent mechanical quality factor at low temperature. Sapphire substrates optical absorption needs to be minimized to reduce the heat deposited in the mirrors and to make the cryogenic operation possible.

During this thesis work, we developed and tested an optical absorption measurement system to characterize KAGRA sapphire mirrors. The system is based on the so-called Photo-thermal Common-path Interferometer (PCI) technique, where there is a pump laser that heats up the sample, and a probe laser that senses the temperature change due to the absorption.

Current detectors employ dielectric SiO_2/Ta_2O_5 multilayer high-reflectivity coatings. The coating thermal noise is a limitation at mid frequencies in the sensitivity

curve. For future upgrades of KAGRA, high-reflectivity substrate-transferred epitaxial multilayers based on single-crystal GaAs/AlGaAs heterostructures have been proposed. This new type of coatings has already demonstrated significant reductions in the mechanical loss. However, fabrication of such coatings is a technological challenge because they require extremely high material purity, excellent surface quality, low absorption, low total integrated scattering, below 10 ppm, and large coating diameters. The absorption should be below 1 ppm to keep the heat deposited in the mirrors in the range of 1W or less thus allowing operation at low temperature in a cryogenic interferometer like KAGRA. During this thesis work, we characterized the optical performance of the first large-area (5 cm diameter) crystalline coatings. The results of this characterization were published in the paper "Optical performance of large-area crystalline coatings" on Optics Express [2]. To measure the absorption we assembled and tested an additional infrared probe in our PCI system, reaching a sensitivity better than 0.2 ppm. In collaboration with CNRS/LMA and MIT, we also measured transmission, defects number, scattering maps, roughness, and thermal noise. This characterization was carried out to understand the current state of the technology and to provide motivation for further developments.

In Chapter 1, starting from the basics of the theory of general relativity, we briefly present the derivation of the gravitational radiation from the Einstein equations. We list the main astronomical gravitational waves sources, and the respectively expected gravitational wave signals. The working principles of interferometric detectors are explained, and some of the techniques used to improve their measurement precision are presented. We list the most important noise limitations to the sensitivity of the interferometers. Some information about the existing detectors and about the recent first detections performed by the network of interferometers are provided.

In Chapter 2, we summarize the features of KAGRA. We focus on the motivations for this thesis work. We give details about the cryogenic system and about the absorption requirements for the sapphire substrates. We introduce the research ongoing for the improvement of the KAGRA sensitivity, in particular, the R&D work on high-reflective crystalline coating done during this Ph.D. thesis. Then we estimate the improvement of the KAGRA sensitivity, once this new technology will be implemented in KAGRA.

In Chapter 3, we describe the working principle, the experimental details, and some first results of the initial setup of the PCI absorption measurement system. We report about the numerical simulations performed in order to deeply understand the setup, and optimize the parameters to get the best absorption signal.

In Chapter 4, we describe the upgrade of the original PCI setup: the large translation stage assembled to measure the large KAGRA sapphire substrates (22 cm in diameter and 15 cm in thickness); and the additional infrared probe laser installed to measure the new AlGaAs crystalline coatings. We report the details on the upgrade development, the main problems we encountered and the solutions we adopted.

In Chapter 5, we report the result of the absorption measurements that we did on several sapphire substrates using our setup. We list the measured sapphire substrate. We report the absorption measurement maps of the substrates. We study the absorption structures found in the samples.

In Chapter 6, we present an R&D work aimed to reduce thermal noise in high-reflectivity coatings for future upgrades of KAGRA. We describe the novel crystalline coatings based on GaAs/AlGaAs multilayer structure. We report the results of the absorption measurements that we did at LMA using a photo-deflection method, and at NAOJ using the PCI setup developed in this Ph.D. Thesis and described in Chapter 4. We present the optical performance measurements that we did in collaboration with LMA. Finally, we present the result of the direct thermal noise measurement that we did at MIT using an optical bench developed there for this purpose.

Chapter 1

Theory and experiments of gravitational wave detection

The first two chapters of this thesis are an introduction to the theory of gravitational waves and of the interferometric detectors. The first section of this chapter is a brief introduction to Einstein's theory of gravitation. The second section is a list of the main astronomical gravitational waves sources and the respectively expected gravitational wave signals. In the third section, the basics of interferometric detectors are explained, and some of the techniques used to improve their measurement precision are presented. The fourth section is a list of the most important noise limitations to the sensitivity of the interferometers. In the last section, some information about the existing detectors and about the recent first detections performed by the network of interferometers are provided.

1.1 Gravitational waves theory

In this section, starting from the definition of the metric tensor, and using the formalism of the General Relativity, we present the main equations that bring to the prediction of the gravitational radiation.

1.1.1 The metric tensor and the Einstein equations

The theory of General Relativity describes the spacetime as a 4-dimensions manifold where the distance between two points x^μ and $x^\mu + dx^\mu$ is

$$ds^2 = g_{\mu\nu} dx^\mu dx^\nu \tag{1.1}$$

where $g_{\mu\nu}$ is the metric tensor, $(\mu, \nu) = 0, 1, 2, 3$, and the Einstein summation convention for repeated indexes is used. For a space without masses, the metric tensor is the flat Minkowski metric $\eta_{\mu\nu} = \text{diag}(-1, 1, 1, 1)$.
Einstein stated that the presence of masses curves the spacetime. This understanding of gravity turns the gravitational force to a geometrical fact. A free falling object, which experiences the gravitational force only, moves along the straightest path in the curved spacetime. This motion is the solution of the geodesic equations

$$\frac{d^2x^\alpha}{d\tau^2} + \Gamma^\alpha{}_{\mu\gamma}\frac{dx^\mu}{d\tau}\frac{dx^\gamma}{d\tau} = 0 \tag{1.2}$$

where τ is the proper time in the local frame where the object moves, and Γ are the affine connections or Christoffel symbols which can be expressed as a combination of the metric tensor and its derivatives as

$$\Gamma^\alpha{}_{\beta\gamma} = \frac{1}{2}g^{\alpha\mu}\left(\frac{\partial g_{\mu\beta}}{\partial x^\gamma} + \frac{\partial g_{\mu\gamma}}{\partial x^\beta} - \frac{\partial g_{\beta\gamma}}{\partial x^\mu}\right). \tag{1.3}$$

These equations can describe the motion of the suspended test masses of an interferometer because they are considered as free falling masses along the horizontal plane. The test masses are used to detect gravitational wave. The starting point of the derivation of the effect of GWs on the test masses are the Einstein Field Equations:

$$R_{\mu\nu} - \frac{1}{2}g_{\mu\nu}R = \frac{8\pi G}{c^4}T_{\mu\nu} \tag{1.4}$$

which relate the spacetime curvature with the mass and energy. On the right-hand side of Equation 1.4, G is the gravitational constant, c is the speed of light and $T_{\mu\nu}$ is the Stress-Energy tensor. On the left-hand side, the Ricci tensor $R_{\mu\nu}$ and the scalar curvature R are contractions of the Riemann tensor: $R_{\mu\nu} \equiv R^\alpha{}_{\mu\alpha\nu}$ and $R \equiv R^\mu{}_\mu$. The Riemann tensor can be expressed as a combination of the Christoffel symbols and their derivatives

$$R^\alpha{}_{\beta\gamma\delta} = \frac{\partial\Gamma^\alpha{}_{\beta\delta}}{\partial x^\gamma} - \frac{\partial\Gamma^\alpha{}_{\beta\gamma}}{\partial x^\delta} + \Gamma^\alpha{}_{\mu\gamma}\Gamma^\mu{}_{\beta\delta} - \Gamma^\alpha{}_{\mu\delta}\Gamma^\mu{}_{\beta\gamma} \tag{1.5}$$

1.1.2 The linearized theory of gravity

In the case of weak-field the metric tensor $g_{\mu\nu}$ can be written in the form

$$g_{\mu\nu} = \eta_{\mu\nu} + h_{\mu\nu} \tag{1.6}$$

where $h_{\mu\nu}$ is a small perturbation $|h_{\mu\nu}| \ll 1$ of the flat Minkowski metric $\eta_{\mu\nu}$. The non-linear Einstein Field Equations can thus be expanded in powers of $h_{\mu\nu}$ keeping only the linear terms. The linearized Christoffel symbols are

$$\Gamma^{\mu}{}_{\alpha\beta} = \frac{1}{2}\eta^{\mu\nu}\left(\frac{\partial h_{\alpha\nu}}{\partial x^{\beta}} + \frac{\partial h_{\beta\nu}}{\partial x^{\alpha}} - \frac{\partial h_{\alpha\beta}}{\partial x^{\nu}}\right) \tag{1.7}$$

and the Ricci tensor becomes

$$R_{\mu\nu} = \frac{1}{2}\left(\frac{\partial^2 h_{\mu}{}^{\alpha}}{\partial x^{\nu}\partial x^{\alpha}} + \frac{\partial^2 h_{\nu}{}^{\alpha}}{\partial x^{\mu}\partial x^{\alpha}} - \frac{\partial^2 h_{\nu\nu}}{\partial x^{\alpha}\partial x_{\alpha}} - \frac{\partial^2 h}{\partial x^{\mu}x^{\nu}}\right) \tag{1.8}$$

where $h \equiv h^{\alpha}{}_{\alpha} = \eta^{\alpha\beta}h_{\alpha\beta}$.

Defining

$$\bar{h}_{\mu\nu} \equiv h_{\mu\nu} - \frac{1}{2}\eta_{\mu\nu}h \tag{1.9}$$

and imposing the Lorenz gauge

$$\frac{\partial \bar{h}^{\mu\nu}}{\partial x^{\alpha}} = 0 \tag{1.10}$$

the linearized field equations become

$$\frac{\partial^2 \bar{h}_{\mu\nu}}{\partial x^{\alpha}\partial x_{\alpha}} = -\frac{16\pi G}{c^4}T_{\mu\nu} \tag{1.11}$$

1.1.3 Propagation of gravitational waves

In vacuum, $T_{\mu\nu} = 0$ and, in the Lorenz gauge, the propagation equations for gravitational fields are the wave equations

$$\Box\bar{h}_{\mu\nu} \equiv \frac{\partial^2 \bar{h}_{\mu\nu}}{\partial x^{\alpha}\partial x_{\alpha}} = 0 \tag{1.12}$$

where $\Box$ is the d'Alembert operator.

The simplest solution to the linearized equations 1.12 is the monochromatic, plane-wave solution

$$\bar{h}_{\mu\nu} = \mathrm{Re}\left[A_{\mu\nu}e^{ik_{\alpha}x^{\alpha}}\right] \tag{1.13}$$

where the amplitude $A_{\mu\nu}$ and the wave vector k_{μ} satisfy

$$k_{\alpha}k^{\alpha} = 0 \tag{1.14}$$

$$A_{\mu\alpha}k^{\alpha} = 0 \tag{1.15}$$

which means that the solution is a transverse wave propagating at the speed of light. The Lorenz condition doesn't completely fix the gauge. Indeed, under a transformation

$$x^\mu \to x^\mu + \xi^\mu, \qquad |\xi| \ll 1, \qquad \Box\xi_\mu = 0 \tag{1.16}$$

$\bar{h}$ preserves the Lorenz condition and the tensor form as

$$\bar{h}_{\mu\nu} \to \bar{h}'_{\mu\nu} = \bar{h}_{\mu\nu} - \left(\frac{\partial \xi_\nu}{\partial x^\mu} + \frac{\partial \xi_\mu}{\partial x^\nu} - \eta_{\mu\nu} \frac{\partial \xi^\rho}{\partial x^\rho} \right). \tag{1.17}$$

So it's possible to choose a coordinate transformation ξ_μ in order to have

$$h^{0\mu} = 0, \qquad h^i{}_i = 0, \qquad \frac{\partial h_{ij}}{\partial x^j} = 0 \tag{1.18}$$

where Latin indexes run on the spatial components of the tensor. The gauge choice 1.18 is called the *transverse-traceless gauge* (TT). Note that since the trace $h = 0$, then $\bar{h}_{\mu\nu} = h_{\mu\nu}$. In the TT gauge the metric tensor takes the form

$$h^{TT}_{\mu\nu} = \begin{pmatrix} 0 & 0 & 0 & 0 \\ 0 & h_+ & h_\times & 0 \\ 0 & h_\times & -h_+ & 0 \\ 0 & 0 & 0 & 0 \end{pmatrix} \cos[\omega(t - z/c)] \tag{1.19}$$

where h_+ and $h_\times$ represent the two polarizations of a gravitational wave. Figure 1.1

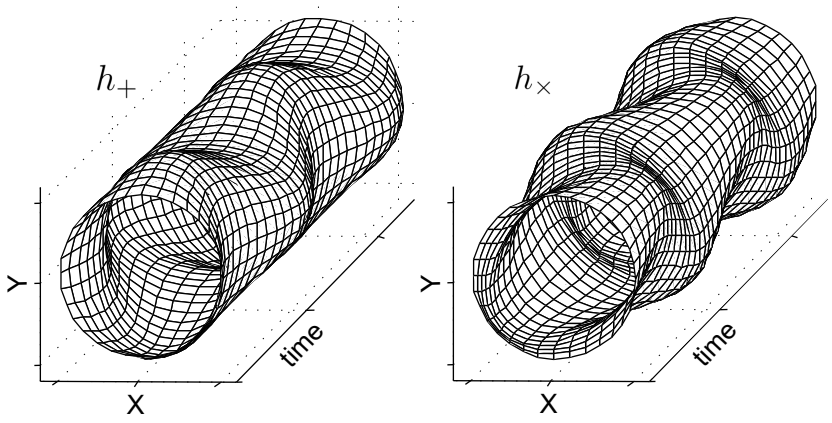

Figure 1.1: A graphical representation of the two polarizations of a gravitational wave: h_+ and $h_\times$. How a wave traveling perpendicular to the (x,y) plane changes the distances between a set of point arranged on a circle.

shows how the distances between a ring of points in the (x,y) plane change in time when a gravitational wave propagates along the z-axis.

Solving the geodesic Equation 1.2 in the TT frame, it turns out that a particle which was at rest before the arrival of the wave remains at rest even after the arrival of the wave. Physical effect can be detected monitoring the proper distances between objects. Considering for instance to events at $(t, x_1, 0, 0)$ and at $(t, x_2, 0, 0)$, the coordinate distance in the TT frame is $x_2 - x_1 = L$, which remains constant, but the proper distance is

$$s = (x_2 - x_1)[1 + h_+ \cos(\omega t)]^{1/2} \simeq L[1 + \frac{1}{2} h_+ \cos(\omega t)] \tag{1.20}$$

which is the quantity measured by gravitational wave detectors.

1.1.4 Generation of gravitational waves

The gravitational wave sources are usually small compared to the wavelength of the GWs they generate. Therefore, in the weak field approximation, and far from the source, we can write the solution to Equation 1.11 as a function of the retarded time

$$\bar{h}_{\mu\nu}(t, \vec{x}) = \frac{4G}{c^4} \int d^3x' \frac{1}{|\vec{x} - \vec{x}'|} T_{\mu\nu} \left(t - \frac{|\vec{x} - \vec{x}'|}{c}, \vec{x}' \right) \tag{1.21}$$

The gravitational radiation can be expanded in multipoles . The absence of negative masses, the conservation of momentum and the conservation of angular momentum, forbid the emission of mass monopole and mass dipole radiation. The first radiation permitted is the mass quadrupole one. Defining the mass quadrupole moment as

$$I_{jk} = \int T^{00} \left(x^j x^k - \frac{1}{3} \delta_{jk} r^2 \right) d^3x \tag{1.22}$$

we can express Equation 1.21 as

$$h^{TT}_{jk}(t, \vec{x}) = \frac{2G}{c^4 |\vec{x}|} \frac{d^2 I^{TT}_{jk}(t - |\vec{x}|)}{dt^2}) \tag{1.23}$$

The factor $G/c^4 \simeq 8 \times 10^{-45}\,\mathrm{s^2/kg\,m}$ is very tiny, so even large moving masses generate weak gravitational waves. For example, two masses of $10^3\,\mathrm{kg}$ each, $2\,\mathrm{m}$ distant, rotating at $f = 1\,\mathrm{kHz}$, would generate a wave with amplitude

$$h \simeq \frac{10^{-33}\,\mathrm{m}}{R} \tag{1.24}$$

where R should be at least one wavelength, $\lambda = 300\,\mathrm{km}$ in this case. Which gives $h \simeq 10^{-39}$ several orders of magnitude below the sensitivity of current ground-based detectors. For this reason, only gravitational waves produced by astronomical events involving huge masses are detectable.

1.2 Sources of gravitational waves

Astronomical sources are classified in three categories according to the time evolution of the gravitational waves they emit. Periodic sources, like spinning neutron stars or binary systems of neutron stars or black holes; impulsive sources, like bursts, supernovae, merging systems; and stochastic background.

1.2.1 Neutron stars

Fast spinning neutron stars emit gravitational waves as long as their mass distribution is asymmetric around the rotation axis. The signal is a monochromatic continuous wave. In the case of pulsars, the frequency is known from the radio astronomy observation, so processing the two signals together would improve the signal to noise ratio. The gravitational wave amplitude expected from a spinning neutron star is

$$h \simeq 3 \cdot 10^{-25} \cdot \left(\frac{\epsilon}{10^{-6}}\right) \left(\frac{I}{10^{-38}\mathrm{kg}\cdot\mathrm{m}^2}\right) \left(\frac{f}{1\,\mathrm{kHz}}\right)^2 \left(\frac{10\,\mathrm{kpc}}{R}\right) \tag{1.25}$$

were I is the moment of inertia and ϵ is the ellipticity that parameterizes the mass distribution asymmetry. The gravitational wave frequency is twice the pulsar spin frequency. The amplitude value resulting from Equation 1.25 is quite below the current sensitivity of ground-based detectors, but since the signal is continuous, it is possible to improve the signal to noise ratio by integrating on time.

1.2.2 Binary systems

Binary systems are well known objects in astronomy. At the end of the stellar evolution, those pairs of stars can become a compact binary system. The systems that are most likely to emit detectable gravitational waves can be composed by two neutron stars (NS-NS), two black holes (BN-BN) or a neutron star and a black hole (BH-NS). Initially, the orbital motion is slow and the gravitational wave emission is outside the sensitivity range of ground-based detectors. The strain amplitude of

the gravitational waves at a distance r from the source is:

$$h \simeq 10^{-21} \cdot \left(\frac{\mathcal{M}}{M_\odot}\right)^{5/6} \left(\frac{f}{100\,\mathrm{Hz}}\right)^{5/6} \left(\frac{r}{15\,\mathrm{Mpc}}\right)^{-1} \tag{1.26}$$

Where $\mathcal{M}$ is the the chirp Mass defined as $\mathcal{M} = \mu^{2/3} M^{2/5}$, where $\mu = \frac{m_1 m_1}{m_1 + m_2}$ is the reduced mass, and $M = m_1 + m_2$ is the total mass.
By the emission of gravitational radiation, the orbital energy decreases at a rate of

$$\frac{dE}{dt} = \frac{c^3}{16\pi\, G} \int \left|\frac{dh}{dt}\right| \mathrm{d}S = \frac{1}{5}\frac{G}{c^5}\frac{d^3Q^{ij}}{dt^3}\frac{d^3Q^{ij}}{dt^3}, \tag{1.27}$$

so the two bodies start spiralling around each other. A graphic representation of this event is shown in Figure 1.2. In this phase, the gravitational signal has a characteristic shape called chirp, shown on Figure 1.3, where the signal amplitude and frequency increase with time. Such systems are expected to emit the strongest gravitational waves detectable from Earth. The wave frequency, that is the double of the orbital frequency, increases with time as

$$f = \frac{5}{8\pi}\left(\frac{c^3}{G\mathcal{M}}\right)^{5/8} (t_c - t)^{-3/8} \tag{1.28}$$

The binary system eventually merges into a single compact object that is rotating and still emitting gravitational waves. In this phase, called the ring-down, there are asymmetries in the mass distribution that still generate gravitational waves. Gravitational energy is released and the mass deformations gradually stabilize until it is not detectable anymore.

1.2.3 Supernovae

Type II supernovae are produced by the gravitational core collapse of massive stars. During the evolution of the star, when the iron core exceeds the Chandrasekhar mass of about $1.4\,M_\odot$, the electron degeneracy pressure is no longer able to bear the gravitational compression, so the core matter is transformed into neutrons and the star collapses. When the density increases too much, the collapse turns into a bounce. If the collapsing is not symmetric, the change in the mass quadrupole moment generates gravitational waves. Asymmetries can arise because of both convective instabilities and rotation. Since the physics of the process is extremely complicated and still not well understood, it is difficult to have precise estimations

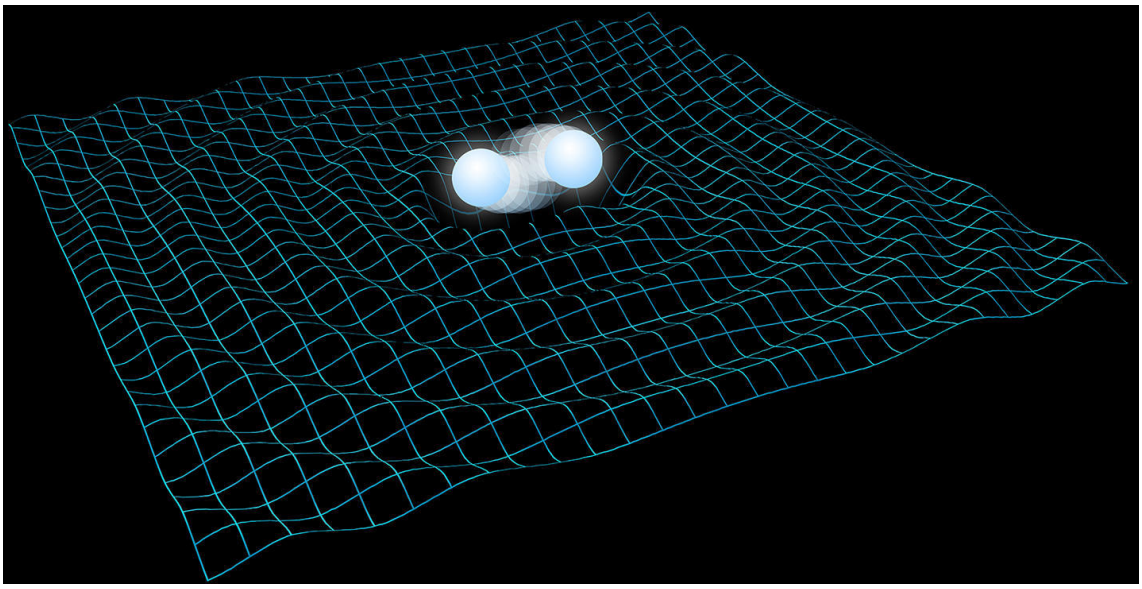

Figure 1.2: Artistic representation of two compact stars merging together with gravitational wave emission. © NAOJ

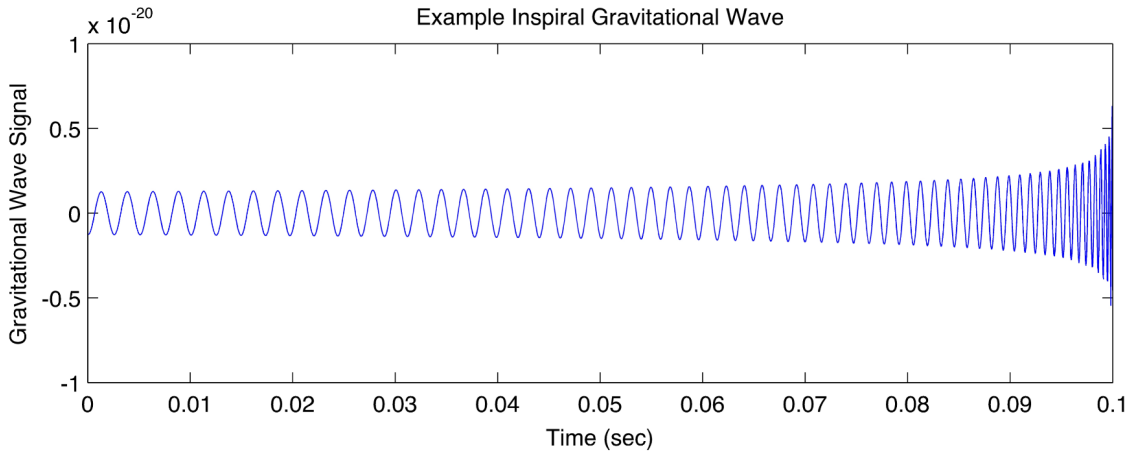

Figure 1.3: An example signal from an inspiral gravitational wave source. [Image: A. Stuver/LIGO]

for the evolution of the quadrupole moment of the system. Recent models predict a gravitational wave strain in the range $4 \times 10^{-25} \leq |h^{TT}| \leq 4 \times 10^{-23}$ or a source at a distance of 10 Mpc. The spectra cover a frequency range from 50 Hz to 3 kHz, with most of the power being emitted between 500 Hz and 1 kHz [3].

1.2.4 Stochastic background

A large number of binary systems in our galaxy produces a stochastic background of gravitational waves. Space-based detectors are expected to detect that signal as a "background noise". Another source of the stochastic signal is a superposition of the gravitational waves originated in the cosmological phenomena such as the fluctuations of the space-time in the early Universe. Detection of a stochastic background generally involves cross-correlation between observations by several detectors. Analyses of the stochastic background have been performed using terrestrial interferometric gravitational wave detectors and the measurements provide restrictions and upper limits to several theories on cosmological gravitational wave sources.

1.3 Interferometric detectors

There are many methods to detect gravitational waves, like resonant bars, pulsar timing, or Sagnac interferometers, but the dual-recycled Fabry-Pérot Michelson interferometers are the most suitable in terms of achievable sensitivity and affordable technology. This section is an introduction to the basic of interferometric detectors. Starting from the simple Michelson model, we introduce the optical configuration of current typical detectors, which are dual-recycled Fabry-Pérot Michelson interferometers.

1.3.1 Simple Michelson

The simplest Michelson interferometer consists of a laser beam, a beam splitter, two end mirrors, and a detector. The laser is separated in two beams by the beam splitter. Each of the two beams travels along each arm (x and y) of the interferometer, it is reflected back by the end mirror, and gets a phase shift according to the optical path length. The two beams superpose at the beam splitter, and a part goes to a photo-detector. If we write the laser beam electric field as $E_0 e^{i(2\pi ft)}$, and assuming

the beam splitter to perfectly divide the beam into two equal parts, the electric field on the photo-detector can be written as:

$$\begin{aligned} E_{\mathrm{PD}} &= \frac{E_0}{2} e^{i(2\pi f t - 2kL_x)} + \frac{E_0}{2} e^{i(2\pi f t - 2kL_y)} \\ &= E_0 e^{i(2\pi f t - 2kL_x - kL_y)} \cos[kL_x - kL_y] \end{aligned} \tag{1.29}$$

where L_x and L_y are the arms lengths. So the power is

$$P_{\mathrm{PD}} = |E_{\mathrm{PD}}|^2 = \frac{E_0^2}{2}(1 + \cos[2(kL_x - kL_y)]) = \frac{P_{in}}{2}(1 + \cos\phi) \tag{1.30}$$

The signal is the result of the interference between the two beams, and it is sensitive to the relative arm length change. In principle, if the noise is small enough, this setup can measure gravitational waves because, when a wave passes, the arms' length changes in the laboratory reference frame, as shown in Equation 1.20.
The phase the light accumulates during a round trip in each arm in presence of a gravitational signal h is given by

$$\phi_{x,y} = 2\pi f \tau_{x,y} = 2\pi f \left(\frac{2L_{x,y}}{c} +, - \int_{t-2L_{x,y}/c}^{t} \frac{1}{2} h(t') dt' \right) \tag{1.31}$$

The phase difference between the two arms is

$$\Delta\phi_{GW} = \phi_x - \phi_y = 2\pi f \int_{t-2L/c}^{t} h(t') dt' \tag{1.32}$$

where $L \simeq L_x \simeq L_y$, and it is observed measuring the interference pattern on the photo-detector. Taking the Fourier transform of 1.32 we can calculate the frequency response of the interferometer. We can rewrite 1.32 as

$$\Delta\phi_{GW} = 2\pi f \int_{t-2L/c}^{t} \int_{-\infty}^{\infty} h(\omega) e^{i\omega t'} d\omega dt' = \tag{1.33}$$

$$= \int_{-\infty}^{\infty} H_{\mathrm{MI}}(\omega) h(\omega) e^{i\omega t} d\omega \tag{1.34}$$

where

$$H_{\mathrm{MI}}(\omega) = \frac{4\pi f}{\omega} \sin\left(\frac{L\omega}{c}\right) e^{-\frac{L\omega}{c}} \tag{1.35}$$

is the frequency response of a simple Michelson interferometer to a gravitational wave. The maximum of $|H_\omega|$ is when

$$L = \frac{\pi c}{2\omega}$$

which means that for example to measure a gravitational wave of 100 Hz, the optimal arm length is 750 km. The construction of such a long instrument on Earth is very difficult. So, instead of building such long arms, current interferometric detectors employ Fabry-Pérot cavities in the arms of the interferometer to enhance the phase sensitivity.

1.3.2 Fabry-Pérot cavity

When a laser pass through two semi-reflective mirrors, there can be a constructive interference in the space between the two mirrors. This is called a Fabry-Pérot cavity. A laser beam with amplitude E_i enters the cavity through the front mirror, which have reflection r_1 and transmission t_1 and it is transmitted through the end mirror, which have reflection r_2 and transmission t_2. These coefficients are referred to the amplitude of the electric field. The intensity (or power) reflectivity and transmissivity of the front and end mirrors are r_1^2, t_1^2, r_2^2, and t_2^2 respectively. The electric field amplitude of the beam that is transmitted from the cavity can be calculated as a summation of multiple reflections between the two mirrors as

$$E_t = E_i t_1 t_2 e^{-i\delta} \sum_{n=0}^{\infty} \left(r_1 r_2 e^{-2i\delta}\right)^n = E_i \frac{t_1 t_2 e^{i\delta}}{1 - r_1 r_2 e^{-2i\delta}} \tag{1.36}$$

where $\delta = 2\pi f L/c$ is the phase the light accumulates travelling from one mirror to the other. The amplitude of the beam that is reflected through the cavity is

$$E_r = E_i r_1 + E_i t_F^2 (-r_2) e^{-i2\delta} \sum_{n=0}^{\infty} \left(r_1 r_2 e^{-2i\delta}\right)^n = \tag{1.37}$$

$$= E_i \left(r_1 - \frac{t_1^2 r_2 e^{-2i\delta}}{1 - r_1 r_2 e^{-2i\delta}} \right) \tag{1.38}$$

While the transmitted and reflected powers are

$$P_t = |E_t|^2 = \frac{t_1^2 t_2^2}{(1 - r_1 r_2)^2 \left(1 + \frac{4 r_1 r_2}{(1 - r_1 r_2)^2} \sin^2 \delta\right)} |E_i|^2 \tag{1.39}$$

$$P_r = |E_r|^2 = \frac{\left[\left(t_1^2 + r_1^2\right) r_2 - r_1\right]^2 + 4 r_1 r_2 \left(t_1^2 + r_1^2\right) \sin^2 \delta}{\left(1 - r_1 r_2\right)^2 \left(1 + \frac{4 r_1 r_2}{(1 - r_1 r_2)^2} \sin^2 \delta\right)} |E_i|^2 \tag{1.40}$$

The transmission is maximum when the cavity is on resonance, which happens when $\delta = \pi n$. The resonance frequencies of the laser in the cavity are:

$$f = \frac{nc}{2L} \tag{1.41}$$

and the separation of those resonance frequencies is the so-called "free spectral range", defined as $f_{\mathrm{FSR}} = c/2L$. The full width at half maximum f_{FWHM} of each resonance peak is derived from the transmission power expression

$$\frac{1}{1 + \frac{4 r_1 r_2}{(1 - r_1 r_2)^2} \sin^2(\pi L f_{\mathrm{FWHM}} / c)} = \frac{1}{2}. \tag{1.42}$$

Assuming $f_{\mathrm{FWHM}} \ll f_{\mathrm{FSR}}$, the solution to 1.42 is

$$f_{\mathrm{FWHM}} = \frac{(1 - r_1 r_2) c}{2\pi L \sqrt{r_1 r_2}}. \tag{1.43}$$

A common parameter to describe a Fabry-Pérot cavity is the so-called *finesse*, defined as the ratio

$$F \equiv \frac{f_{\mathrm{FSR}}}{f_{\mathrm{FWHM}}} \simeq \frac{\pi \sqrt{r_1 r_2}}{1 - r_1 r_2}. \tag{1.44}$$

The phase change of the reflected light around a resonance as a function of the one-way phase change δ is steep. Since the interferometer is sensitive to the phase change, around the resonance the sensitivity is enhanced by the usage of a Fabry-Pérot cavity. The higher the finesse, the steeper the phase change, and the better the sensitivity.

To calculate the frequency response of a Fabry-Pérot interferometer one calculates the time τ_n the light takes to make n round trips in the cavity using the approximation

$$\int_{t-\tau_n}^{t} 1 - \frac{1}{2} h(t') dt' \simeq \frac{2Ln}{c} \tag{1.45}$$

and express the phase change in the same way as in 1.31

$$\delta_n = 2\pi f \tau_n = 2\pi f \left(\frac{2nL}{c} + \int_{t-2nL/c}^{t} \frac{1}{2} h(t') dt' \right) \tag{1.46}$$

Then, taking the Fourier transform of $h(t)$ and substituting in the multiple reflec-

tions summation expression 1.37 of the reflected beam amplitude, we get

$$\frac{E_r}{E_i} \simeq r_1 - \frac{t_1^2 r_2 e^{-i2\delta}}{1 - r_1 r_2 e^{-i2\delta}} \left[1 - 2\pi f \int_{-\infty}^{\infty} h(\omega) \frac{1 - e^{-i2L\omega/c}}{1 - r_1 r_2 e^{-i2\delta} e^{-i2L\omega/c}} \frac{e^{i\omega t}}{2\omega} d\omega\right] \tag{1.47}$$

Around the resonance 1.47 simplifies to

$$\frac{E_r}{E_i} \simeq \frac{r_1 - (r_1^2 + t_1^2) r_2}{1 - r_1 r_2} \left[1 - i \int_{-\infty}^{\infty} H_{\mathrm{FP}}(\omega) h(\omega) e^{i\omega t}\right] \tag{1.48}$$

Where H_{FP} is the frequency response of a Fabry-Pérot interferometer

$$H_{\mathrm{FP}}(\omega) = \frac{2\pi f t_1^2 r_2}{r_1 - r_2(r_1^2 + t_1^2)} \frac{\sin(\omega L/c) e^{-iL\omega/c}}{\omega \left[1 - r_1 r_2 e^{-i2\omega L/c}\right]}. \tag{1.49}$$

Note that f is the frequency of the laser, and ω is the angular frequency of the gravitational wave signal.

Highly sensitive interferometers operate on a dark fringe to minimize shot noise, therefore most of the injected light returns toward the laser source. By inserting an additional partial mirror, called a recycling mirror, in front of the interferometer, this light is reflected back to the beam splitter and coherently added to the input laser beam. The result is to increase the effective input power and to improve the sensitivity to gravitational waves.

1.3.3 Power recycling

The end mirrors have a reflectivity very close to 1. When the interferometer is set on the dark fringe, almost all the power injected in the interferometer is reflected back to the laser source. A power recycling mirror (PR) is put in between the laser source and the beam splitter. This forms a cavity where the first mirror is the PR and the rest of the interferometer acts as the second mirror. The power inside the interferometer increases without increasing the input power. The power recycling cavity does not affect the bandwidth of the interferometer because the sidebands generated by the gravitational waves exit directly from the asymmetric port without being recycled nor filtered by the power recycling cavity. As a summary of this section, Figure 1.4 shows a diagram of the optical configuration of an interferometric gravitational wave detector of the first generation. The second generation detectors are called dual-recycled Fabry-Pérot interferometers because, besides the power recycling, they also implement the signal recycling, which is an additional mirror

before the photo-detector. The signal recycling introduces more complexity to the system, but it doesn't change the noise management and reduction.

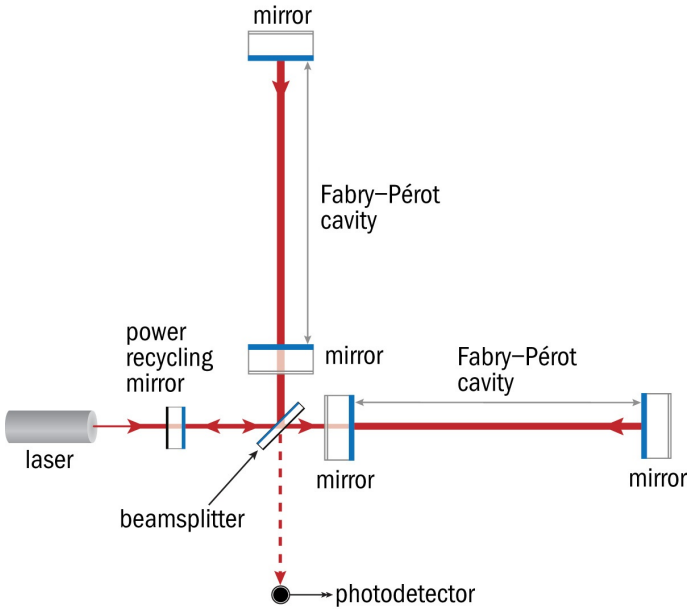

Figure 1.4: Simple diagram of the optical configuration of a power-recycled Fabry-Pérot Michelson interferometer. [© LIGO]

1.4 Noise sources

In this section, we list and explain the main noise sources that limit the sensitivity of the interferometers. The astrophysical sources that generate the strongest gravitational waves are so far that the amplitude of the GWs that reach the Earth is extremely tiny. The quantity to be measured by an interferometric gravitational wave detector is a distance variation of the order of 10^{-19}m. Since the distance changes that the interferometer should be able to measure are extremely small, most of the research effort is for reducing the noise that affects the gravitational signal.

The noise sources that affect the detector are summarized in the following list:

- shot noise - the fluctuations of the number of photons impinging on the detection photo-diode;
- fluctuations of the laser radiation pressure on the mirrors;
- seismic motion of the ground that shakes the suspensions;

- fluctuations of the gravitational field around the detector;
- thermal excitation of the suspensions, the mirrors' coating, and the substrate;
- fluctuations of the laser beam in amplitude, frequency and position (jitter);
- fluctuations of the refractive index along the laser optical path;
- stray light that scatters from the mirrors to the chamber walls and interferes with the main beam;
- electronic noise in the interferometer read-out and in the control systems;

By investigating sapphire absorption and crystalline coatings, the ultimate goal of this thesis work is to reduce thermal noise. Therefore, the largest part of this section is about the theory of thermal noise, and in particular of the mirror thermal noise.

The power spectral density of a general noise in the frequency domain is

$$S(f) = \lim_{T\to\infty} \frac{2}{T} \left| \int_{-T}^{T} A(t) e^{-i2\pi ft} dt \right|^2 \tag{1.50}$$

where $A(t)$ represents the the measured physical quantity in the time domain. The linear spectral density is defined as the root square of 1.50

$$s(f) = \sqrt{S(f)} \tag{1.51}$$

To compare the noise with the gravitational wave signal, we often use the equivalent strain noise spectral density $h(f)$

$$h(f) = \frac{x(f)}{L} \tag{1.52}$$

where $x(f)$ is the the mirror displacement noise linear spectral density and L is the interferometer arm length, and it is measured in $1/\sqrt{\text{Hz}}$).

1.4.1 Shot noise

The output power of the interferometer is measured by a photo-detector. Due to the quantum nature of light, the measurement is equivalent to a count of the number of photons N arriving on the photo-detector during the measurement time Δt. The

arrival time is characterized by the Poisson probability distribution

$$p(N) = \frac{\bar{N}^N e^{-\bar{N}}}{N!} \tag{1.53}$$

Recalling Equation 1.30, the average number of photons of energy $\hbar\omega$ is

$$\bar{N} = \frac{\eta P_{in} \Delta t}{2\hbar\omega}(1 + \cos\phi)$$

where η is the photo-diode quantum efficiency. Then, given the Poisson distribution variance, the power fluctuation is

$$\delta P_{\text{shot}} = \sqrt{\frac{2\hbar\omega}{\eta P_{in} \Delta t}(1 + \cos\phi)}$$

When a gravitational wave passes, the phase perturbation $\Delta\phi_{\text{GW}}$ makes the output power to be

$$\begin{aligned} P_{\text{PD}}(\phi + \phi_{\text{GW}}) \simeq & P_{\text{PD}}(\phi) + \frac{dP_{\text{PD}}}{d\phi}\,\phi_{\text{GW}} \\ = & P_{\text{PD}}(\phi) - \frac{P_{\text{in}}}{2}\sin\phi\,\phi_{\text{GW}} \end{aligned} \tag{1.54}$$

According to Equation 1.54 the signal should be maximum when $\sin\phi = 1$, in the *mid-fringe* condition. But the signal to noise ratio of the power change is

$$\text{SNR}_{\text{shot}} = \frac{P_{\text{in}}}{2}\sqrt{\frac{\eta P_{\text{in}} \Delta t}{2\hbar\omega}}\frac{\sin\phi}{\sqrt{1 + \cos\phi}}\Delta\phi_{\text{GW}} \tag{1.55}$$

and it is maximum when $\cos\phi = -1$ which means in the *dark-fringe* condition. The equivalent strain spectral density $h_{\text{shot}}(f)$ for the shot noise is [4]

$$h_{\text{shot}}(f) = 2.9 \times 10^{-21}[\text{Hz}^{-1/2}]\left(\frac{3[\text{km}]}{L}\right)\sqrt{\frac{\lambda}{1.064[\mu\text{m}]}}\sqrt{\frac{70[\text{W}]}{P_{\text{in}}}} \tag{1.56}$$

To reduce this noise, a high power laser source is used. Also, the power recycling technique, that increases the power inside the interferometer, reduces the shot noise.

1.4.2 Radiation pressure noise

On one hand, increasing the laser power reduces the shot noise, on the other hand, it increases the effect of the laser power fluctuations on the test masses. Due to the

quantum nature of light, the total momentum transferred from the photons to the mirror fluctuates. The spectral density of the force that pushes the mirrors is

$$F(f) = \sqrt{\frac{2\pi\hbar P}{c\lambda}} \tag{1.57}$$

the corresponding position fluctuation of the free falling test mass is

$$x(f) = \frac{1}{M(2\pi f)^2} F(f) = \frac{1}{M(2\pi f)^2} \sqrt{\frac{2\pi\hbar P}{c\lambda}} \tag{1.58}$$

The radiation pressure noise strain equivalent is

$$h_{\mathrm{rp}} = \frac{1}{Mf^2L} \sqrt{\frac{\hbar P}{2\pi c\lambda}} \tag{1.59}$$

The optical quantum noise is thus made by two contributions that have the same quantum nature and can be added in quadrature giving

$$h_{\mathrm{oro}} = \sqrt{h_{\mathrm{shot}}^2 + h_{\mathrm{rp}}^2} \tag{1.60}$$

The radiation pressure dominates at low frequencies because it is proportional to $1/f^2$ while the shot noise dominates at high frequencies because it has a white spectrum. On varying the power P it is possible to find a frequency f_0 where $h_{\mathrm{shot}}(f_0) = h_{\mathrm{rp}}(f_0)$, which is the minimum noise spectral density. The locus of these minimum doesn't depend on the laser power and it is called the standard quantum limit

$$h_{\mathrm{SQL}}(f) = \frac{1}{\pi f L} \sqrt{\frac{\hbar}{M}} \tag{1.61}$$

The standard quantum limit is an application of the Heisenberg principle to the interferometric measurement. It is possible to push the noise below this quantum limit by injecting particular squeezed states of light in the interferometer. Frequency-dependent squeezing allows to reduce the quantum noise for a wide range of frequencies. The application of such technology is currently under investigation [5].

1.4.3 Seismic noise

The ground vibrates for many reasons like earthquakes, human activities, wind, sea waves. The ground motion follows the empirical law

$$x_{\mathrm{g}} = 10^{-7} \frac{\mathrm{m}}{\sqrt{\mathrm{Hz}}} \left(\frac{10Hz}{f} \right). \tag{1.62}$$

This movement is several orders of magnitude larger than the expected gravitational signal. Therefore, the test masses and other mirrors of gravitational wave interferometers cannot simply sit on the ground. Ground-based interferometer gravitational wave detectors have to deal with this noise using vibration isolation systems to reduce the mirror motion. The suspensions constituted by a chain of filters. Each filter stage consists of pendulums for the horizontal motion and springs for the vertical motion. Considering a simplified model, each stage of the suspension have a different resonance frequency ω_k. The attenuation can be expressed by the suspension transfer function between the suspension point x_0 and the test mass position x:

$$\frac{x(\omega)}{x_0(\omega)} = \prod_{k=1}^{N} \frac{\omega_k^2}{\omega_k^2 - \omega^2}. \tag{1.63}$$

Technical constraints such as the maximum number of stages or the available pendulum lengths limit the attenuation of the suspensions below $\sim 1\,\mathrm{Hz}$.

1.4.4 Newtonian noise

The test masses are also subject to the gravitational field of the masses around them. Local fluctuations of the gravitational field are due to ground motion, wind, ocean activity, nearby water flowing, snow and other moving masses. According to the Newtonian law of gravity, the effect of these fluctuations is a displacement of the test masses. The main contribution to Newtonian noise is the seismic movement. The strain equivalent noise is

$$h_{\mathrm{nn}} = \frac{G}{\sqrt{3\pi}} \frac{\rho}{L} \frac{x_g}{f^2} \tag{1.64}$$

where x_g is the ground motion spectrum introduced in Equation 1.62, L is the arm length, G is the gravitational constant and ρ is the mass density of the ground around the test masses [6]. Due to the frequency dependence of the seismic noise, the Newtonian noise affects the sensitivity at lower frequencies, below 10 Hz.

1.4.5 Thermal noise

Given a linear system that is in thermal equilibrium with its surroundings and that obeys the detailed balance principle, the fluctuation-dissipation theorem relates the thermal fluctuations of a physical quantity with the dissipation mechanism for that physical quantity. [7]
This theorem states that the power spectrum of a force $F(\omega)$ applied to the generalized coordinate $x(\omega)$ is

$$F_{\text{th}}^2(\omega) = 4k_B T \,\text{Re}\{Z(\omega)\} \tag{1.65}$$

where k_B is the Boltzmann constant, T is the temperature, and $Z(\omega)$ is the generalized complex impedance defined as

$$Z(\omega) = \frac{F(\omega)}{v(\omega)} = \frac{F(\omega)}{i\omega x(\omega)}. \tag{1.66}$$

In the case of an electric conductor, replacing the force F with the voltage and $\text{Re}[Z(\omega)]$ with the resistance, Equation 1.65 describes the Johnson noise. The power spectrum of the generalize coordinate $x(\omega)$ is therefore

$$x_{\text{th}}^2 = \frac{4k_B T}{\omega^2} \,\text{Re}\{Y(\omega)\} \tag{1.67}$$

where $Y(\omega)$ is the generalized admittance of the system $Y(\omega) = Z^{-1}(\omega)$. In the case of a damped harmonic oscillator, the equation of motion is

$$m\ddot{x} + \gamma\dot{x} + kx = F_{\text{th}} \tag{1.68}$$

where k is the elastic constant and m the mass. The damping mechanism is described macroscopically by the parameter γ, but it has a microscopical origin. According to the fluctuation-dissipation theorem, the microscopical mechanism responsible for the damping is also responsible for the thermal fluctuation of the coordinate x. Being the admittance of this system

$$Y(\omega) = \frac{\gamma\omega^2 + i\omega(k - m\omega^2)}{(k - m\omega^2)^2 + \gamma^2\omega^2} \tag{1.69}$$

the damped harmonic oscillator position have a power spectrum

$$x_{\rm th}^2 = \frac{4k_B T\gamma}{(k - m\omega^2)^2 + \gamma^2\omega^2}, \tag{1.70}$$

this spectrum have a resonance at $\omega_0 = \sqrt{k/m}$. When the damping coefficient is small, the resonance is higher, but outside the resonance, the noise is lower. In other words, the noise is more concentrated on the resonance peak. Two examples of this kind of damping are the residual gas around the test masses and the eddy currents in the magnets used in the force actuators to control the position of the mirrors. There are damping mechanisms also in the materials of the mirrors substrate and coating, and the suspension wires. This kind of mechanisms is due to material structure dislocations and is called structural damping. It is modeled with a generalized Hooke's law where an imaginary part is added to the elastic constant of the material. So, the oscillator equation of motion is

$$m\ddot{x} + k(1 + i\phi)x = F \tag{1.71}$$

where ϕ is called the loss angle. The thermal noise for this simple model of structural damping is

$$x_{\rm th}^2 = \frac{4k_B T\phi}{\omega[(k - m\omega^2)^2 + k^2\phi^2]}. \tag{1.72}$$

Pendulum thermal noise

The gravity is a conservative force, so the elastic constant of a pendulum, $k_{\rm g} = mg/L$, is lossless. This makes the pendulum a good technique for the vibration isolation suspensions. However, a small part of the restoring force of the suspension is given by the elasticity of the wires, which have a loss angle $\phi_{\rm w}$. The elastic constant given by n suspension wires with length L, Young's modulus E, tension T, and inertia momentum I is $k_{\rm el} = n\sqrt{TEI}/2L^2$. The total restoring force is given by the elastic force

$$k = k_{\rm g} + k_{\rm el}(1 + i\phi_{\rm w}) \tag{1.73}$$

Since the gravity term is much larger than the wire elasticity term, $k_{\rm g} \gg k_{\rm el}$, 1.73 becomes

$$k \simeq k_{\rm g}(1 + i\frac{k_{\rm el}}{k_{\rm g}}\phi_{\rm w}) \tag{1.74}$$

Given that the tension T is proportional to the mass m and the inertia momentum is proportional to m^2, the effective losses $\frac{k_{\rm el}}{k_{\rm g}}\phi_{\rm w}$ are proportional to $m^{1/2}$. Hence,

the power spectrum $x_p^2(\omega)$ is proportional to $m^{-1/2}$, increasing the mass the thermal noise decreases. This is one of the reasons why the mirrors are as massive as possible.

Mirror thermal noise

The simple models for the harmonic oscillators 1.68 and 1.71 can describe the motion of the center of mass of a mirror, but they are not enough to model the thermal noise in a continuous medium such as the substrate or the coating. Actually, it is possible to model a continuous system with an infinite number of vibrational eigenmodes, each of them with its resonance frequency and its loss angle; to calculate the response of an applied force projected on each eigenmode and finally summing up the total impedance to calculate the fluctuations. But this method can become computationally cumbersome and it assumes that the losses are uniform along the system, which is not always true [8]. Another method, proposed by Levin [9], consists in doing a mental experiment applying a force on the surface of the mirror and calculating the system impedance for an observable that represents the surface displacement. The displacement observable is

$$x(t) = \int I(\mathbf{r})u(\mathbf{r},t)dS \tag{1.75}$$

where $\mathbf{r}$ is the position on the surface, $I(\mathbf{r})$ is the gaussian profile of the laser beam and the integral is extended on the mirror surface. The applied force $F(\mathbf{r},t)$ has the same intensity distribution of the laser beam, which means $F(\mathbf{r},t) = I(\mathbf{r})F(t)$. The admittance of this system is

$$Y(\omega) = \frac{i\omega x(\omega)}{F(\omega)} \tag{1.76}$$

the real part of the admittance 1.76 is related to the dissipation of the system as

$$\mathrm{Re}[Y(\omega)] = \mathrm{Re}\left[\frac{v(\omega)F^*}{|F(\omega)|^2}\right] = \frac{W_{\mathrm{diss}}(\omega)}{|F(\omega)|^2} \tag{1.77}$$

Using the fluctuation-dissipation theorem, the spectrum of the mirror by thermal noise is

$$x_{\mathrm{th}}^2 = \frac{4k_BT}{\omega^2}\,\mathrm{Re}[Y(\omega)] = \frac{4k_BT}{\omega^2}\frac{W_{\mathrm{diss}}(\omega)}{|F(\omega)|^2} \tag{1.78}$$

to calculate the thermal noise, we have to calculate the dissipated energy: $W_{\mathrm{diss}}(\omega)$. The structural losses of a continuous system are modeled adding an imaginary part to Young modulus $E(\omega) = E_0(1 + i\phi(\omega))$, where $\phi(\omega))$ is the loss angle of the

material. The dissipated energy is given by

$$W_{\text{diss}} = \omega\phi(\omega)U_{\max}(\omega) \tag{1.79}$$

where $U_{\max}(\omega)$ is the maximum energy stored in the mirror during an oscillation of the applied force. Since the gravitational signal frequencies where the detectors are most sensitive are far below the resonances of the mirror, it is sufficient to calculate $U_{\max}$ at $\omega = 0$.

$$U_{\max}(0) = \frac{1-\sigma^2}{2\sqrt{\pi}E_0 w}|F(\omega)|^2 \tag{1.80}$$

where σ is the Poisson ratio, and w the laser beam radius.
The mirror thermal noise spectrum is therefore

$$x^2_{\text{th}}(\omega) = \frac{4k_bT}{\omega}\frac{(1-\sigma^2)}{2\sqrt{\pi}E_0 w}\phi \tag{1.81}$$

Thermo-optic noise

The loss angle ϕ represents the dissipation mechanism due to structural friction inside the material, and it leads to the Brownian noise. However, there is also another important energy dissipation mechanism. When a part of the material get compressed, it heats up and the heat flows from the warmer zone to the colder zone. The fluctuation-dissipation theorem relates this dissipation (the heat flow) to temperature fluctuations, indeed the generalized coordinate is the temperature and the generalized force is the entropy. The temperature fluctuations lead to two effects: one is the thermal expansion of the material and is called thermo-elastic noise; the other is the thermal change in the refractive index, and is called thermo-refractive noise. These two noises are collectively called thermo-optic noise.
One way to calculate the thermo-elastic noise is to inject some entropy, solve the thermal conductivity equation to find how the system responds to the entropy injection, and apply the fluctuation-dissipation theorem, [10]. The result is

$$x^2_{\text{th}}(\omega) = \frac{8}{\sqrt{2\pi}}\alpha^2(1+\sigma)^2\frac{k_BT^2\kappa}{\rho^2C^2w^3\omega^2} \tag{1.82}$$

where α is the expansion coefficient, σ is the Poisson coefficient, κ is the thermal conductivity, ρ is the density, C is the specific heat capacity, and w is the beam radius.

The thermo-refractive noise has been calculate by [11] and it is

$$x^2_{\text{th}}(\omega) = \frac{16}{\pi\omega^2}\frac{k_B T^2 \kappa l}{\rho^2 C^2 w^4}\left(\frac{dn}{dT}\right)^2 \tag{1.83}$$

where l is the optics length and dn/dT is the thermo-refractive coefficient.

Coating thermal noise

The main contribution to the mirror total thermal noise comes from the high reflective dielectric multilayer coating on the mirror surface. The coating thickness is a few microns, but when a gaussian force is applied on a mirror most of the stored energy is concentrated on the surface; moreover, the losses of the coating material are larger than the substrate ones. One can calculate the Brownian noise of the coating in the same way as Equation 1.81 was derived. In the case of coated mirrors, the total loss angle ϕ can be calculated as a weighted sum of the losses in the substrate and in the coating:

$$\phi = \frac{1}{U}\left(U_s\phi_s + U_c\phi_c\right) \tag{1.84}$$

where the subscript s stands for substrate and the subscript c stands for coating. Since the coating is thin compared to the size of the pressure distribution, and most of the energy is stored on the substrate, Equation 1.84 can be approximated as

$$\phi = \phi_s + \frac{\delta U d}{U}\phi_c \tag{1.85}$$

where δU is the energy density on the substrate integrated on the surface, and d is the coating thickness. Since the material is in general anisotropic, we separate the energy related to strains parallel to the coating surface and the perpendicular ones

$$\phi = \phi_s + \frac{\delta U_\parallel d}{U}\phi_\parallel + \frac{\delta U_\perp d}{U}\phi_\perp \tag{1.86}$$

after calculating the energies using the strains and stresses in the coating and in the substrate, and applying the fluctuation-dissipation theorem the total thermal noise

is

$$x^2_{\rm th}(\omega) = \frac{4k_BT}{\omega}\frac{1-\sigma_s^2}{wE_s}\Bigg\{\phi_s + \frac{d}{\sqrt{\pi}w}\frac{1}{E_sE_c(1-\sigma_c^2)(1-\sigma_s^2)} \Bigg[E_c^2(1+\sigma_s)^2(1-2\sigma_s)^2\phi_\parallel + E_sE_c\sigma_c(1+\sigma_s)(1+\sigma_c)(1-2\sigma_s)(\phi_\parallel-\phi_\perp) + E_s^2(1+\sigma_c)^2(1-2\sigma_c)\phi_\perp\Bigg]\Bigg\} \tag{1.87}$$

where T is the mirror temperature, w is the beam radius and d is the thickness of the coating, E_s is Young's modulus of the substrate, E_c is Young's modulus of the coating, σ_s is the Poisson ratio of the substrate, and σ_c is the Poisson's ratio of the coating. The details of the calculation are in [12]. In the equations above the coating has been considered as an approximately uniform layer. In a more realistic model, the alternating layers that compose the dielectric coating have different mechanical properties. Taking the approximation of small Poisson ratio ($\sigma \lesssim 0.25$), we can rewrite Equation 1.87 as

$$x^2_{\rm th}(\omega) = \frac{4k_BT}{\omega}\frac{1}{wE_s}\left\{\phi_s + \frac{d}{\sqrt{\pi}w}\left(\frac{E_\parallel}{E_s}\phi_\parallel + \frac{E_s}{E_\perp}\phi_\perp\right)\right\} \tag{1.88}$$

where Young's moduli and the loss angles become

$$E_\perp = \frac{d_1+d_2}{d_1/E_1 + d_2/E_2} \qquad E_\parallel = \frac{E_1d_1 + E_2d_2}{d_1+d_2} \tag{1.89}$$

$$\phi_\perp = \frac{E_\perp}{d_1+d_2}\left(\frac{d_1}{E_1}\phi_1 + \frac{d_2}{E_2}\phi_2\right) \qquad \phi_\parallel = \frac{E_1d_1\phi_1 + E_2d_2\phi_2}{E_\parallel(d_1+d_2)} \tag{1.90}$$

where the subscripts 1,2 indicate the two materials that compose the coating. We can calculate the total coating Brownian noise by adding the contribution from each test mass of the interferometer. Each dielectric mirror brings two contributes, one from the low-index layer material and the other from the high-index layer material. Given the number of layer doublets N_c, the laser wavelength λ, the low refractive index n_1 and the high refractive index n_2, then

$$d_1 = \frac{N_c+1}{n_1}\frac{\lambda}{4}; \qquad d_2 = \frac{N_c}{n_2}\frac{\lambda}{4}$$

Assuming that the material perpendicular and parallel losses are equal, $\phi_\parallel = \phi_\perp$,

Equation 1.87 becomes:

$$x^2_{\text{th}}(\omega) = \frac{4k_BT}{\omega}\frac{d}{\pi w^2}\frac{E_c^2(1+\sigma_s)^2(1-2\sigma_s)^2 + E_s^2(1+\sigma_c)^2(1-2\sigma_c)}{E_s^2E_c(1-\sigma_c^2)}\phi \tag{1.91}$$

where d is d_1 or d_2 depending on the coating material. For each mirror, the total coating noise is made of two material contributions that are calculated with Equation 1.91 (replacing the parameters of the respective coating material). This equation is used in the next chapter to estimate the coating noise improvement for the crystalline coating studied in this thesis.

1.5 Detectors network

The sensitivity of a single interferometer depends on the direction of the astronomical source and on the polarization of the gravitational wave. For each polarization, there is a different sensitivity distribution in sky. With only one detector, the localization of the source is not accurate, so it is necessary to have a network of synchronized detectors. If two detectors are far apart, the signal arrival time delay between the two detectors is a piece of useful information to locate the source. With three detectors the localization can be reduced to one or a few spots, and with more detectors, the localization precision improves.

1.5.1 First generation gravitational wave detectors

The interferometric type of detectors has been proposed in the 1960s. Since then, a lot of feasibility studies and prototyping have been done and their construction started in the 1990s. The first generation interferometric gravitational wave detectors are the two LIGO, 4 km-long, located in Livingston, Louisiana and in Hanford, Washington; Virgo 3 km-long located near Pisa, Italy; GEO600 600 m-long located near Hannover, Germany, and TAMA300, 300 m-long, located in the Mitaka campus of NAOJ in Tokyo, Japan. Their best sensitivity were $1.5 \cdot 10^{-21}/\sqrt{\text{Hz}}$ (TAMA), $2 \cdot 10^{-22}/\sqrt{\text{Hz}}$ (GEO), $6 \cdot 10^{-23}/\sqrt{\text{Hz}}$ (Virgo), $2 \cdot 10^{-23}/\sqrt{\text{Hz}}$ (LIGO) [13]. Although they didn't detect any gravitational wave event, their construction and tuning allowed to build a deep knowledge of the detectors and of their limits. The analysis of the data taken by those detectors allowed to set upper limits to the event rate of binary black holes merger (BH-BH) to $6.4 \cdot 10^{-6}\text{Mpc}^{-3}/\text{yr}$; of binary neutron star merger (NS-NS) to $1.3 \cdot 10^{-4}\text{Mpc}^{-3}/\text{yr}$; and of black hole and neutron star merger

(NS-BH) to $3.1 \cdot 10^{-5}\mathrm{Mpc}^{-3}/\mathrm{yr}$.

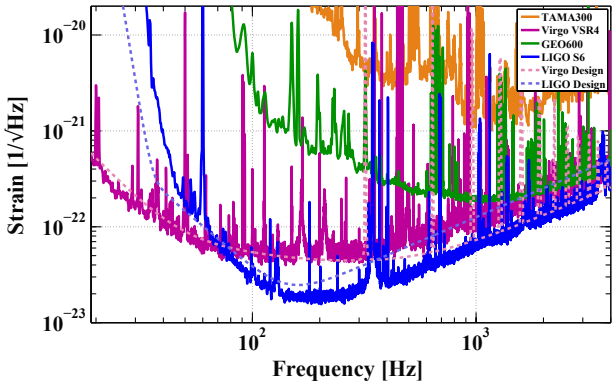

Figure 1.5: Strain noise for the first generation detectors. TAMA300, GEO600, Virgo+, and Enhanced LIGO. Also shown (dashed) are the strain noise goals for the initial Virgo and LIGO detectors [13].

1.5.2 Second generation gravitational wave detectors

Since the event detection rate scales with the volume of the reachable portion of the universe, improving the sensitivity of the detectors by a factor of 10, increases the event detection rate by a factor of 1000. To increase the sensitivity, the existing facilities of LIGO and Virgo were upgraded to make two Advanced LIGO, and Advanced Virgo. Meanwhile, a new Japanese detector (KAGRA) started its construction in 2012, with the tunnel excavation, and it is currently under commissioning. Some pictures of the 4 interferometers are shown in Figure 1.6, and Figure 1.7 shows the sensitivity curves of the three detectors running together during the second observation run (O2). An observation run, is a phase when the interferometer is locked in resonance, the noise is minimized, and it is "listening" to the universe and recording data. During the first observation run (O1), on September 14th, 2015, the two Advanced LIGO detected for the first time a gravitational wave signal, GW150914 [1]. It was emitted by the merger of two black holes with masses $36\,\mathrm{M}_\odot$ and $29\,\mathrm{M}_\odot$. The signal to noise ratio (SNR) was 24. The estimated distance is between 230 and 570 Mpc. This event marked the beginning of the gravitational wave astronomy. Other detections followed, and they are summarized in Table 1.1. We can have an idea of the importance of having a detector network by looking at Figure 1.8, which summarizes the localization of the BH-BH merger events detected in O1 and O2. Having a third detector (Virgo) in GW170814 dramatically reduced the estimated portion of sky where the GW signal came from. During O2, on Au-

Figure 1.6: Pictures of the 4 interferometric gravitational waves detectors. The two LIGO observatories in Hanford and Livingston, Virgo in the countryside of Pisa, and an artistic view of KAGRA inside the Kamioka mine.

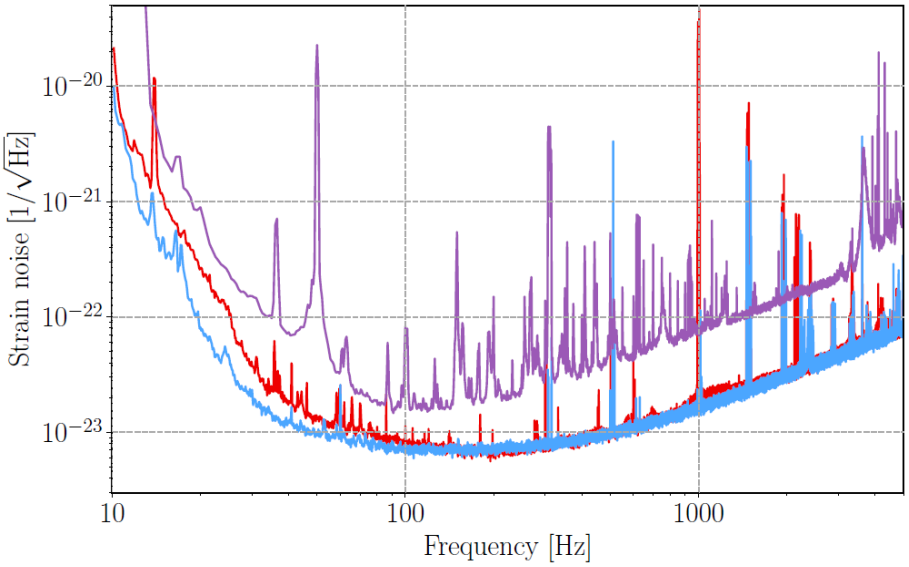

Figure 1.7: Sensitivity of the two Advanced LIGO (blue and red curves) and Advanced Virgo (purple curve) during the second observation run O2. This kind of sensitivity curves are the result of the sum of all the noises affecting the interferometer readout. The lower the curve, the better the sensitivity.

Event	Masses [$M_\odot$]		Final [$M_\odot$]	d [Mpc]	Solid angle [deg^2]
GW150914	$35.6^{+4.8}_{-3.0}$	$30.6^{+3.0}_{-4.4}$	$63.1^{+3.3}_{-3.0}$	430^{+150}_{-170}	179
GW151012	$23.3^{+14.0}_{-5.5}$	$13.6^{+4.1}_{-4.8}$	$35.7^{+9.9}_{-3.8}$	1060^{+540}_{-480}	1555
GW151226	$13.7^{+8.8}_{-3.2}$	$7.7^{+2.2}_{-2.6}$	$20.5^{+6.4}_{-1.5}$	440^{+180}_{-190}	1033
GW170104	$31.0^{+7.2}_{-5.6}$	$20.1^{+4.9}_{-4.5}$	$49.1^{+5.2}_{-3.9}$	960^{+430}_{-410}	924
GW170608	$10.9^{+5.3}_{-1.7}$	$7.6^{+1.3}_{-2.1}$	$17.8^{+3.2}_{-0.7}$	320^{+120}_{-110}	396
GW170729	$50.6^{+5.3}_{-1.7}$	$34.3^{+9.1}_{-10.1}$	$80.3^{+14.6}_{-10.2}$	2750^{+1350}_{-1320}	1033
GW170809	$35.2^{+8.3}_{-6.0}$	$23.8^{+5.2}_{-5.1}$	$56.4^{+5.2}_{-3.7}$	990^{+320}_{-380}	340
GW170814	$30.7^{+5.7}_{-3.0}$	$25.3^{+2.9}_{-4.1}$	$53.4^{+3.2}_{-2.4}$	580^{+160}_{-210}	87
GW170817	$1.46^{+0.12}_{-0.1}$	$1.27^{+0.09}_{-0.09}$	≤ 2.8	40^{+10}_{-10}	16
GW170818	$35.5^{+7.5}_{-4.7}$	$26.8^{+4.3}_{-5.2}$	$59.8^{+4.8}_{-3.8}$	1020^{+430}_{-360}	39
GW170823	$39.6^{+10.0}_{-6.6}$	$29.4^{+6.3}_{-7.1}$	$65.6^{+9.4}_{-6.6}$	1850^{+840}_{-840}	1651

Table 1.1: Compact binary coalescences detected during the observation runs O1 and O2. This table is a simpler version of the table in [14]

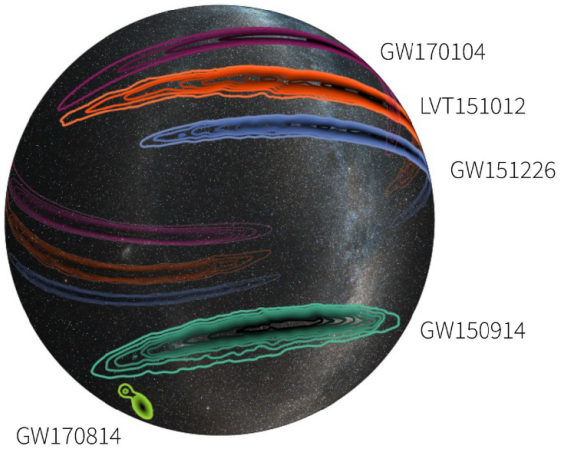

Figure 1.8: BH-BH merger events detected in O1 and O2. Having a third detector (Virgo) in GW170814 dramatically increased the localization precision. [Image credit: LIGO/Virgo/Caltech/MIT/Leo Singer (Milky Way image: Axel Mellinger)]

gust 16th, 2017 the three detectors (LIGO and Virgo) detected for the first time the gravitational wave emitted during the inspiral and merging of a binary neutron star. The masses estimation is between $1.2\,M_\odot$ and $1.6\,M_\odot$. The signal lasted for 100 s. It was observed with a combined SNR of 32.4 and it is the loudest GW signal ever recorded. Thanks to the electromagnetic follow up observations, an impressive amount of relevant scientific information has been produced [15]. Many gravitational waves have been detected, but this is just the beginning of the gravitational astronomy. As explained in the previous section, having more detectors improves the localization precision. Having 4 detectors will also improve the duty cycle, when whenever one of the detectors will be temporarily shut down for improvements, the others can stay in the data-taking mode to be in continuous listening of the universe. For this reasons, other detectors like KAGRA, Einstein Telescope, and space-based interferometers like DECIGO and LISA have been funded for feasibility studies, construction and development.

The next chapter will focus on the experimental details of KAGRA, and on the motivations of this thesis.

Chapter 2

KAGRA

As we mentioned in the previous chapter, with a larger number of detectors in the network, the signal-to-noise ratio will increase, and the source localization precision will improve. In this chapter, we summarize the features of KAGRA, and give the motivations for this thesis work, regarding the sapphire absorption requirements and the R&D work on high-reflective coatings.

The gravitational wave detector KAGRA, previously called Large Cryogenic Gravitational wave Telescope (LCGT), is currently under construction inside the Kamioka mine in Gifu prefecture, Japan, see Figure 2.1. In this new detector, the seismic noise and the thermal noise will have a significant reduction. Moreover, KAGRA will lead the path to third generation ground-based detectors like the Einstein-Telescope. The recent first gravitational wave detection was an important achievement for the gravitational wave research, yet only the first step in the new era of gravitational astronomy. It proved the possibility of doing new astronomy and motivated more efforts in the improvement of the detectors' sensitivity.

The first section of this chapter is a brief overview of the detector configuration. In the second section, we give more details about the cryogenic system and about the requirements for the sapphire substrates. In the third section, we introduce the research ongoing for the improvement of the KAGRA sensitivity: we introduce the research on crystalline coating done during this Ph.D. thesis work.In the last section, we estimate the expected improvement once these new technologies will be implemented in KAGRA.

Figure 2.1: Picture of the KAGRA tunnel inside the Kamioka mine.

2.1 Detector configuration

KAGRA is a power- and signal-recycled Fabry-Pérot Michelson interferometer, a configuration similar to the one of Advanced LIGO [16] and Advanced Virgo [17]. Compared to other existing large-scale detectors, KAGRA has two main differences that make it unique: it is built underground to reduce seismic noise, and it has cryogenic mirrors to reduce thermal noise. It employs sapphire for the test masses, which will be cooled down to 20K. Building it underground, where there is low RMS ground motion and seismic noise is lower, relaxes the requirements for the interferometer control and so reduces the impact of the actuation noise.The reason for the cryogenic operation is that the thermal noise is proportional to the temperature. The choice of the substrate material is made considering this: at cryogenic temperatures, fused silica has a bad thermal conductivity, so it would be difficult to cool down the test masses; sapphire, instead, because of its crystalline structure, has good conductivity at low temperature. Another benefit about the cryogenic operation is that, due to the high thermal conductivity of sapphire at 20K, there is almost no thermal lensing effect in the mirrors, which is currently a big issue for room-temperature detectors.

The new features of such detector come along with new issues. The floor is tilted for the water drainage system. So the mirrors have to be tilted, making the alignment and control more difficult. The laser power is limited by the amount of

absorbed heat that can be extracted through the mirrors suspension fibers. The planned final optical configuration [18] is similar to the one of Advanced LIGO and Advanced Virgo. It has folded recycling cavities to avoid the cavities degeneracy for the laser frequency side-bands [19]. The main difference is that the finesse of the Fabry-Pérot cavities is higher (1500 compared to 450 in LIGO and Virgo) in order to reduce the laser power inside the power recycling cavity, therefore inside the input mirror substrates. This allows reducing the heat to be extracted in order to cool down the mirrors. The laser is an Nd:YAG at 1064 nm. The final input power will be around 180 W. The power stored in the Fabry-Pérot cavities will be about 400 kW.

The test masses are suspended at a mechanical system that isolates from the seismic vibrations. These vibration isolation systems are based on a chain of pendulums and springs made of maraging steel combined in a design similar to the one used in Virgo and TAMA300. The number of mechanical filters depends on the isolation required. The largest attenuator is the so-called Type A, 15 m tall. It is composed of a low frequencies pre-isolator and 5 seismic filters, and it is used to suspend the 4 sapphire mirrors of the two Fabry-Pérot cavities. A shorter vibration isolation system, called Type B, is composed of the pre-isolator and 2 seismic filters. It is used to suspend the beam splitter and the signal recycling mirrors. A simplified version, the Type Bp without pre-isolator, will be used to suspend the recycling mirrors. For the input and output optics components, a double pendulum is assembled on the bench itself sustained by three stacks of masses and springs [20]. The design sensitivity of KAGRA was declared in 2009, and then updated in 2017. There are several configuration steps before reaching the maximum KAGRA sensitivity. The current intermediate goal is called bKAGRA, which stands for baseline KAGRA and it is operated with the final detector configuration at cryogenic temperature. The bKAGRA estimated sensitivity curve is shown in Figure 2.2.

2.2 KAGRA cryogenic operation

In this section we introduce the cryogenic system developed for KAGRA and we give the requirements for the sapphire absorption.

The test masses are cooled down in a cryostat vacuum chamber. The cryostat has two shields, an outer shield at the temperature of 80 K and an inner one at 8 K. Four cryo-coolers are used, the first stages of the cryo-coolers extract heat from the outer shield, while the second stages of the cryo-coolers act on different parts of the

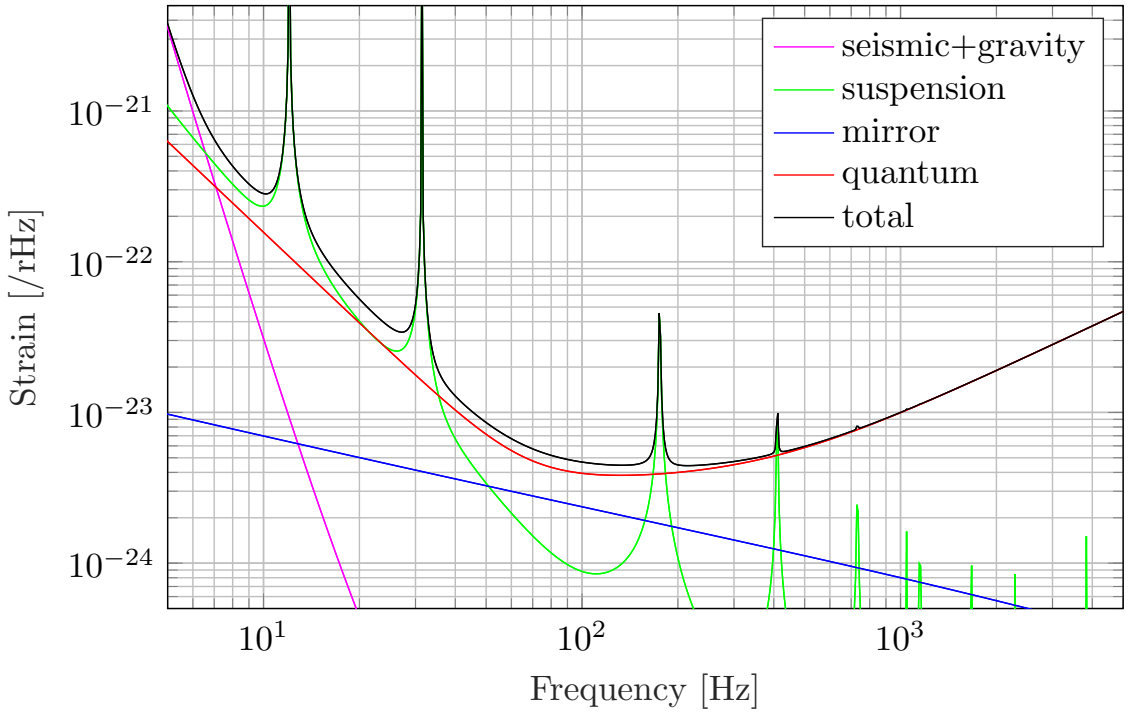

Figure 2.2: Design sensitivity of bKAGRA. The various noises contributions are summed up in the black curve. Mirror substrate Brownian and thermoelastic noise, and coating Brownian noise are summed up in the blue curve, suspension thermal noise is the green curve, seismic noise is the magenta curve and quantum noise is the red curve. The quantum noise is calculated here in the BRSE configuration (Broadband resonant sideband extraction). To calculate this plot we used the official script written by K. Somiya [21].

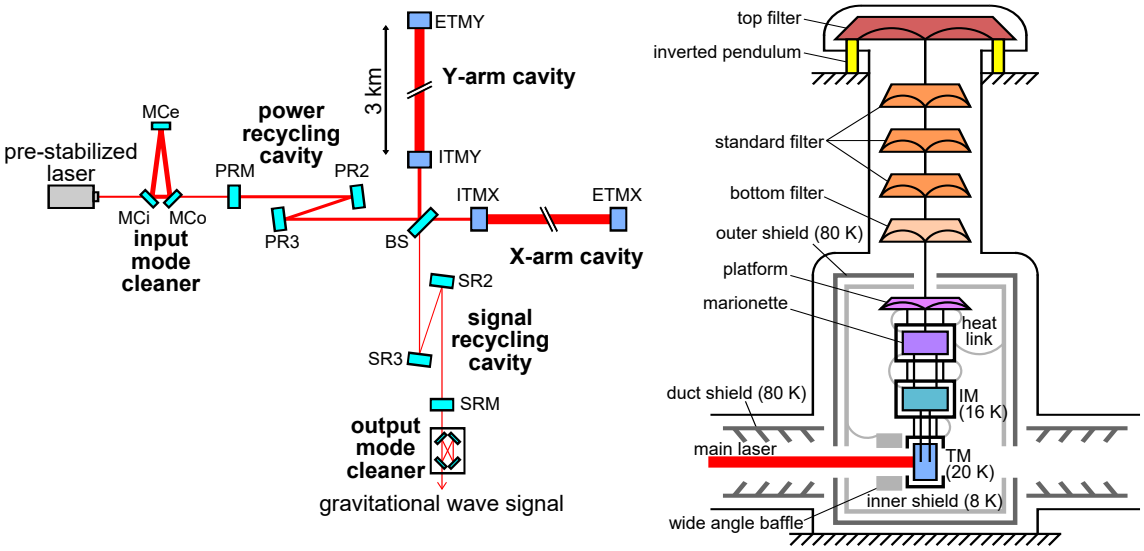

Figure 2.3: On the left, detector configuration of KAGRA. On the right, cryogenic suspension system for sapphire test masses. The marionette, the intermediate mass (IM) and the test mass (TM) are surrounded by their respective recoil masses for position and alignment control [22].

cryostat: two of them extract heat from the inner shield and two of them extract heat from the mirror payload. The design is made to be able to reach a temperature of 20 K in the test mass. The cryogenic suspension is represented in Figure 2.3, and a detailed drawing of the lowest part is shown in Figure 2.4. The test masses are suspended with sapphire fibers that connect them to the intermediate masses. The fibers are monolithic to reduce the suspension thermal noise. The fibers thickness is 1.6 mm diameter, and is a compromise between the thermal noise reduction (as thin as possible) and the amount of extractable heat (as thick as possible). Sapphire prisms (ear) are used to attach the fibers to the mirror. The ears are bonded to the side of the mirror with the technique of Hydroxide Catalysis Bonding. The upper end of each fiber is attached to a sapphire blade through a thin Indium layer, and the sapphire blade is fixed at the intermediate mass. All the heat produced in the test mass must be transferred through the suspension fibers. To calculate the absorption requirement let's consider the amount of heat that is possible to transfer from an object at temperature T_2 to and object at temperature T_1 is given by

$$K = \int_{T_1}^{T_2} \frac{\pi d_w^2}{4 l_{\mathrm{sus}}} N_w \kappa(d_w, T) dT \tag{2.1}$$

where d_w, l_{sus}, and N_w are respectively diameter, length, number of the fibers, while κ is the thermal conductivity that depends on the diameter and on the temperature

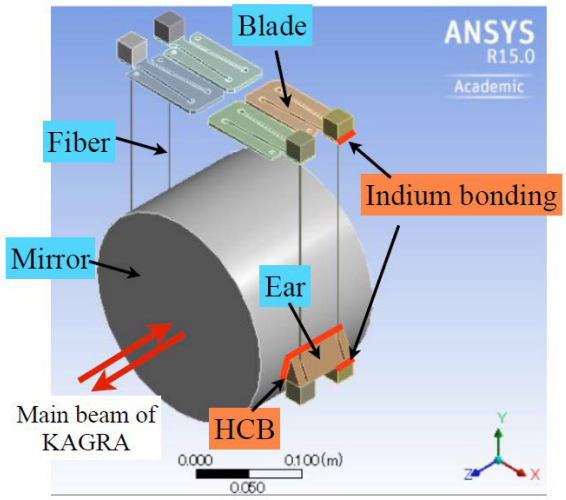

Figure 2.4: Design of the sapphire suspension [20, 23].

through the law: $\kappa \simeq 5270 d_w (T/1\,K)^{2.24} [\mathrm{W^{-1}m^{-1}K^{-1}}]$, which is valid for temperatures below ∼40 K [24]. The laser power that reaches the input test mass (ITM) is 800 W, and the power resonating inside the Fabry-Pérot cavity is 400 kW. Assuming 1 ppm of absorption on the coating and 50 ppm/cm in the substrate, and considering additional 200 mW of heat coming through apertures of the vacuum chamber, the amount of heat extracted through the fibers has to be 1.2 W. The only way to extract the heat is through the fibers, therefore, a larger amount of heat to be extracted would require thicker fibers, as shown in Equation 2.1. As explained in Chapter 1, increasing the mass of the suspension fibers, will increase the thermal noise. This is the reason why it is so important to have low absorption sapphire substrates. According to this design, the requirement for the bulk absorption of sapphire is 50 ppm/cm.

2.2.1 Thesis motivation: sapphire absorption

The fabrication of large size sapphire substrates is a technological challenge for crystal growing companies. The causes of sapphire absorption are not completely understood, they may depend on the growth procedure and on the material purity. The companies are doing efforts to make crystals as pure as possible, but each crystal boule has different absorption. For these reasons, sapphire substrates absorption need to be measured sample by sample. There are several experiments in the world that can measure the absorption of large substrates (in LMA, in Caltech, etc), but no one was available in Japan until this thesis work. To measure the substrates,

every sample had to be shipped overseas. Having such a system in Japan allows saving time and cost. This was the main motivation for developing an absorption measurement system in NAOJ. The details of the system developed and tested in NAOJ are described in Chapter 3 and Chapter 4. The results obtained with this system are presented in Chapter 5 and in part of Chapter 6. The sapphire characterization measurements can be shared with the crystal growing companies in order to optimize the production and improve KAGRA substrates.

2.3 R&D for KAGRA

Several upgrades for improving the sensitivity of gravitational wave detectors are currently under investigation. The goal of R&D effort is to reduce the limiting noises in order to lower the total sensitivity curve. Even if the commissioning of KAGRA is not completed yet, the KAGRA collaboration is considering in advance the possibilities of further improvement of the interferometer sensitivity.

- Increasing the input laser power is planned for LIGO and VIRGO because it reduces the shot noise, but it increases the radiation pressure noise. For KAGRA this is not a viable path in the nearest future because it would bring more problems for the cooling of the test masses.

- The use of larger test masses reduces the coating thermal noise for having a larger reflecting surface. Larger test masses are also heavier, and this is good for reducing the radiation pressure noise. The amount of changes of the interferometer required to increase the size of the mirrors makes this upgrade possible only in the long term.

- It has been demonstrated that the injection of a frequency dependent squeezed vacuum through the dark port of the interferometer will improve the sensitivity at both high frequencies and low frequencies. This upgrade is able to reduce both the shot noise and the radiation pressure noise, but it requires the construction of a squeezing source and a 300 m-long under-vacuum filter cavity. A prototype of the cavity is being constructed at NAOJ, inside the infrastructure of the TAMA300 interferometer.

- Current detectors employ amorphous multilayer optical coatings, metal oxides such as SiO_2 and TiO_2-alloyed Ta_2O_5, deposited by ion-beam sputtering [25, 26]. Since the coating thermal noise depends on the mechanical losses, new

materials with lower losses have been widely investigated. As explained in detail in Chapter 6, high-reflectivity interference coatings based on substrate-transferred crystalline coatings are a very promising material to reduce the coating thermal noise. Such new coatings, made of several layers of crystalline AlGaAs, have already demonstrated significant reductions in mechanical losses down to $\phi = 2.5 \times 10^{-5}$ at room temperature [27], and the potential for a loss angle of 4.5×10^{-6} at cryogenic temperatures [28].

2.3.1 Sensitivity improvement

As seen before in Figure 2.2, the sensitivity curve of an interferometer is calculated by summing all the noises. An interferometer upgrade improves the sensitivity as it reduces one or more noises. The possible sensitivity improvement is quantified by how much the sensitivity curve moves downward. In Figure 2.5, there is the estimation of the impact that some of the upgrades will have on KAGRA sensitivity.

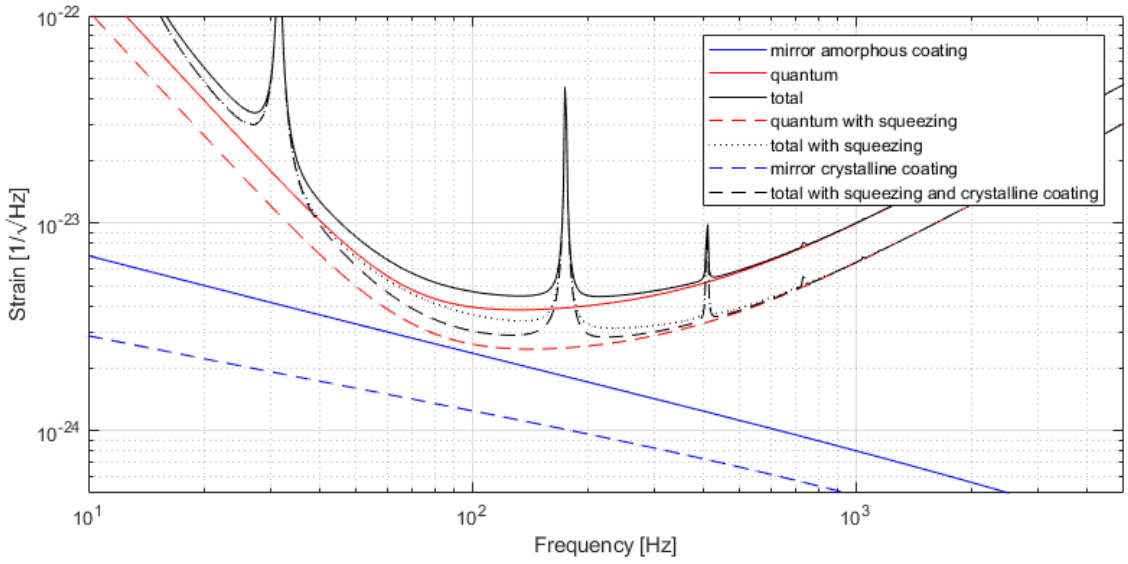

Figure 2.5: KAGRA sensitivity curve estimation after applying the upgrades studied in the R&D.

To summarize the sensitivity in a number, it is useful to calculate the maximum distance at which a gravitational wave source can be detected with the given noise. The usual way to calculate it is to take two kinds of events: the Binary Black Hole merger and the Binary Neutron Star merger. For each kind of event the following

formula is used [29]

$$D = \frac{1}{\rho}\frac{(G\mathcal{M})^{5/6}}{c^{3/2}\pi^{2/3}}\sqrt{\frac{5}{6}\int_{f_{\rm low}}^{f_{\rm high}}\frac{f^{-7/3}}{S(f)}df} \tag{2.2}$$

where ρ is the signal to noise ratio which is conventionally set as 8, $S(f)$ is the sensitivity curve as a function of the frequency f, $\mathcal{M} = \mu^{3/5}M^{2/5}$ is the chirp mass, $\mu = \frac{M_1 M_2}{M_1+M_2}$ is the reduced mass of the binary system, and M is the total mass in solar masses. This formula takes in account the sensitivity spectrum and the range of frequencies from $f_{\rm low}$ to $f_{\rm high}$ that a inspiral merge typically emits. In Table 2.1 there are the results of this calculation. The horizon value increases for every upgrade applied to KAGRA. The crystalline coating thermal noise is calculated using Equation 1.91 and the mechanical losses $\phi = 4.5 \times 10^{-6}$ at cryogenic temperature given by G Cole et al. [27].

	BBH [Gpc]	BNS [Mpc]
bKAGRA (BRSE)	2.26	289
bKAGRA + squeezing	2.89	374
bKAGRA + crystalline coatings	2.41	310
bKAGRA + squeezing + crystalline coatings	3.12	425

Table 2.1: Horizon for two kinds of events, BBH and BNS, in several cases of upgrade of KAGRA. The values corresponding to "bKAGRA (BRSE)" are calculated using the current bKAGRA design sensitivity, which employs amorphous coatings and don't use squeezing. The other values are calculated using the expected sensitivity curves in the cases of applying the squeezing and/or the crystalline coating upgrade.

After the frequency dependent squeezing upgrade will be applied, at mid frequencies in the sensitivity spectrum, the coating thermal noise will be an important limitation. Looking at Table 2.1 we notice that the BNS horizon, when the crystalline coating is used, improves by 7% (from 289 Mpc to 310 Mpc); but after the squeezing upgrade, the BNS horizon improvement due to crystalline coatings will be 14% (from 374 Mpc to 425 Mpc). In other words, after the quantum noise is reduced, the crystalline coatings will be a great step forward in terms of sensitivity.

2.3.2 Thesis motivation: crystalline coatings

The sensitivity improvements estimation shown in Table 2.1 motivates the effort of R&D on the crystalline coating test and development. The high purity of the materials and the large size of the test masses poses a technological challenge for

the fabrication process. Small scale crystalline coatings have been proved to have very low thermal noise, but, in order to be applicable to KAGRA, their size should be of the order of the test masses, which are 22 cm in diameter. So far, the largest size of 2 inches in diameter was achieved by the CMS company. It is important that as the size increases, the optical performances keep satisfying the requirements for a gravitational wave detector. As we explain in Chapter 6, these requirements are: less than 1 ppm of absorption; less than 10 ppm of scattering, therefore very low micro-roughness; and less than 1 defect/mm^2. During this thesis work, we characterized these large size crystalline coatings. In collaboration with the manufacturer and several laboratories, we performed many tests, such as transmission, scattering, defects, roughness, absorption and thermal noise measurements.

Given the high finesse of the optical cavity, most of the optical power density is concentrated on the reflective coating. For this reason, the absorption is a critical requirement for the coating. In order to have an efficient cooling of the test masses, the requirement for the coating absorption is less than 1 ppm. Current amorphous coatings fulfill these requirements, but the new crystalline coatings must be measured. We developed the system for the measurement of absorption maps in sapphire substrates, and upgraded it to measure also absorption maps of GaAs samples such as the crystalline coating. The system upgrade is described in Chapter 4 and the results on crystalline coatings are reported in Chapter 6.

Chapter 3

Optical absorption measurement system

During this thesis work, we developed and tested an absorption measurement system in the laboratory of TAMA300, in the Mitaka Campus of the National Astronomical Observatory of Japan (国立天文台). The setup initial configuration has been developed by the Stanford Photo Thermal Solutions (SPTS) company. This chapter describes the working principle, the experimental details, and some first results of the initial setup of this experiment. The last section of this chapter is a report about the numerical simulations performed in order to deeply understand the setup, and optimize the parameters to get the best absorption signal. After this preliminary study, the system has been upgraded to measure the absorption of KAGRA sapphire mirrors and new AlGaAs crystalline coatings. The upgrade details are reported in Chapter 4, while the measurement results are in Chapter 5 and Chapter 6.

3.1 Introduction

The optical absorption of a material is the transformation of part of the incident optical power into heat. The way to measure absorption is to sense how much the temperature increases when a laser goes through the material. When the temperature change is small, of the order of few mK, a direct measurement with a thermometer might be inaccurate. In the case of optics, we can take advantage of the so-called *thermal lens effect*, which is caused by the fact that the refractive index depends on the temperature. For small temperature changes, we can consider the effect to be linear, which means $dn(T)/dT$ is a constant, at first approximation. The temperature distribution $u(x,t)$ follows the Gaussian shape of the heating source

(the laser beam) and evolves in time and space according to the heat equation

$$\frac{\partial u}{\partial t} = k\frac{\partial^2 u}{\partial x^2} + \frac{Q(x,t)}{c\rho} \tag{3.1}$$

where c is the heat capacity, ρ is the mass density, $k = \frac{K}{c\rho}$ is the thermal diffusivity and K is the thermal conductivity.

The resulting refractive index distribution produces a lens: the thermal lens. The perturbation that a laser experiences when passing through such thermal lens can be measured with a photo-detector. The detector output signal, conveniently processed, reveals the temperature change, which is proportional to the absorbed amount of optical power. The experimental setup developed in this thesis work is based on the photo-thermal common-path interferometer (PCI) method. In the next sections, the PCI method is presented in detail.

3.2 Working principle of the PCI

The high power laser beam that is partially absorbed by the sample is called *pump* and it generates the temperature distribution inside the sample. The pump is modulated in intensity by an optical chopper at a fixed modulation frequency so that the temperature change is periodical in time. At the same time, another laser, called *probe*, crosses the pump beam inside the material, with an angle of about 0.1 rad. Because of the refractive index gradient, the probe experiences a non-uniform phase shift. Both the waist of the pump and the waist of the probe are located at the crossing point. The pump waist is much smaller than the probe, experimentally it is about 3 times smaller. This means that the central part of the probe gets a higher phase shift. Right after the heated region, the phase shift doesn't affect the beam intensity, but after some propagation, the beam shape is distorted. This distortion is proportional to the absorption rate. An interpretation of this distortion is that the thermal lens focuses the laser with a focal length proportional to the refractive index gradient so that the beam shape changes after some propagation. Another interpretation of this method is the model described in the following subsection. The heated area creates a perturbation in the center of the probe which makes interference with the probe itself. This interpretation gives the method the name of Common-path Interferometer.

3.2.1 Simple model

A simplified model of what happens can be derived writing the form of the probe Gaussian beam, and calculating the propagated beam after the heated sample. Let's start writing down the probe laser incident electric field

$$E_{\text{in}}(x, y, z_0) = Ae^{-ikz_0}e^{-\frac{x^2+y^2}{w^2(z_0)}}e^{i\psi(z_0)} \tag{3.2}$$

where A is a constant, k is the wave vector, w is the beam radius, and ψ is the Gouy phase. Immediately after the sample, the beam will get a phase shift due to the temperature distribution, so it will have the form

$$E_{\text{out}}(x, y, z_0) = Ae^{-ikz_0}e^{-\frac{x^2+y^2}{w^2(z_0)}}e^{i\psi(z_0)}e^{i\phi(x,y)} \tag{3.3}$$

where the phase shift $\phi(x, y)$ follows the shape of the temperature distribution

$$\phi(x, y) = \phi_0 e^{-\frac{x^2+y^2}{w_P^2(z_0)}} \tag{3.4}$$

where w_P is the radius of the pump beam. Since the temperature change is very small, we can make the approximation that the phase shift is also small and expand the exponential

$$e^{i\phi(x,y)} \simeq 1 + i\phi_0 e^{-\frac{x^2+y^2}{w_P^2(z_0)}}. \tag{3.5}$$

So the electric field immediately after the sample (at the same $z = z_0$) is

$$E_{\text{out}}(x, y, z_0) \simeq Ae^{-ikz_0}e^{-\frac{x^2+y^2}{w^2(z_0)}}e^{i\psi(z_0)}\left[1 + i\phi_0 e^{-\frac{x^2+y^2}{w_P^2(z_0)}}\right] \tag{3.6}$$

multiplying the content of the squared bracket we get two terms: one is the main original beam that just passes through the sample; the second term is a perturbation: another Gaussian beam with a different waist w' that satisfies the relation

$$\frac{1}{w'^2} = \frac{1}{w^2} + \frac{1}{w_P^2} \tag{3.7}$$

and propagates differently with his own Gouy phase $\psi'(z)$. In our case, $z_0 = 0$ because the waist of the pump and the probe are both on the crossing point inside the sample, which is where the absorption signal is generated. At a distance z_d from

the crossing point, the beam will be

$$\begin{aligned} E_{\text{out}}(x,y,z_d) \simeq & Ae^{-ik(z_0-z_d)}e^{-\frac{x^2+y^2}{w^2(z_d)}}e^{i\psi(z_d)}+ \\ & Ai\phi_0 e^{-ik(z_0-z_d)}e^{-\frac{x^2+y^2}{w'^2(z_d)}}e^{i\psi'(z_d)}. \end{aligned} \tag{3.8}$$

Let's now take out a common factor

$$E_{\text{out}}(x,y,z_d) \simeq Ae^{-ik(z_0-z_d)}e^{-\frac{x^2+y^2}{w^2(z_d)}}e^{i\psi(z_d)}\left[1+i\phi_0 f(x,y)e^{i\Delta\psi(z_d)}\right] \tag{3.9}$$

with

$$f(x,y) = e^{-\frac{x^2+y^2}{w'^2(z_d)}}e^{\frac{x^2+y^2}{w^2(z_d)}} \tag{3.10}$$

and $\Delta\psi(z_d) = \psi'(z_d) - \psi(z_d)$.

In order to show the interference between the main beam and the perturbation, we calculate the beam intensity taking the squared modulus of equation 3.9. Using the Euler relation, the intensity can be written as

$$\begin{aligned} I(x,y,z_d) \simeq & e^{-2\frac{x^2+y^2}{w^2(z_d)}}\times \\ & \times\left[\left[1-\sin(\Delta\psi(z_d))\phi_0 f(x,y)\right]^2+\left[\cos(\Delta\psi(z_d))\phi_0 f(x,y)\right]^2\right], \end{aligned} \tag{3.11}$$

and dropping the quadratic terms in ϕ_0, we have

$$I(x,y,z_d) \simeq e^{-2\frac{x^2+y^2}{w^2(z_d)}}\left[1-2\sin(\Delta\psi(z_d))\phi_0 f(x,y)\right]. \tag{3.12}$$

There will be no interference when $\Delta\psi(z_d) = 0$, which means at the sample position, or when $\Delta\psi(z_d) = \pi$ which means at an infinite distance. There will be maximum interference when $\Delta\psi(z_d) = \pi/2$. If the pump beam waist is much smaller than the probe one, then $w' \simeq w_P$, and $\Delta\psi(z_d) = \pi/2$ when z_d is the Rayleigh length of the perturbation beam.

$$z_R = \frac{\pi w_P^2}{\lambda} \tag{3.13}$$

where λ is the probe laser wavelength and w_P is the pump laser waist.

In order to detect the maximum interference, the detector should be placed at this distance, but the experimental conditions don't allow to put the detector so close to the pump/probe crossing point. In order to overcome this problem, it is convenient to reproduce the image of the interference far away from the sample and put the detector there. The image is reproduced with a telescope made of a

converging lens, that focuses the beam onto a small convex spherical mirror. The spherical mirror reflects the beam and makes it large on the detector. The distance between the lens and the sphere determines where the image is formed. This imaging unit is placed far enough from the sample, in order to avoid intersections with the pump beam. The total intensity of the probe beam doesn't change, so the intensity of the central part of the laser spot is what has to be measured. Indeed, before the detector, there should be a diaphragm to select the central part of the beam, but actually, the size of the detector itself plays the role of the diaphragm. Figure 3.1 represents the working principle and optical configuration of the PCI method.

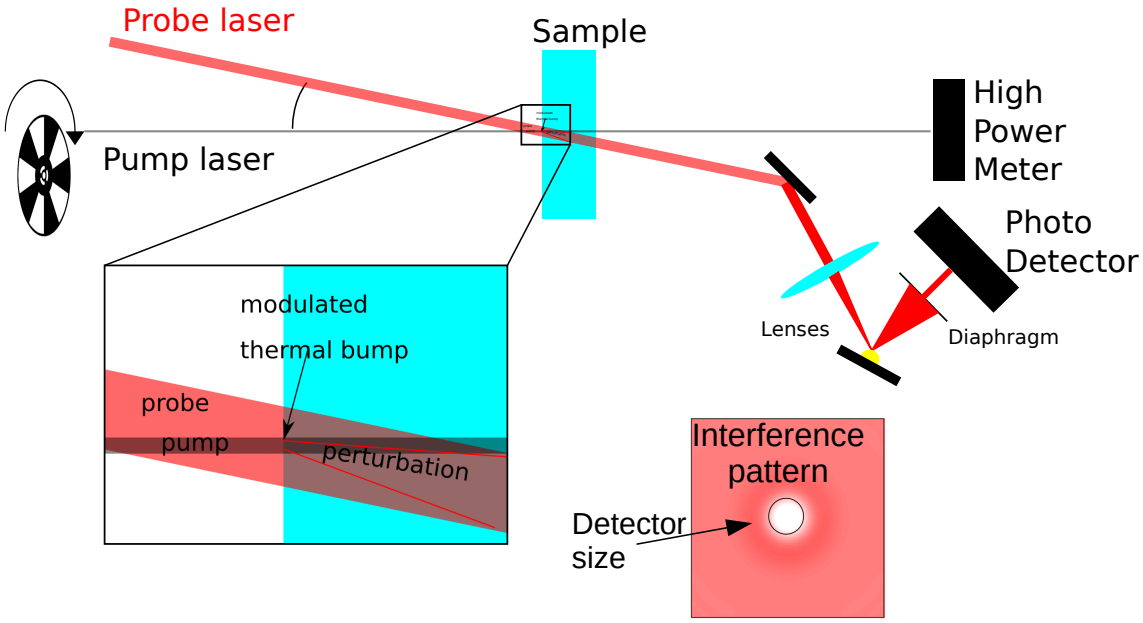

Figure 3.1: Photo thermal common-path interferometer (PCI). This concept diagram represents the core of the system. The pump is modulated by the optical chopper, goes through the sample, heats it up and ends on the power meter. The zoomed part shows that the probe crosses the pump inside the sample. The thermal bump creates the small perturbation. Notice that the pump is smaller than the probe. The imaging unit is made by a converging lens, a small sphere, and the PD. The imaging unit creates the image of the interference pattern on the PD. The size of the PD is smaller than the probe spot (as if there was a diaphragm) and it senses the intensity variation of the central part of the beam.

The detector signal is sent to a lock-in amplifier, which mixes it with the chopper reference signal and returns 3 signals: the DC, the demodulated AC, and the phase. The DC is the continuous component of the detector signal and it is proportional to the probe laser power, to the detector efficiency and to the load resistance. The

AC is actually the quadrature sum of the X signal and the Y signal which are the demodulation of the PD signal respectively with a cosine and with a sine at the modulation frequency and locked in phase with the chopper. The AC is the demodulation of the component that oscillates at the modulation frequency (from the optical chopper). Since it is proportional to the laser power, dividing it by the DC signal cancels out all the factors (like electronic gains or efficiency) that come from the detector and from the lock-in amplifier. The ratio AC/DC is proportional to the amplitude of the temperature oscillation. Therefore it is proportional to the absorption rate Abs and the pump laser power P. Given the above considerations, the absorption rate is calculated by using the simple formula

$$\mathrm{Abs}[\mathrm{cm}^{-1}] = \frac{AC[\mathrm{V}]}{DC[\mathrm{V}] \cdot P[\mathrm{W}] \cdot R[\mathrm{cm/W}]} \tag{3.14}$$

where R is the calibration factor that depends on other experimental parameters like the beams sizes, the modulation frequency, the sample thermal properties, and the alignment. The calibration factor is determined experimentally by measuring a sample with a known absorption value and reversing equation 3.14. The power P should be taken where the signal is generated. In the case of surface absorption, P is the incident power, but in the case of bulk absorption, it is the power inside the sample, which is calculated multiplying the incident power by the square root of the measured transmission. This will take into account of the Fresnel reflections and, in case of large absorption, the pump depletion.

3.3 Experimental setup

The setup makes use of two lasers, the pump that heats up the sample, and the probe that senses the thermal variations. In this section, the lasers configuration and alignment are described. In Figure 3.2 there is a picture of the original setup from the SPTS company. The pump laser is a high power fiber laser at 1064 nm from the company OXIDE. The laser is controlled by a LabVIEW-based software that communicates with the device through a serial port. The temperature is controlled and the diode current can be set from the PC, up to 7.5 A, with a corresponding maximum power of 20 W. The laser diode threshold is 0.7 A. The output comes to the optical table through an optical fiber. The adjustment of the laser power is done using two polarizing plate beam splitters (PBS) and a half-wave plate in the middle of them. Rotating manually the half-wave plate, the power reflected by the

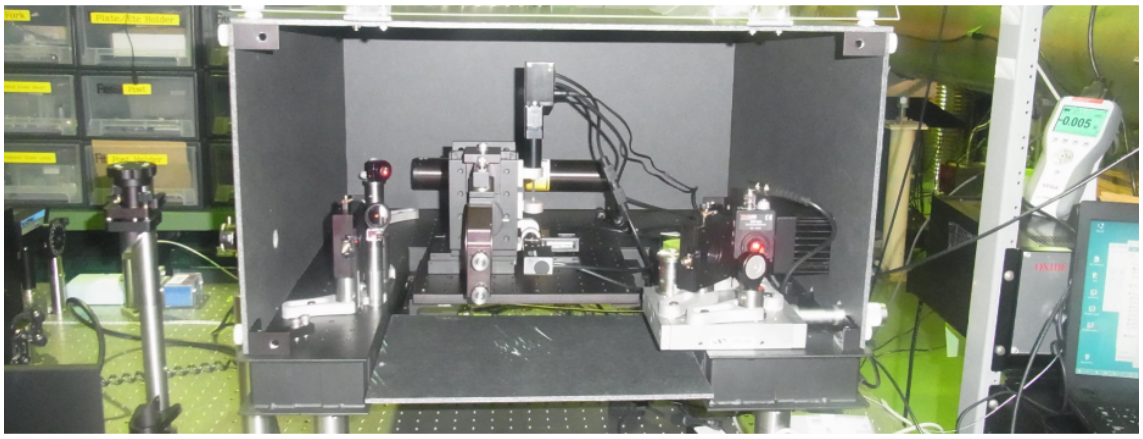

Figure 3.2: Original setup from SPTS with HeNe probe laser for small optics.

second PBS is regulated. Then the laser passes through a converging lens to keep it collimated and then it passes through an optical chopper (SR540) that modulates the amplitude as a square wave. The reference signal of the chopper is sent to the lock-in amplifier with a BNC cable. A periscope brings the laser to a higher optical breadboard. On the breadboard, there is the core of the system. The last lens for the pump focalizes it to the sample, the size of the beam at the waist is 70 µm in diameter. After the sample position, there is a power meter to measure the pump optical power. The optical configuration of the pump beam path is shown in Figure 3.3. The probe laser is a Helium-Neon laser at 633 nm with a power of 5 mW. It is led to the sample position where it crosses the pump beam at the pump beam waist. The angle between the two lasers is 6°. It is focused with a lens in order to have the waist at the crossing point. As explained in the previous section, the point where there is the maximum interference needs to be re-imaged far away from the sample. At about 200 mm from the crossing point there is the imaging unit. The imaging unit is made of a prism mirror that redirects the probe beam to a lens. The lens is mounted on an XY translation mount, the focal length is 50 mm. The beam is focused on a small spherical mirror of radius 2.5 mm which make the beam diverge toward the detector. At the detector, the beam is large enough so that the detector can measure only the central part of the spot. The detector is a Si Biased detector, model DET10A from Thorlabs. The signal is sent to the lock-in amplifier with a BNC cable. The sample to be measured is attached at a motorized translation stage, Zaber T-NA [30], that can move along the three axes X, Y, and Z for a range of 50 mm in each direction. The stage is controlled through the serial port, by a LabVIEW-based software.

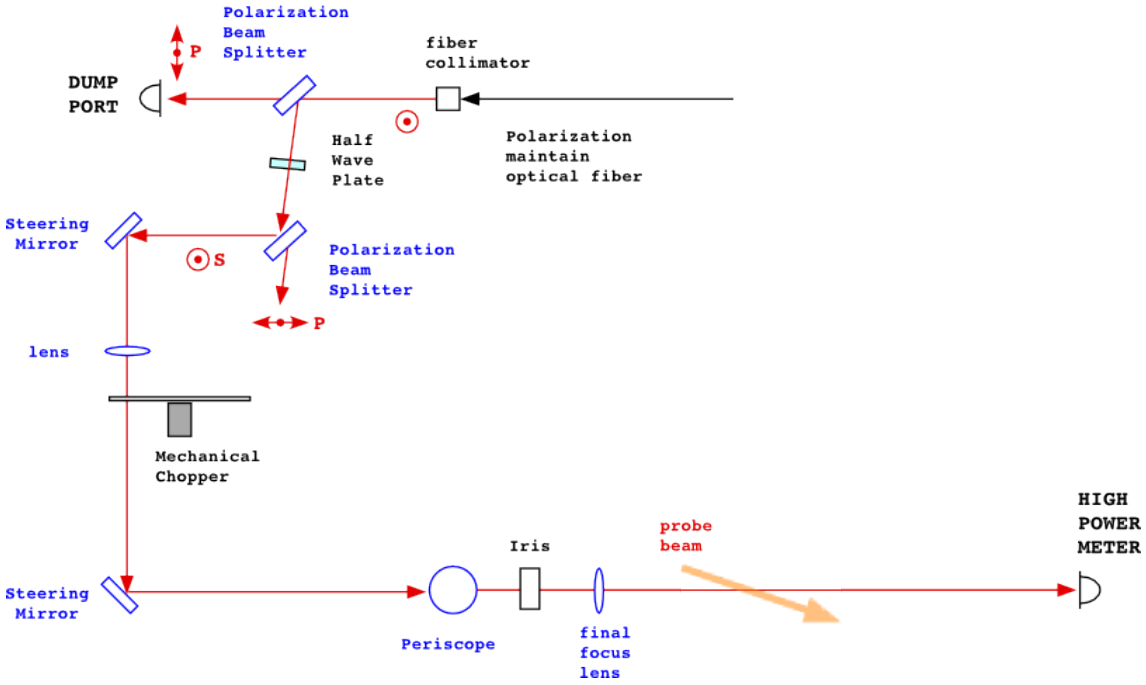

Figure 3.3: Optical configuration of the pump beam. The laser fiber output is mostly vertically polarized (s-polarization), the first PBS cleans the residual p-polarization that is transmitted and dampened. The amount of s-polarized light reflected by the second PBS depends on the rotation angle of the half-wave plate. The steering mirrors are used for alignment. The lenses are placed in order to have the pump waist at the crossing point with the probe. Finally, the beam ends on the power meter. Drawing credit: D.Tatsumi.

3.3.1 Alignment procedures

The procedure to align the beams in order to have the maximum absorption signal to noise ratio consists of some steps to be done in sequence. The initial configuration alignment was done by the SPTS company, but then these procedures have been made again as part of this thesis work for the upgrade to the new configuration reported in Chapter 4.

First of all, the focusing lenses of the two lasers are chosen to have the waist at the same position, the crossing point. The last lens of the pump is mounted on an XY translation mount to perform the finest adjustment of the pump beam position. A pin-hole of 200 µm in diameter is attached at the translation stage and it is moved to the position where the pump waist is. Then the probe is aligned to pass through the same hole at 6° with the pump. Since the pin-hole is larger than the beams, this alignment has to be finely improved. The probe goes to the imaging unit and it is focused on the small spherical mirror using a 50 mm lens mounted on an XY translation mount that moves the lens laterally. The direction of the reflected beam from the sphere strongly depends on the position of the beam on the surface of the sphere. So, adjusting the position of the lens, the beam is directed and centered on the photo-detector. Since the absorption signal is maximum when the detector measures the central portion of the beam, we center the beam on the PD by adjusting the lens XY position and maximizing the DC signal from the photo-diode. To have the correct image of the interference at the PD, the distance between the lens and the sphere is crucial. The procedure is to put a blade that covers half of the probe beam at the position calculated in equation 3.13, and to see on the PD a sharp image of the blade shadow. The distance between the lens and the sphere is adjusted until the shadow is sharp. The fine adjustment is done maximizing the signal as a function of the total imaging unit position. Last alignment step is to place a surface absorption sample (usually the calibration reference) at the crossing point, and maximize the AC signal by centering the position of the pump beam using the pump focusing lens. Every time we change sample, the DC signal has to be maximized.

3.4 Calibration

The SPTS company provides the reference samples for the calibrations, one for surface absorption and one for bulk absorption.

The absorption of the two samples is measured also with a spectrophotometer at NAOJ, which measures transmission $T(\%)$ and reflection $R(\%)$; then the absorption is given by $A(\%) = 100 - T(\%) - R(\%)$. The samples have a high absorption rate, so it's necessary to use a pump power below the damage threshold of the samples, so 30 mW is used. The same calibration measurement is done on different days and the repeatability is calculated. In Figure 3.4 the typical calibration scan is shown.

- Surface absorption: Newport FRQ-ND02 coated with Inconel
  Nominal absorption: 22.2 % at 1064 nm
  Spectrophotometer measurement: 22.0 % at 1064 nm
  Thickness: 3 mm
  Calibration factor R= 11 W^{-1}
  Repeatability: 10 %

- Bulk absorption: Schott glass NG-12
  Nominal absorption: 116 %/cm at 1064 nm
  Spectrophotometer measurement: 104 %/cm at 1064 nm
  Thickness: 3.6 mm
  Calibration factor R= 0.5 cmW^{-1}
  Repeatability: 3 %

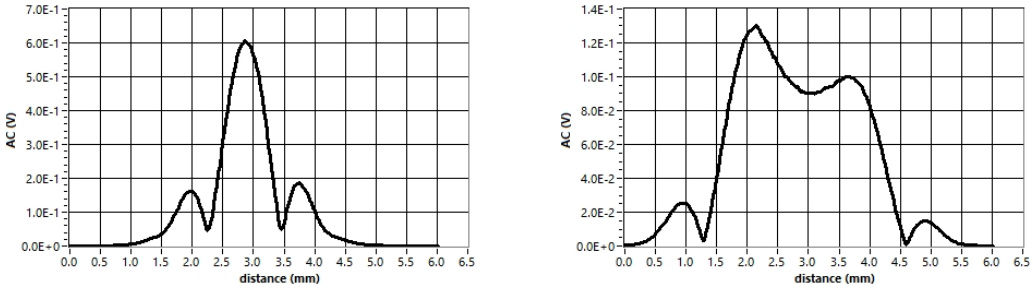

(a) Surface reference (b) Bulk reference

Figure 3.4: Reference samples typical absorption signal as a function of the position of the sample along the z-axis.

3.5 Thick sample issues

The system is capable of measuring the absorption of samples with different sizes. Because of the sample's higher refractive index, the probe undergoes an optical path

change which scales with the sample thickness. As explained in the previous section, the photo-detector measures the intensity of the central part of the probe, and the signal depends on the relative size of the detector with respect to the probe. In order for the calibration to be valid, the size of the probe at the detector must always be the same. When we put a thick sample, the size of the probe at the detector becomes smaller. So, in order to recover the original size, the detector is moved backward. A qualitative representation of the effect is shown in Figure 3.5. The position correction value can be calculated by using the ABCD matrix formalism.

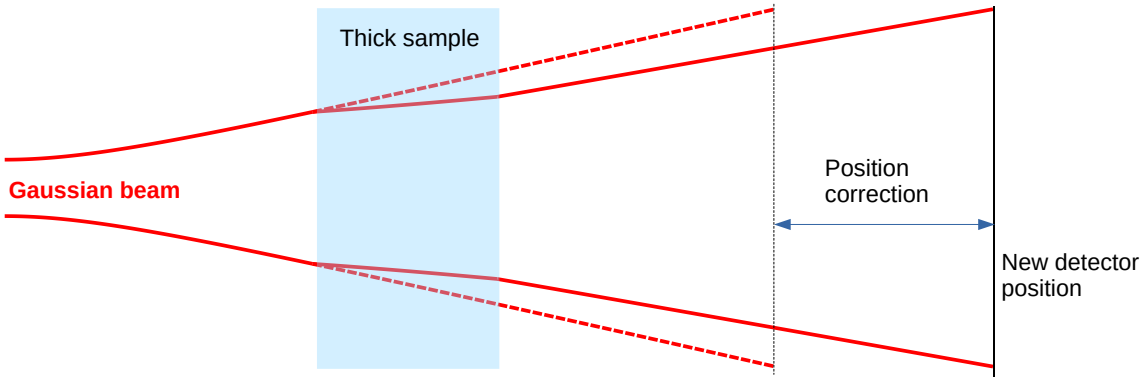

Figure 3.5: Correction of the detector position. When the beam passes through a thick material, the position where the beam has the same size moves according to the thickness and the material refractive index. The solid red lines represent the beam going through the thick sample, while the dashed red line represents the beam profile in absence of the sample.

- In the case of propagation without the sample, the ABCD matrices that describe the probe optical path are:

$\begin{pmatrix} 1 & \mathrm{d1} \\ 0 & 1 \end{pmatrix}$ propagation from the sample until the converging lens

$\begin{pmatrix} 1 & 0 \\ -1/\mathrm{f1} & 1 \end{pmatrix}$ trough the lens

$\begin{pmatrix} 1 & \mathrm{d2} \\ 0 & 1 \end{pmatrix}$ propagation from the lens to the spherical mirror

$\begin{pmatrix} 1 & 0 \\ -1/\mathrm{f2} & 1 \end{pmatrix}$ reflection on the spherical mirror

$\begin{pmatrix} 1 & \mathrm{d3} \\ 0 & 1 \end{pmatrix}$ propagation from the sphere to the detector

The product of all these ABCD matrices gives the total path matrix without the sample.

- In the case of propagation through the thick sample:

$\begin{pmatrix} 1 & 0 \\ 0 & 1/\mathrm{n} \end{pmatrix}$ changing refractive index entering in the sample

$\begin{pmatrix} 1 & \mathrm{L} \\ 0 & 1 \end{pmatrix}$ propagation from the sample until the converging lens

$\begin{pmatrix} 1 & 0 \\ 0 & \mathrm{n} \end{pmatrix}$ changing refractive index exiting from the sample

$\begin{pmatrix} 1 & \mathrm{d1}-\mathrm{L} \\ 0 & 1 \end{pmatrix}$ propagation inside the thick sample

$\begin{pmatrix} 1 & 0 \\ -1/\mathrm{f1} & 1 \end{pmatrix}$ trough the lens

$\begin{pmatrix} 1 & \mathrm{d2} \\ 0 & 1 \end{pmatrix}$ propagation from the lens to the spherical mirror

$\begin{pmatrix} 1 & 0 \\ -1/\mathrm{f2} & 1 \end{pmatrix}$ reflection on the spherical mirror

$\begin{pmatrix} 1 & \mathrm{d3} \\ 0 & 1 \end{pmatrix}$ propagation from the sphere to the detector

The product of all these ABCD matrices gives the total path matrix with a

L-thick sample with refractive index n.

Then using the formulas for the complex beam parameter

$$\frac{1}{q(z)} = \frac{1}{R(z)} - \frac{i\lambda_0}{\pi n w(z)^2} \tag{3.15}$$

$$q_f = \frac{Aq_i + B}{Cq_i + D} \tag{3.16}$$

we calculate the beam size w as a function of d1. Equating the waists and solving the equation for d1 (with the help of the software Mathematica® for the algebra), we find that the waist with the thick sample and the waist without the sample are equal when the distance d1 is shifted by

$$\mathrm{d_{shift}} = \frac{(\mathrm{n}-1)\mathrm{L}}{\mathrm{n}} \tag{3.17}$$

This result doesn't depend on the initial beam parameters, so it is valid for both the main beam and for the perturbation. Applying this correction recovers the interference pattern or intensity, so the calibration is valid. To perform this shift, the imaging unit (lens, sphere, and detector) is placed on a micrometric translation stage, whose position is adjusted whenever the sample thickness changes. Another effect of the sample thickness is about the refraction of the probe according to the Snell's law. Since the pump is perpendicular to the sample surface but the probe has a non-zero incidence angle, the crossing point position inside the sample depends on how much material the probe has traveled in before crossing the pump. In Figure 3.6 there is a diagram of the situation. The Snell's law is

$$\sin(\alpha_0)n_0 = \sin(\alpha_1)n_1 \tag{3.18}$$

where α_0 and α_1 are the probe angle outside the sample and inside the sample, n_0 and n_1 are the refractive index outside the sample and inside the sample. Applying the Snell's law to the geometry represented in Figure 3.6, in the case of sapphire, $n_1 = 1.76$, and incidence angle $\alpha_0 = 6°$, we get

$$X_1 = X_0\frac{\tan(\alpha_0)}{\tan(\alpha_1)} = X_0\frac{n_1}{n_0}\frac{\cos\left(\arcsin\left(\frac{\sin(\alpha_0)n_0}{n_1}\right)\right)}{\cos(\alpha_0)} = X_0 \cdot 1.81 \tag{3.19}$$

The result of this simple calculation shows that to make a complete scan of a thick sample, it is necessary to move the sample by 1.81 times less than the sample

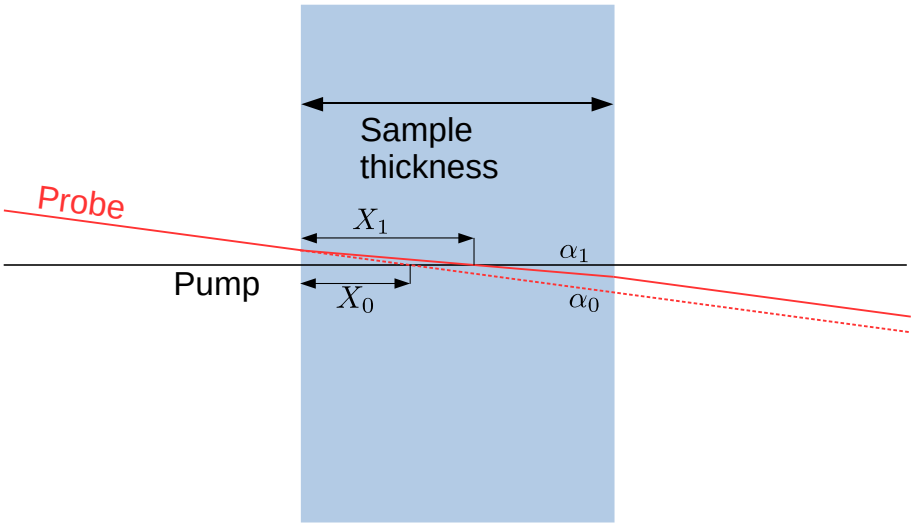

Figure 3.6: Apparent position of the crossing point inside the sample. X_0 is the distance between the sample first surface and the pump-probe crossing point if the sample had refractive index 1. X_1 is the real distance between the first surface of the sample and the pump-probe crossing point.

thickness. For example, a 150 mm-thick KAGRA substrate needs to be translated by 83 mm to get a scan from one surface to the other.

3.6 Absorption test measurements

Since the reference samples have a very high absorption rate, it is useful to measure very low absorbing samples that are already measured with another method. So it is possible to investigate the sensitivity of the system and see if the calibration changes when the pump power changes, and also compare the two different methods.

3.6.1 LMA Samples

The samples provided by Laboratoire des Matériaux Avancés (LMA) are 3 coated surface samples and a bulk sample and they are measured at LMA with the Photo Deflection system:

Coating

- ref 15034/1 absorption @ 1064 nm = 0.65 ppm
- ref 15033 absorption @ 1064 nm = 12.8 ppm
- ref 15032/2 absorption @ 1064 nm = 4.5 ppm

Bulk

- VIRGO BN40556 Suprasil312 Mat.ID 90160122 n2
  absorption @ 1064 nm = 1.5-1.6 ppm/cm

Surface samples In Figure 3.7 there are the maps of the coated samples, the spatial resolution is 70 µm, which is the size of the pump beam.
In all the samples there are many absorption peaks of the order of hundreds of ppm. Table 3.1 shows the comparison of the measure with the Photo Deflection system at LMA and the measure with the Photo-thermal Common-path Interferometer system at NAOJ. The value is the mean of the scanned area calculated excluding the peaks. The comparison shows that the PCI method gives always a slightly higher value, the reason seems to be a difference in the calibration.

Sample	**PD (LMA)**	**PCI (NAOJ)**
ref 15034	0.65 ppm	0.85 ppm
ref 15032	4.5 ppm	5.4 ppm
ref 15032	12.8 ppm	14 ppm

Table 3.1: Surface absorption measurement comparison for the two methods.

In order to understand the reason of the absorption peaks the same map of sample #15034 is measured before and after cleaning the surface with the First Contact polymer. As shown in Figure 3.8 the absorption after cleaning is lower, but the peaks remain.

The surface of sample #15034 was watched at the microscope, the entire surface of the sample is reconstructed assembling many microscope pictures, as shown in Figure 3.9(b), many dots on the surface suggest that the absorption peaks are given by the defects on the coating. In the absorption system, the boundary of the sample is measured taking the map of the DC signal of the probe; the pump was OFF, otherwise uncontrolled reflections of the pump could burn something, Figure 3.9(a). The broken boundaries of the sample helped to make a match of the two maps. In Figure 3.9(c) there is the comparison with the correspondent area at the microscope. Unfortunately, it's not easy to see a good correspondence between the dots and the absorption peaks.

Bulk sample The sample Suprasil312 is measured, the absorption measured at LMA is 1.5 ppm. Figure 3.10 shows a scan along the z-axis; it's possible to see the

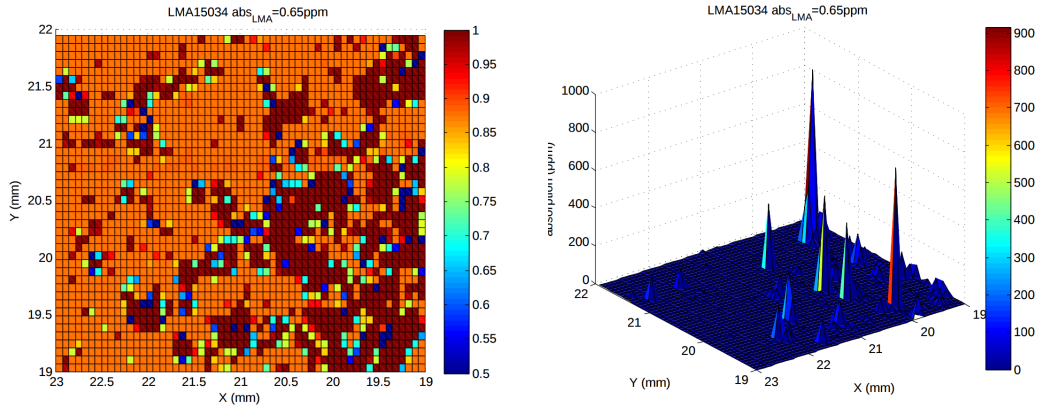

(a) Sample #15034

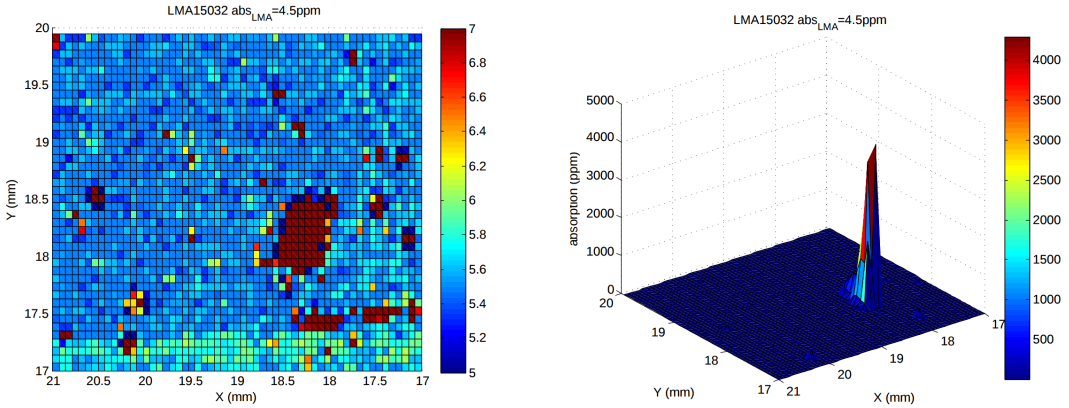

(b) Sample #15032

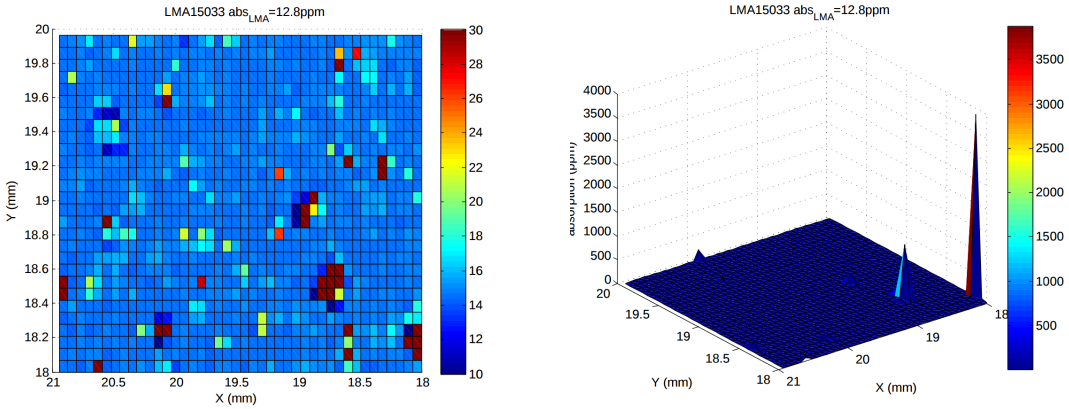

(c) Sample #15033

Figure 3.7: LMA surface samples absorption maps.

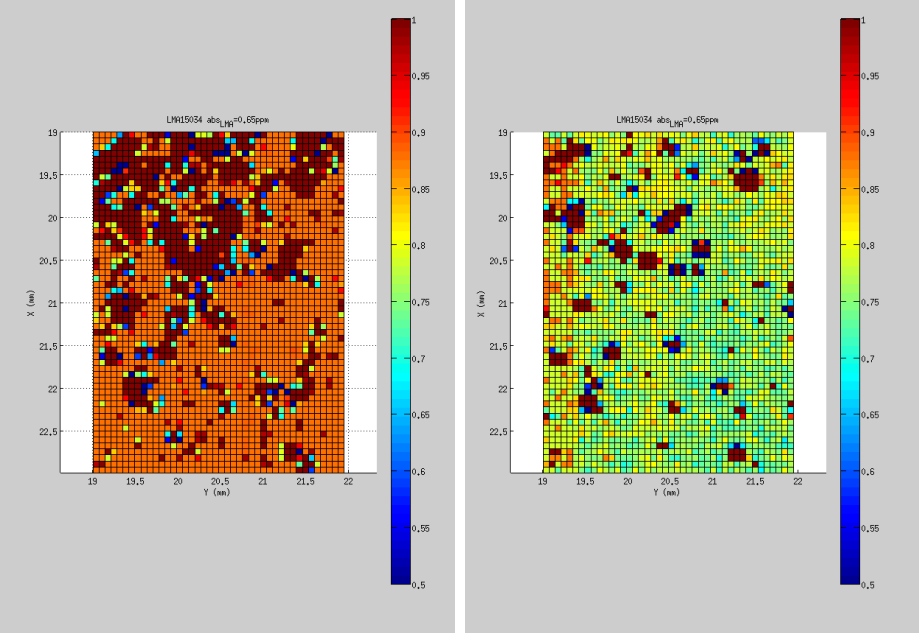

Figure 3.8: Surface map of sample #15034 before (left) and after (right) cleaning with the first contact.

thickness of the sample (20 mm). The noise level is about 1 ppm and the value in the bulk is 4 ppm, so the measured absorption rate is 3 ppm, different from the one measured at LMA. There is a huge absorption on the surface of the sample (even after cleaning the sample with the First Contact). This is probably due to some remaining glue residuals from the fabrication and polishing procedures.

3.6.2 Sapphire sample

The main goal of the system at NAOJ is to measure the sapphire absorption of KAGRA mirrors. As a first test, a small sample of Sapphire made by the Japanese company Shinkousha (信光社) has been measured.

Figure 3.11(a) shows the scan along the z-axis, with the typical shape of bulk absorption. In Figure 3.11(b) there is the map with a resolution of 200 µm, this map has been made twice and the difference (Figure 3.11(c)) shows that the noise level is about 1 ppm. Figure 3.11(d) shows the same map but made with a higher resolution, 100 µm. The calibration factor used is $R = 0.5\,\mathrm{cm}W^{-1}$. The SPTS company provides also the calibration correction factor between the reference sample and other materials. The value for sapphire is 3.34. The minimum of absorption is 37 ppm/cm while the maximum is 310 ppm/cm. The conclusion is that the sample is not homogeneous. The company is improving the quality of Sapphire, so other

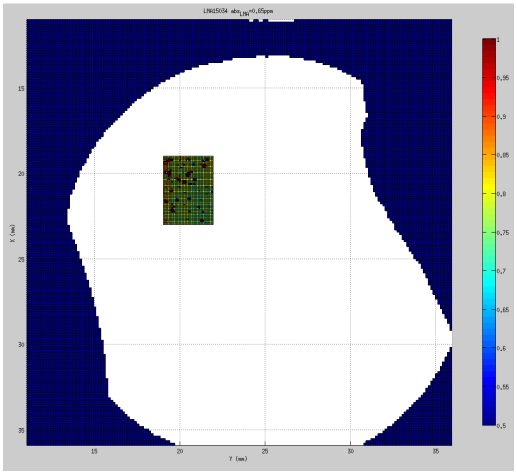

(a) PCI system map

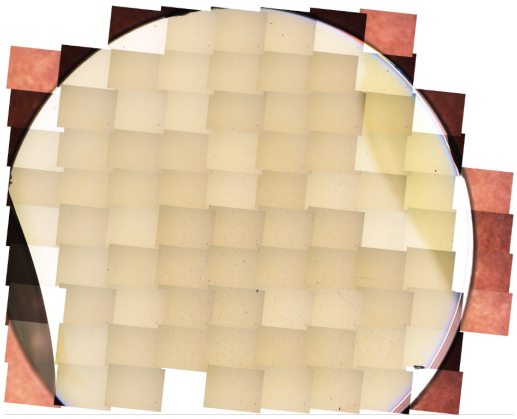

(b) Microscope map

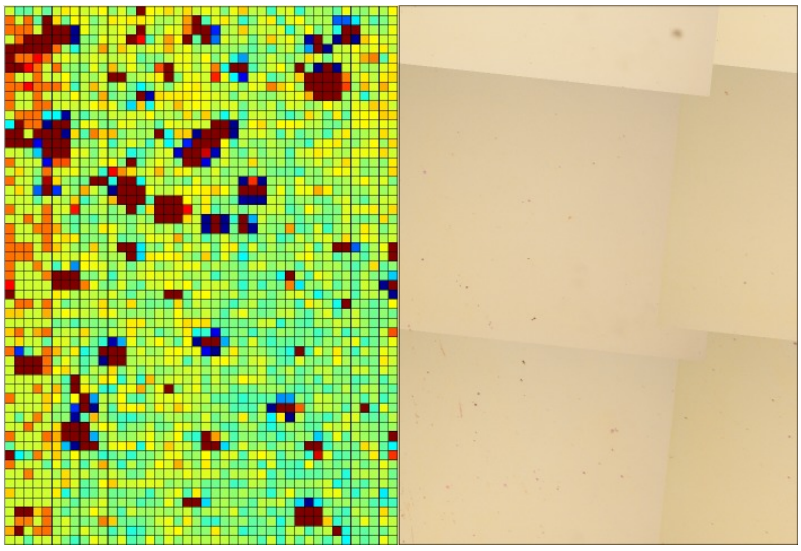

(c) Comparison

Figure 3.9: Sample #15034. We took a 4 mm×3 mm absorption map on the mirror (a). Then we took many pictures at the microscope to reproduce the total surface (b). Then we could compare the absorption and the picture of the corresponding areas (c). Unfortunately there is not a clear correspondence between the absorption peaks and the dots on the picture.

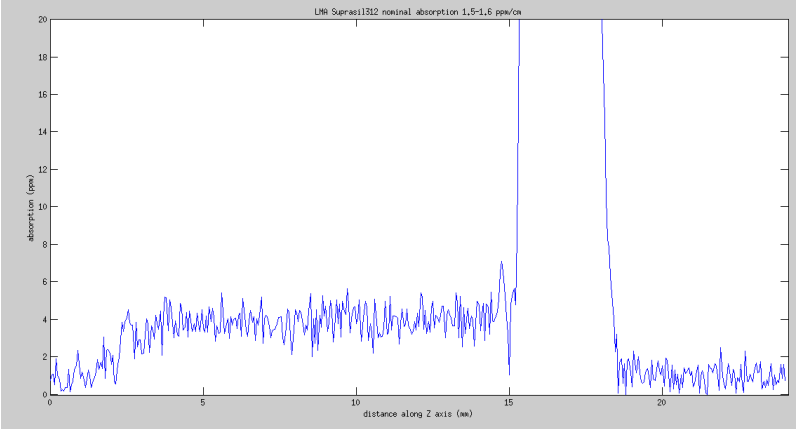

Figure 3.10: Sample Suprasil312 scan. There is a small absorption rate in the bulk, near the noise level, and a huge absorption on the surface, probably due to some glue residual from the polishing process

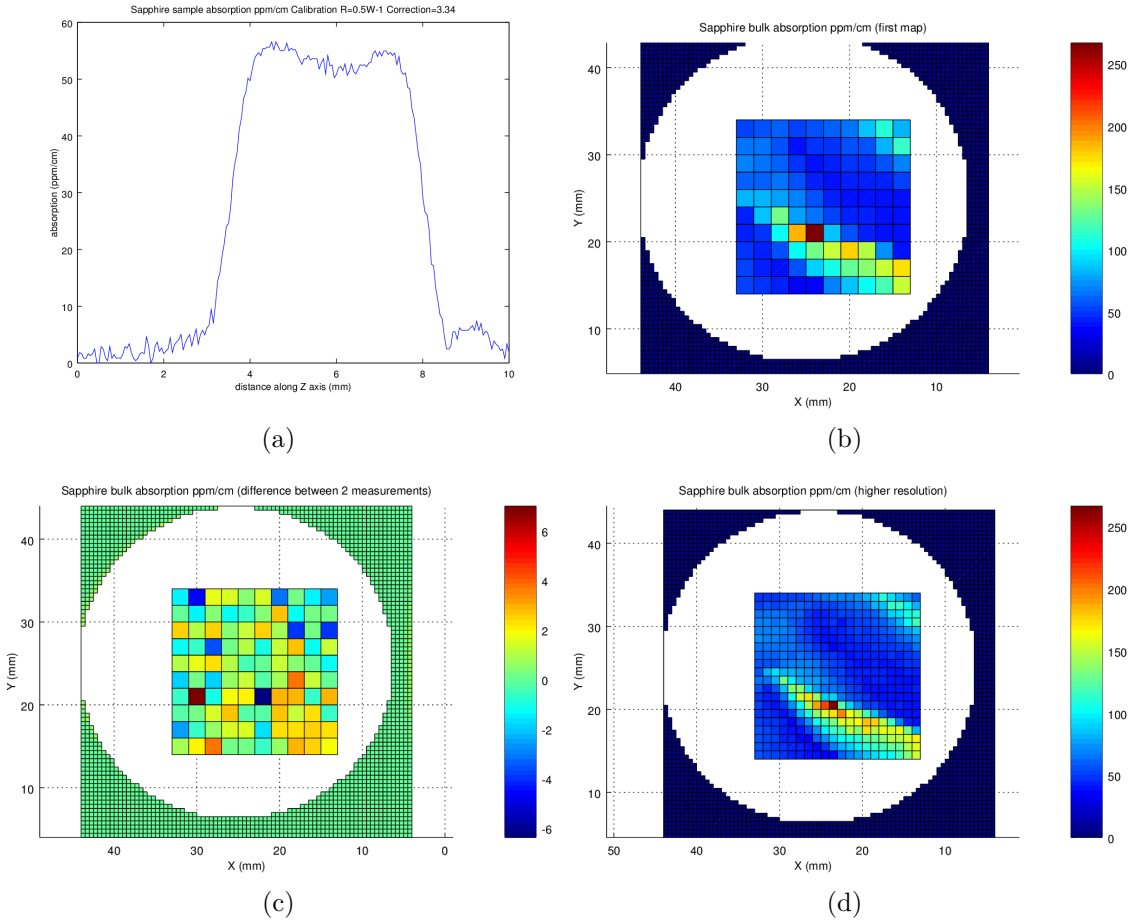

Figure 3.11: Sapphire sample from Shinkousha. (a) the scan along the z-axis. (b) map with a resolution of 200 µm. (c) difference between 2 measurement maps that shows the noise level. (d) higher resolution map, 100 µm.

samples will be measured.

3.7 Noise

To measure very low absorption rates such as the order of ppm, it is necessary to deal with several noise sources. The pump modulation with the chopper and the demodulation with the lock-in amplifier allow getting rid of most of the noise at any frequency different from the modulation one. But still, there are noise sources at the modulation frequency.

The stray light from the modulated pump reaches the PD and shows up in the lock-in amplifier output. This signal has a constant phase because it is in-phase with the chopper, but it's not an absorption signal. The way to remove this noise is to put optical filters in front of the PD to make only the probe wavelength pass. In Figure 3.12 there are the filters used on the HeNe probe detector.

Since the PD selects the central part of the beam spot, the system is very sensitive to vibrations which make positioning (or jitter) noise. To isolate the mechanical chopper vibrations that propagate through the optical table, we put a rubber sheet below the chopper. This solution was sufficient in the original setup, but, as we will see in the next Chapter, in the upgraded setup the chopper vibrations were isolated by hanging it at the ceiling, so that it doesn't even touch the optical table. During a scan or a map, the noise generated by the moving motors of the translation stage is reduced by setting a waiting time, usually between 100 ms and 1500 ms.

Another important precaution is to block any reflection of the probe to reach the chopper. This would generate a modulated stray light that would pass through the optical filters.

We did a systematic work of noise hunting. After filtering out the pump stray light, and isolating the chopper vibration, we looked for other noise sources: the clean booth filters rotating fans; the temperature fluctuations caused by the wind; the ground loops in the electric power supply; the dust crossing the probe. When the probe is off, the noise is 0.8 µV, and with the probe on, it is 18 µV. This means that the electronic noise, from the PD dark noise until the lock-in output, don't dominate. We could conclude that the system's noise shown in Figure 3.13 is mainly due to the probe power fluctuations and residual vibrations. Given the DC=6.5 V and the calibration factor for surface absorption R=11 W^{-1}, the corresponding noise for a pump power of 1 W (2 W before the chopper) is 0.25 ppm. In the case of bulk absorption, where R= 0.5 cmW^{-1}, the corresponding noise is 5 ppm/cm for silica

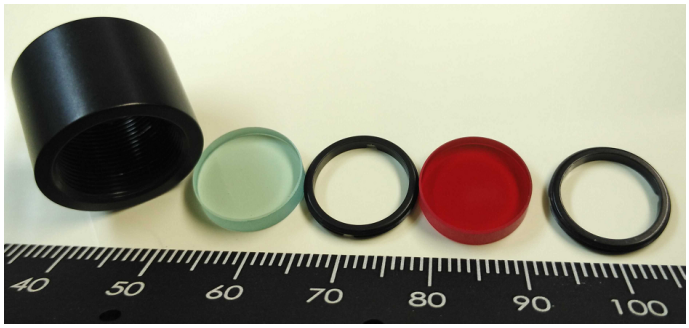

Figure 3.12: The two optical filters, together with the mount and the retaining rings used to fix them in front of the DET10A photo-detector. They are Heat Absorbing Glass, the first filter on the left is a 3 mm-thick KG-3 glass that filters out the 1064 nm light from the pump with an OD7 @1064 nm and 73% of transmission @633 nm; the one on the right is 2.5 mm-thick R-60 sharp cut red-color filter that blocks most of the daylight until 600 nm and has 90% of transmission @633 nm and @1064 nm. Together they allow only the 633 nm light to pass.

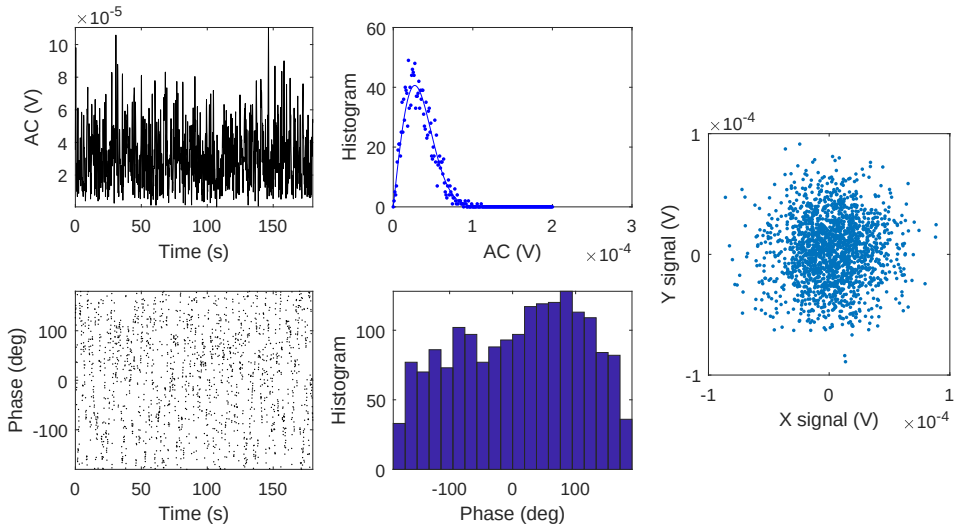

Figure 3.13: Different representations of the system's noise. On the left, the noise in the time domain of AC and phase, 180 s of acquisition time at 10 Hz of sampling rate. In the center, the histograms of the demodulated AC signal and its phase. The AC noise fits the Rayleigh distribution because it is the quadrature sum of two Gaussian distributed variables; the phase shows a uniform distribution. On the right, the same set of data plotted on the XY plane of the lock-in output signals. The signal is isotropic (phase uniform distribution), and centered in 0. The standard deviation of the noise is 18 µV. This data was taken with the probe laser ON and centered on the PD, the motors not moving, the chopper set at 430Hz, the lock-in time constant set at 100 ms.

and 15 ppm/cm for sapphire, which becomes about 1.5 ppm/cm when increasing the pump power up to 10 W.

Provided the noise not being in phase with the modulation (isotropic noise), it is possible to reduce the noise with digital filtering. There are 3 kinds of filters we are using. The *median filter* removes the spikes that are mainly due to dust particles crossing the probe. The *mean filter* (a moving average) reduces the standard deviation of the noise. In principle, the mean filter would have the same effect of increasing the lock-in time constant, but it is important to apply it after the median filter, otherwise, the spikes would spread in the filter buffer instead of being removed. Then there is the *phase filter* with is multiplying the AC signal by the cosine of the difference between the phase and the expected phase. This will remove the component of the signal orthogonal to the signal. If the setup doesn't have any noise drift, increasing the filters order (median and mean) there is no theoretical limit to reduce the noise, but we make a compromise with the acquisition time. For the lowest absorption rates, the acquisition time is about 10 s per point.

3.8 Numerical simulations

The main motivation for making numerical simulations is to understand what the expected signal is in an absorption system like ours, and to compare the calculated signal with measurements. It is also useful to calculate calibration correction factors between different materials. Moreover it's interesting to understand the differences between coating and bulk absorption.

This section is a report on how the PCI system is simulated, from the temperature distribution inside a test sample to the probe beam propagation, imaging, and detection. In the next section, we report the main results obtained with the simulation and the comparison with the scan measurement.

3.8.1 Temperature distribution

The first step is to get the temperature distribution inside a sample that is heated with a square wave modulated Gaussian beam. To calculate the solution to the heat equation, two kinds of approach are used:

- Semi-analytic solution calculated with MATLAB
- Finite Element Method software: COMSOL Multiphysics v5.1

Then, we compare the results from the two methods to confirm that the calculation is correct.

Semi-analytic solution The article "Photothermal deflection spectroscopy and detection" [31] presents a solution to the 3D heat propagation problem. The geometry has cylindrical symmetry, where the symmetry axis is the propagation direction of the pump beam, perpendicular to the surface of the sample. The sample is divided in 3 regions. The region 0 is the non absorbing air before the sample, the region 1 is the absorbing layer and the region 2 is non absorbing. In the case of surface absorption, the region 1 is the coating and the region 2 is the substrate; in the case of bulk absorption, region 1 is the absorbing substrate and region 2 is air again. The heat equation system is:

$$\nabla^2 T_0 - \frac{1}{k_0}\frac{\partial T_0}{\partial t} = 0 \qquad \text{region 0} \tag{3.20}$$

$$\nabla^2 T_1 - \frac{1}{k_1}\frac{\partial T_1}{\partial t} = \frac{-Q(\mathbf{r},t)}{\kappa_1} \qquad \text{region 1} \tag{3.21}$$

$$\nabla^2 T_2 - \frac{1}{k_2}\frac{\partial T_2}{\partial t} = 0 \qquad \text{region 2} \tag{3.22}$$

where κ_i is the conductivity, and $k_i = \frac{\kappa_i}{\rho_i C_i}$ is the diffusivity.$Q(\mathbf{r},t)$ is the heat deposited per unit volume oscillating at the chopper frequency ω in the absorbing medium and is given by

$$Q(\mathbf{r},t) = \frac{1}{2}\frac{4P\alpha}{\pi^2 a^2} e^{-\alpha z} e^{-\frac{2r^2}{a^2}} e^{i\omega t} + \text{c.c.} \tag{3.23}$$

where Q is a power per unit of volume, P is the laser total power, α is the absorption coefficient, a is the $1/e^2$ radius of the Gaussian beam, and the complex conjugate (c.c.) means that the real part is taken.

In order to clarify the coefficients of Eq. 3.23, let's calculate the integral of the Gaussian beam in dr:

$$\int_0^\infty 2\pi r e^{-\frac{2r^2}{a^2}} dr = \frac{\pi a^2}{2} \tag{3.24}$$

While the integral along the depth is:

$$\int_0^\infty e^{-\alpha z} dz = \frac{1}{\alpha} \tag{3.25}$$

Writing the total oscillating power as an integral in the total volume of Equation

3.23 we get:

$$\int_0^\infty \int_0^\infty Q(\mathbf{r},t)2\pi r dr dz = \frac{4}{\pi}\frac{P}{2} cos(\omega t) \tag{3.26}$$

which means that the term in Equation 3.23 is the first addend of the Fourier series for the square wave of amplitude $P/2$ and frequency $\omega/2\pi$, as shown in Figure 3.14.

$$Q_{TOT}(t) = \frac{P}{2}\frac{4}{\pi}\left(\cos(\omega t) - \frac{1}{3}\cos(3\omega t) + \frac{1}{5}\cos(5\omega t) + ...\right) \tag{3.27}$$

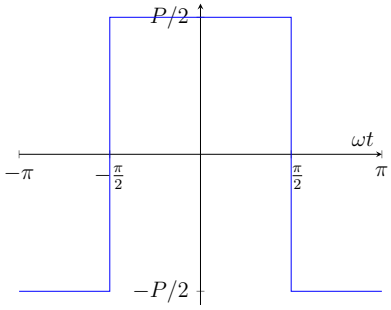

Figure 3.14: Pump intensity modulation: square wave

The analytic expression of the solution is shown in Figure 3.15. The integral has to be calculated numerically, so we made a MATLAB script. This is why we call the solution *semi-analytic*. Since the heat equations are linear, if the heat source is a square wave, the solution is calculated as a Fourier expansion where each term of the expansion is the solution for each harmonic of the heat source.

Using this solution it is possible to calculate the temperature distribution in any experimental condition by choosing the proper set of parameters. Figure 3.16(a) and 3.16(b) show an example of the calculated temperature distribution as a function of the radius r and the depth z.

$$T_0(\mathbf{r},t) = \frac{1}{2}\int_0^\infty \delta d\delta J_0(\delta r)E(\delta)\exp(\beta_0 z)\exp(i\omega t) + \text{c.c.}; \quad (4)$$

for region 2, we have

$$T_2(\mathbf{r},t) = \frac{1}{2}\int_0^\infty \delta d\delta J_0(\delta r)D(\delta)\exp[-\beta_2(z-l)]\exp(i\omega t) + \text{c.c.}; \quad (5)$$

and for region 1, we have

$$T_1(\mathbf{r},t) = \frac{1}{2}\int_0^\infty \delta d\delta J_0(\delta r)[\Gamma(\delta)\exp(-\alpha z) + A(\delta)\exp(-\beta_1 z) + B(\delta)\exp(\beta_1 z)]\exp(i\omega t) + \text{c.c.}, \quad (6)$$

where $T_i(r,z)$ is the component of the temperature difference oscillating at frequency ω,

$$\Gamma(\delta) = \frac{P\alpha}{\pi^2\kappa_1}\frac{\exp[-(\delta a)^2/8]}{\beta_1^2 - \alpha^2}, \quad (7)$$

$$\beta_i^2 = \delta^2 + i\omega/k_i. \quad (8)$$

Substituting into Eqs. (1) and satisfying the boundary conditions, we find that

$$\begin{aligned}
A(\delta) &= -[(1-g)(b-r)\exp(-\alpha l) + (g+r)(1+b) \times \exp(\beta_1 l)]\Gamma(\delta)/H(\delta),\\
B(\delta) &= -[(1+g)(b-r)\exp(-\alpha l) + (g+r)(1-b) \times \exp(-\beta_1 l)]\Gamma(\delta)/H(\delta), \quad (9)\\
D(\delta) &= \Gamma(\delta)\exp(-\alpha l) + A(\delta)\exp(-\beta_1 l) + B(\delta)\exp(\beta_1 l),\\
E(\delta) &= \Gamma(\delta) + A(\delta) + B(\delta),\\
H(\delta) &= [(1+g)(1+b)\exp(\beta_1 l) - (1-g)(1-b)\exp(-\beta_1 l)],
\end{aligned}$$

where

$$g = \kappa_0\beta_0/\kappa_1\beta_1, \qquad b = \kappa_2\beta_2/\kappa_1\beta_1, \qquad r = \alpha/\beta_1.$$

Figure 3.15: Analytic expression of the solution to the heat problem in the test sample from the article [31]. Equations (4),(5), and (6) are the integrals to calculate the temperatures outside the sample (T_0), inside the substrate (T_2), and inside the absorbing coating (T_1), at position (r, z), time t and modulation frequency ω. The integration variable δ has the unit of the inverse of a distance. δ enters the equations directly or through the variable β_i. α is the absorption coefficient, and l is the coating thickness. The variables g, b, and r in Equations (9) depend on the material properties: κ_i is the conductivity, $k_i = \kappa_i/\rho_i C_i$ is the diffusivity, ρ_i is the mass density, and C_i is the thermal capacity.

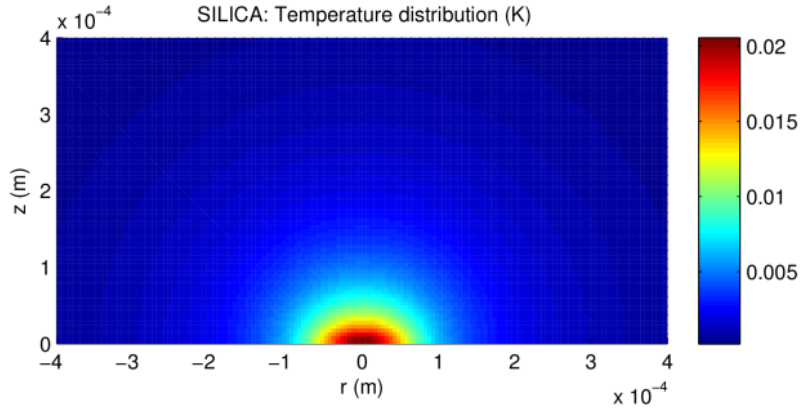

(a) Surface absorption

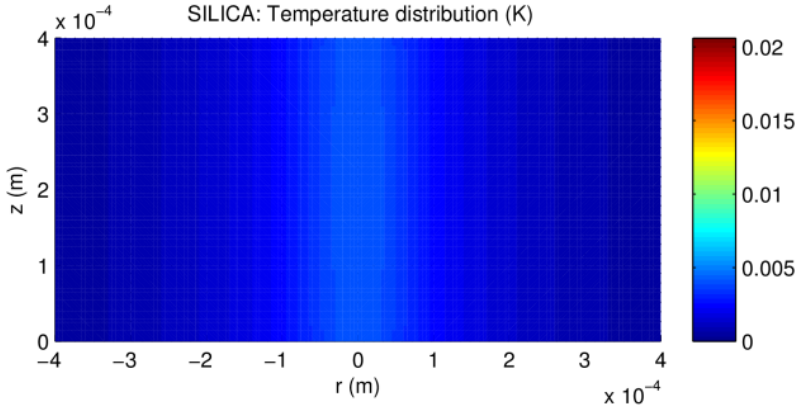

(b) Bulk absorption

Figure 3.16: Simulated temperature distribution in a fused silica sample that absorbs 12 ppm only on the surface (a), and in a fused silica sample that absorbs 12 ppm/cm in the substrate (b). The parameters used in this simulation are: the pump power, 1 W; the modulation, a sine wave at 1 Hz; the thickness of the surface absorbing layer, 10 µm. Note that, in the case of surface absorption, most of the temperature change happens inside the non-absorbing substrate. This is because the absorbing coating thickness is much smaller than the thermal length.

Given the pump power, the temperature distribution height and width, strongly depends on the thermal parameters of the material, especially on the diffusivity.

The plot in Figure 3.17 compares the temperature at the point $(r, z) = (0, 0)$ as a function of the modulation frequency, for three different materials, Silica, Sapphire and GaAs. We can see that the cut-off frequency change with the diffusivity. Table 3.2 summarizes the thermal properties of these materials.

Material	**Density** [kg/m^3]	**Conductivity** [W/(mK)]	**Capacity** [J/(kgK)]	**Diffusivity** [J/(kgK)]
Fused Silica	2200	1.38	740	8.47×10^{-7}
Sapphire	3980	24	761	7.92×10^{-6}
GaAs	5317	55	330	3.13×10^{-5}

Table 3.2: Thermal properties of the materials used for the substrates and coatings studied in this thesis.

COMSOL Multiphysics In order to double check the correctness of the solution, we calculate again the temperature distribution with another method: the software COMSOL Multiphysics v 5.1 with the Heat Transfer Module. The software solves the heat equation using the Finite Element Method (FEM). The geometry is 2D axisymmetric. The sample is a disk and there is a layer of 10 µm which represents the coating. The mesh of elements upon which the solution is calculated is finer near the center of the heat source and is coarser for larger r, see Figure 3.18(a). COMSOL requires to define the heat source. It has to be a Gaussian, according to the shape of the laser. The software allows to define the analytic form by taking one parameter: the standard deviation σ, and it defines the normal distribution:

$$\mathrm{gp1}(r) = \frac{e^{-\frac{r^2}{2\sigma^2}}}{\int_{-\infty}^{\infty} e^{-\frac{r^2}{2\sigma^2}} dr} = \frac{1}{\sigma\sqrt{2\pi}} e^{-\frac{r^2}{2\sigma^2}} \tag{3.28}$$

so, in order to have the same radius dependence as in Eq. 3.23, we have to set:

$$\sigma = \frac{a}{2} \tag{3.29}$$

In order to have the same amount of power on the sample, we have to find a constant A that multiplies $\mathrm{gp1}(r)$ and satisfies:

$$\frac{A}{\sigma\sqrt{2\pi}} = \frac{P\alpha l}{\pi a^2} \tag{3.30}$$

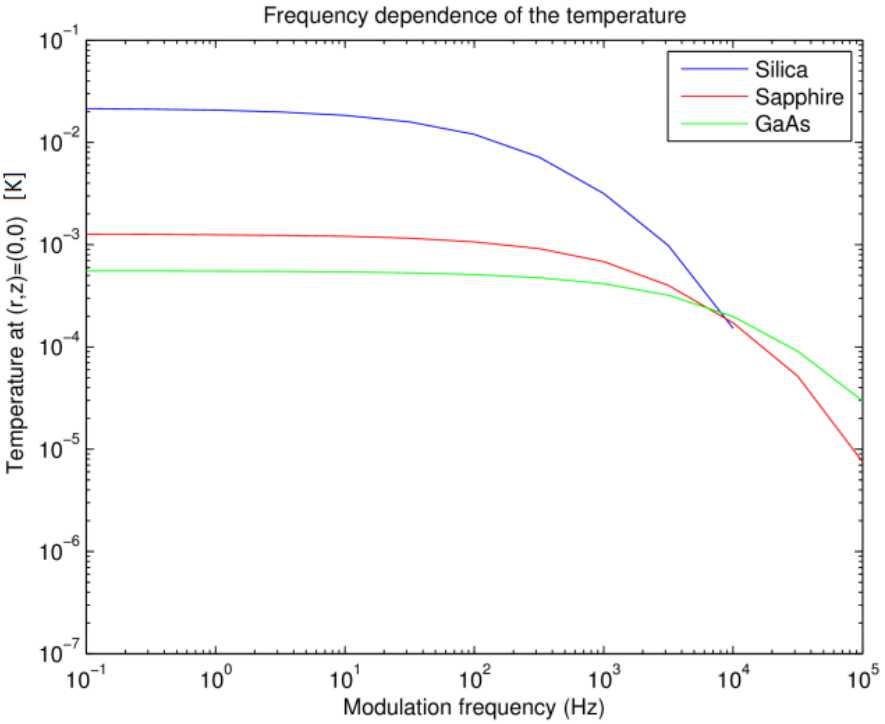

Figure 3.17: Frequency dependence of the temperature change at the center of the heated surface in the case of silica, sapphire and GaAs. The cut-off frequency in these spectra is related to the material thermal properties. The higher the diffusivity, the higher the frequency at which the temperature spectrum starts decreasing.

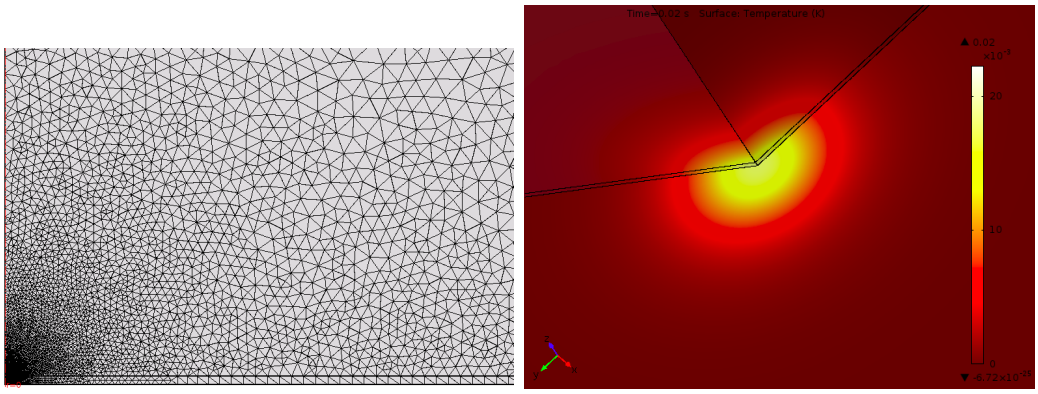

(a) Mesh (b) 3D representation of the solution

Figure 3.18: COMSOL Multiphysics: (a) the mesh grid of the geometry in cylindrical symmetry. There are more elements near the center of the heating source. (b) a 3D representation of the temperature distribution.

where the approximation $\int_0^l e^{-\alpha z} dz \sim l$ is used for $\alpha l \ll 1$. So, using relation 3.29 and solving for A :

$$A = \frac{P\alpha l}{\sqrt{2\pi a}} \tag{3.31}$$

So, the heat source to set in COMSOL is $\frac{P\alpha l}{\sqrt{2\pi a}}\,\mathrm{gp1}(r)$. The solution is time-dependent. The heat source time dependence can be set as a square wave. In Figure 3.18(b) there is an example of COMSOL result at a fixed time. A comparison of the two methods is shown in Figure 3.19, the plots show the temperature at the point $(r, z) = (0, 0)$ as a function of time. In the case of MATLAB semi-analytic solution, 50 harmonics are summed up to obtain the square wave solution. Since the two solutions have a good match, for the peak to peak value and for the rising time, we can conclude that the solution is correct. The choice is to use the MATLAB script

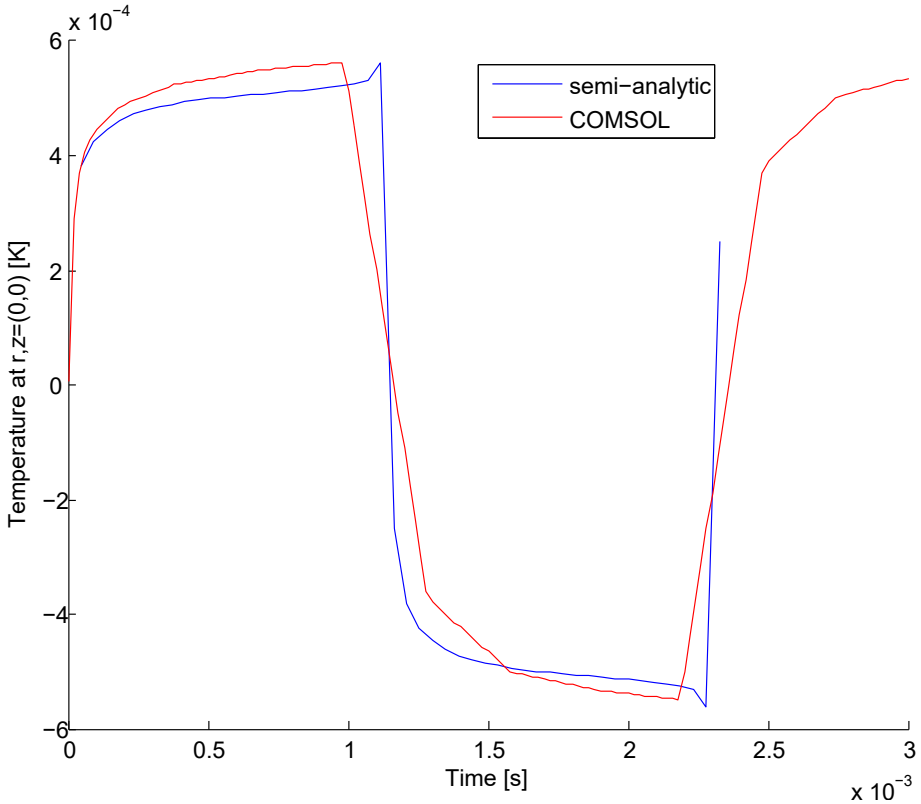

Figure 3.19: Comparison of the two simulations: good match for both the peak to peak value and the rising time.

to calculate the temperature distribution because it is a bit faster; in addition, the exportation of the result to the optical part of the simulation (written in MATLAB) is more direct.

3.8.2 Optical simulation

The final goal of the simulation is to calculate the photo-detector signal and compare the results with different sets of experimental parameters. The optical simulation consists of the propagation of the probe beam through the heated sample and through the optics of the Imaging Unit. I used the MATLAB package OSCAR V3 [32]. It is an FFT code that can define and propagate Gaussian beams. In Table 3.3 there is a list of the OSCAR commands used in the simulation.

G1 = Grid(Nb_points_grid, Size_grid)	Represents the discretization of the space where the electric field will be defined
E1 = E_field(Grid_name, options)	Defines the electric field of the Gaussian beam on the grid
E_plot(E1)	Displays a 2D plot of the field amplitude
[beam_radius, wavefront_RoC] = Fit_E_Field(E1)	Finds the beam parameter of the field E1
E2 = Propagate_E(E1, dist)	Propagates the field E1 over a distance dist in meter
E2 = Transmit_lens(E1, focal_length)	Transmits the field E1 through a lens of a given focal length

Table 3.3: OSCAR commands used for the optical simulation.

The crucial point of this simulation is the implementation of the thermal lens effect on the probe. To do this, we need the temperature distribution calculated previously and explained in Section 3.8.1. The refractive index distribution is calculated multiplying the temperature distribution by $\frac{dn}{dT}$, which is assumed to be a constant of the material. The refractive distribution is included in OSCAR as a 2D map of the optical path change. In general, when the laser beam crosses a medium of non-uniform refractive index $n(x, y, z)$, the optical path length along the optical axis can be defined as:

$$\mathrm{OPL}(x, y) = \int_0^L n(x, y, z) dz. \tag{3.32}$$

The probe passes through the sample with an incidence angle θ_{in}, which is about 6°, and inside the material it becomes

$$\theta = \arcsin\left(\sin\theta_{\mathrm{in}}/n\right) \tag{3.33}$$

according to the refraction laws. The optical path change is calculated from the temperature distribution as:

$$\Delta\mathrm{OPL}(x, y, \theta) = \frac{dn}{dT} \int_0^{\text{thickness}} T(x + z\tan\theta, y, z) \frac{dz}{\cos\theta} \tag{3.34}$$

The laser field E_0 passing trough an element that has a spatially dependent optical path $\Delta\mathrm{OPL}(x, y)$ gets an additional phase shift described by the Equation:

$$E_t(x, y) = E_0(x, y) e^{-jk\Delta\mathrm{OPL}(x,y)} \tag{3.35}$$

where E_t is the electric field right after passing the temperature distribution.

To make realistic simulations, I measured the waist of the probe and the distances among the parts of the original experimental setup. At the crossing point between pump and probe, the pump radius is 50 µm and the probe radius is 145 µm. The pump beam waist position along the z direction coincides with the crossing point position with an accuracy of ∼1 mm. The probe waist position along the z direction is 46.4 mm before the crossing point. The probe radius at the waist has a value of 87 µm. After the sample there is a mirror at 200 mm of distance; the converging lens ($f = 50$ mm) at 34 mm from the mirror; the reflective 5 mm-diameter sphere ($f = -1.25$ mm) at 65 mm from the lens; the detector at 75 mm from the small sphere; finally the photo-detector senses the intensity of the central part (0.8 mm^2) of the probe beam spot. The parts from the mirror to the detector are constrained to move together since they are on a micrometric translation stage (Imaging Unit) that can move along the direction of the pump beam axis. Figure 3.20 is a drawing of the probe optical path from the sample to the detector.

The optical simulation reproduces all the passages of the probe through the optical components of the system, from the definition of the probe beam before the sample, up to the detector. A pseudo code of the simulation follows:

- Create a grid
- Define the electrical field with waist 87 µm
- Propagate 46.4mm
- Add the phase of the thermal lens effect (Equation 3.35)
- Propagate 234 mm (crossing point-mirror distance + mirror-lens distance)
- Pass through lens with f=50 mm

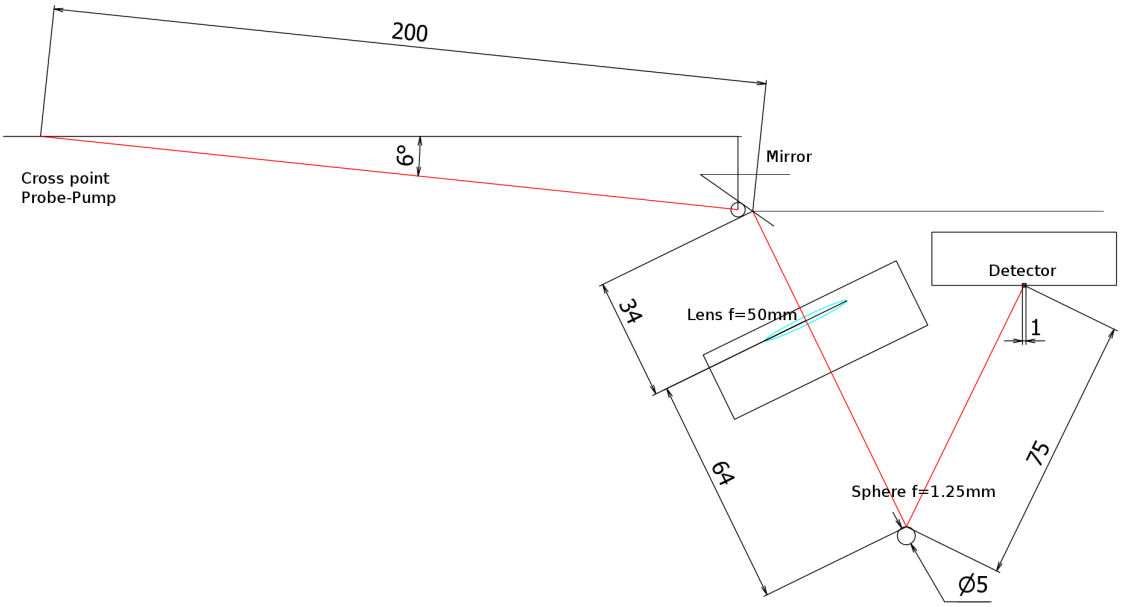

Figure 3.20: Drawing of the optical probe path from the crossing point to the detector. Distances are in mm.

- Propagate 65 mm
- Pass through a lens with f=-1.25 mm
- Propagate 75 mm
- Take the square modulus of the electric field, $|E|^2$.
- Integrate $|E|^2$ on the central area, 0.8 mm^2, which is the size of the detector.

The result is proportional to the output signal of the detector.

In the experimental setup, the lock-in amplifier demodulates the PD output and returns an AC amplitude which is proportional to the absorption, and a phase, which is related to the delay of the temperature oscillation with respect to the chopper. In order to reproduce this demodulation process in the simulation, we could calculate the oscillating temperature distribution at many times in one period, then propagate the probe for each of these times and calculate the oscillation of the PD signal. Instead, a much more efficient way, in terms of computational time, is to consider the oscillating temperature as a complex number, separately propagate the probe through the real part and through the imaginary part of the temperature distribution, and then recombine real part and the imaginary part of the PD output to get the module (AC) and the phase of the signal.

3.8.3 Sample scan

To test the simulation results, we reproduce a typical signal and compare it with a measurement. The typical measurement is a scan along the z-axis, which is the direction of the sample depth. In the lab reference frame, during a scan, the pump and the probe beam positions are fixed, while the sample is translated along the z-axis. In the simulation, we choose to stay in the reference frame of the sample. In this frame, the pump beam doesn't move because it has an almost perpendicular incidence on the surface. The probe beam shifts along the surface by an amount which is the tangent of the incidence angle (6°) times the translation of the sample along the z-axis in the lab frame. The shift of the probe during the scan is made by shifting the $\Delta\mathrm{OPL}(x, y)$ map along x.

When plotting the scan of AC and phase vs the sample displacement, the refraction inside the material is considered by scaling the z coordinate according to Equation 3.19.

3.9 Simulation results and applications

In this section, we show the most significant results achieved by using the simulations.

3.9.1 Comparison with the measurements

We simulated the scan of the two reference samples presented in Section 3.4. Figure 3.21 shows the experimental scan of the surface reference sample and bulk reference sample and the comparison with the simulation.

Regarding the shape of the scan, both the simulations are in very good agreement with the measurement. The surface sample scan peak value is within the experimental error, but the bulk simulation is about 3 times smaller than the measurement. This shows that there are some limitations to this simulation approach. The calculation from [31] is a model designed for coatings absorption where the absorbing layer is much thinner than the Rayleigh distance of the pump, so the pump size is constant. To adapt this model to the bulk absorption, we increased the thickness of the absorbing layer to the whole substrate thickness, while the non-absorbing substrate is replaced with the air surrounding the sample. In this way, the simulation doesn't take into account of the variation of the pump size while crossing the substrate. The Rayleigh length of the pump is 3.8 mm and the sample thickness

is 3.6 mm. Another important approximation is the material of the bulk reference sample. For the Schott glass which is based on fused silica, the thermal properties are a bit different from the pure fused silica, but we couldn't find the parameters values in the literature. Also, other physical effects are not taken into account. For example, the fact that the dn/dT value might change when the material is under mechanical stress such as the periodical thermal expansion due to the modulation of the heating.

However, the simulation purpose is not to quantify the absorption signal, but to have a qualitative understanding of what is going on in the setup.

3.9.2 Parameters variations

Sometimes, changing the experimental parameters may be difficult, time-consuming or expensive. Running simulations allows having an idea of what would happen if a parameter was different. Also, it is useful for a better understanding of the optimization procedures and maximization of the system responsivity.

The imaging unit position optimization is done experimentally by moving the lenses on the imaging unit and finding the sharp image of a blade, as explained before in this Chapter. We simulated the optimization process by changing the distance of the lenses on the imaging unit. The simulation result plotted in Figure 3.22 shows that for a larger pump size the responsivity is lower and that the optimal position of the imaging unit is different. So, when changing the pump size, the alignment and optimization must be repeated.

We simulated the absorption signal if the bulk reference sample was thicker, 8 mm instead of 3.6 mm, but with the same absorption rate: 116%/cm. The simulation result is shown in Figure 3.23. In the case of a thicker sample, we can clearly see the effect of the depletion of the pump inside the substrate, which is the reason why the second interference peak at the boundary of the sample is smaller than the first one, even with the real thickness 3.6 mm.

As we change sample material, a difference in the thermal parameters produce a difference in the thermal distribution, and so in the responsivity. We simulated the signal of a low absorbing sapphire sample, and the signal of a sample with the same absorption and thickness, but made of fused silica which has a lower diffusivity. The result is shown in Figure 3.24. Higher diffusivity gives lower responsivity. According to the simulation, with the same absorption rate, the ratio between the silica sample signal and the sapphire sample signal is about 3.5. This number is consistent with

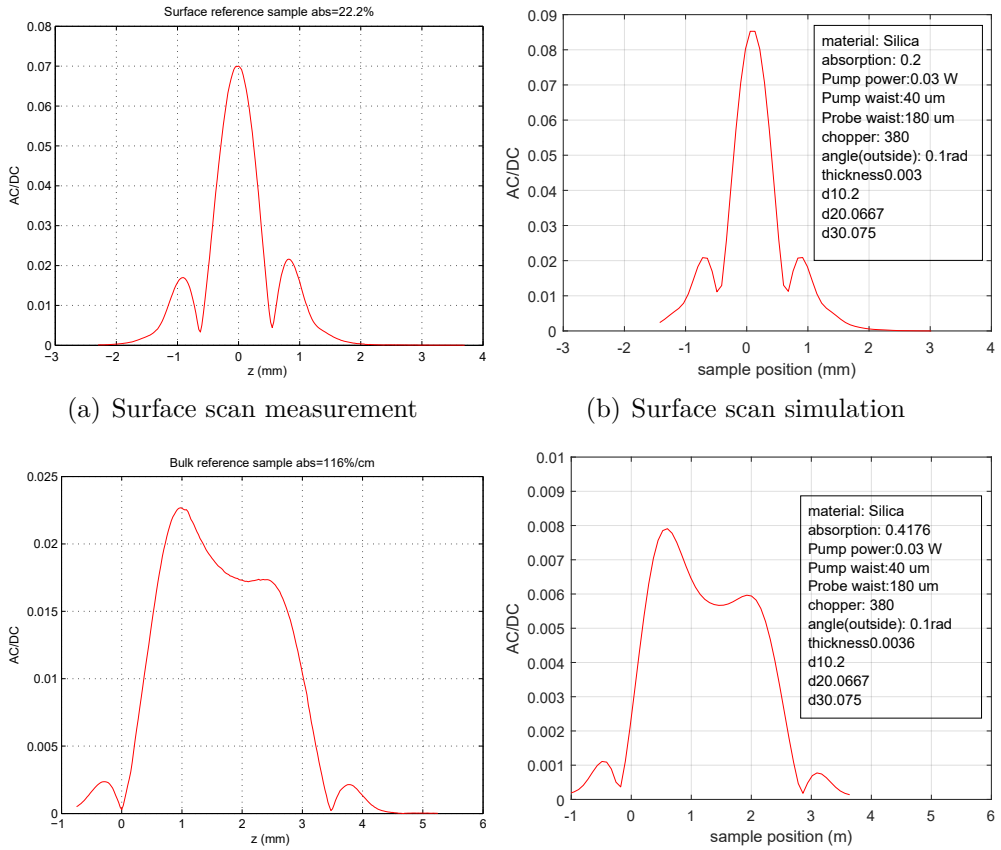

(a) Surface scan measurement

(b) Surface scan simulation

(c) Bulk scan measurement

(d) Bulk scan simulation

	Surface	Bulk
Measurement	0.068	0.0175
Simulation	0.086	0.0057

Figure 3.21: Reference samples measurements and simulations. On the top, the surface reference sample. On the bottom, the bulk reference sample. The experimental error is 20% for the absolute value. In the thermal part of the simulation, the power parameter is set as the power of the measurement, P=30 mW, and the absorption rate is set as the nominal absorption rate of each sample. For the bulk reference sample, the absorbing layer thickness parameter is set at 3.6 mm, which is the total thickness of the sample; for the surface reference sample, the layer thickness parameter is set at 10 µm, which is the order of magnitude of the thickness of the typical coatings. In order to normalize the signal to the probe power, the plots show the AC signal divided by the DC value. The table shows the AC/DC values at the center of the scan.

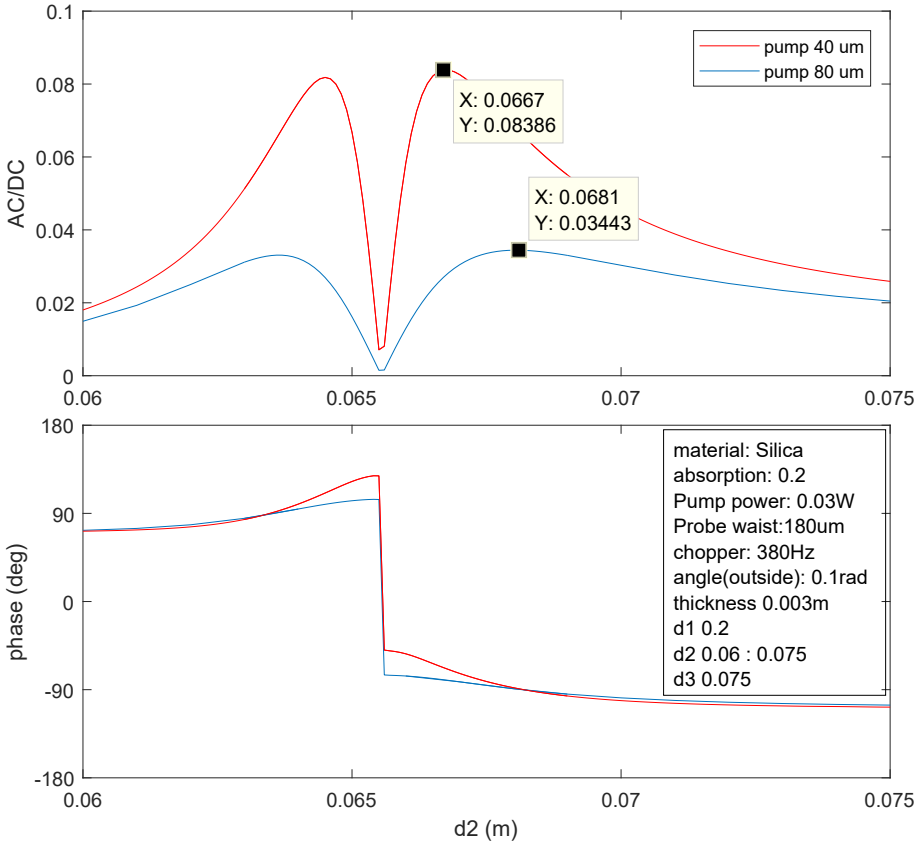

Figure 3.22: Simulation of AC signal and phase of the surface reference sample as a function of the distance between the focusing lens and the reflective sphere on the imaging unit. In red the case when the pump size (radius) is smaller, in blue the case when the pump size is larger.

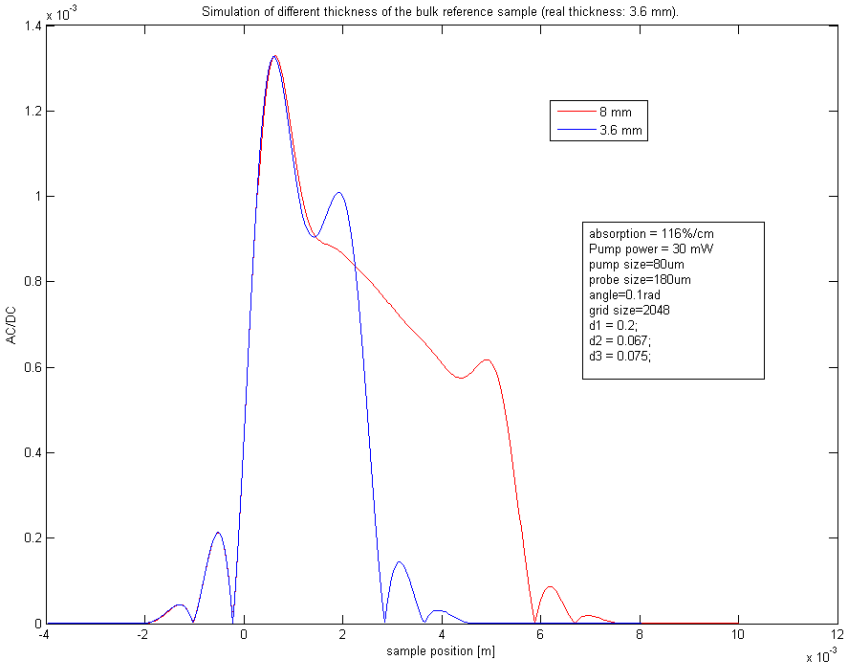

Figure 3.23: Blue curve: simulation of the scan of the 3.6 mm-thick bulk reference sample. Red curve: sample with the same properties but larger thickness: 8 mm.

the 3.34 correction factor found experimentally by the company SPTS that provided the absorption measurement system.

3.9.3 Prediction of calibration factor for thin GaAs samples

In the PCI absorption measurement system, surface absorption and bulk absorption have different calibration values. GaAs/AlGaAs dielectric coatings are grown on GaAs substrates and then they are transferred on optical substrates, such as silica or sapphire. Since the coating is very thin (few microns) the calibration of surface absorption depends on the thermal diffusivity of the material of the substrate (Table 3.2). The wafers where the coatings are grown are thin disks between 0.4 mm and 0.5 mm of thickness. Usually, the calibration procedure is made by using a spectrophotometer that measures the transmission T and the reflection R of the sample, and then the absorption is calculated as the difference Abs$= 1 - R - T$. The precision of this procedure is about 1% of absorption. So, the calibration of coatings that absorb only a few ppm is not possible with a spectrophotometer. Having high absorbing substrates would help as long as there is a way, the simulations, to convert

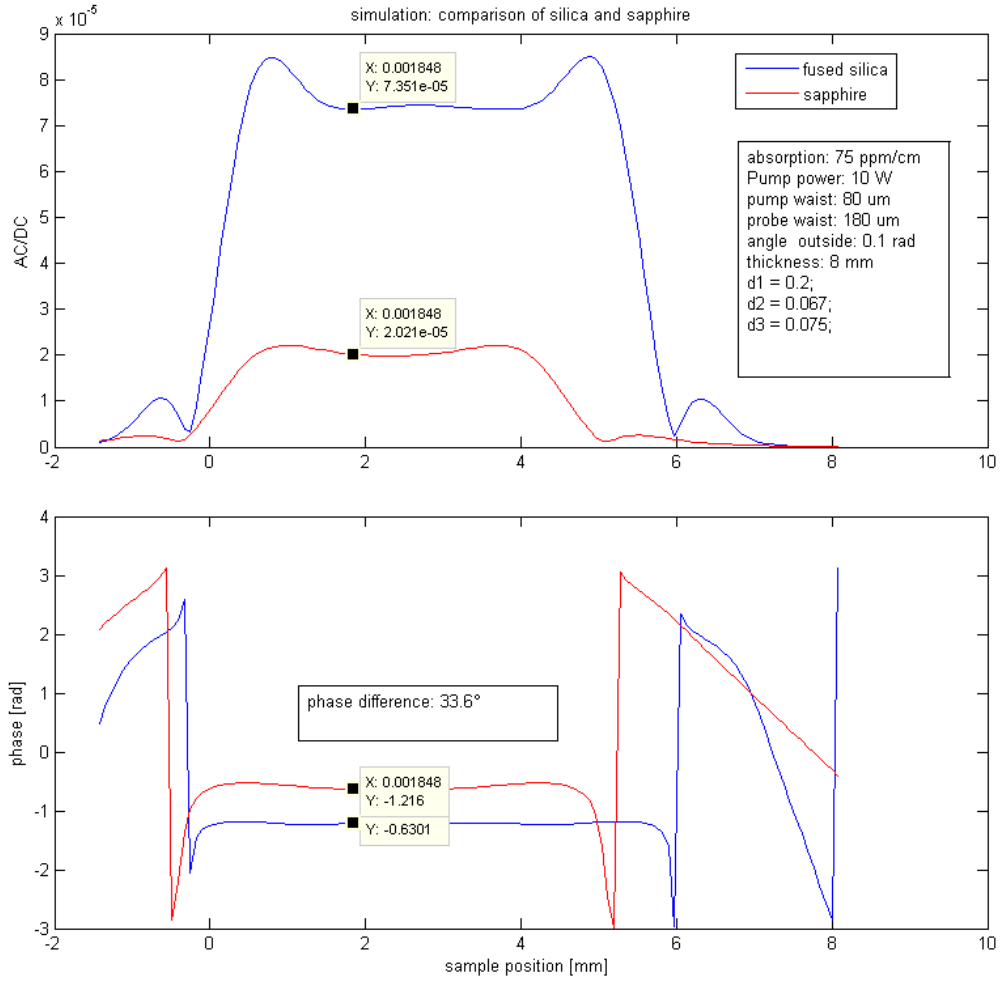

Figure 3.24: Simulation: comparison of fused silica (blue) and sapphire (red). Sapphire, with higher diffusivity, gives a lower signal than fused silica. The phase is different in the two material because of the different delay in the temperature change with respect to the chopper modulation. Also, the apparent thickness is smaller because the refractive index is higher. In the case of low absorption, the pump depletion in the substrate is negligible, so the two interference peaks at the sample boundaries are equal.

bulk calibration to surface calibration. In other words, the simulation can calculate how the detector signal changes if the absorption happens on the entire bulk or if it's concentrated only on the surface. In the case of surface absorption, the bulk absorption rate is not considered because the pump beam is not transmitted after the high-reflection coating. Figure 3.25(a) shows the temperature distribution on a GaAs 0.4 mm thick sample with 5% absorption rate distributed on the entire thickness. Figure 3.25(b) shows the temperature distribution on a GaAs 0.4 mm thick sample with 5% absorption rate concentrated on the first 10 µm. The temperature distributions are very different, but the simulated scans of the two cases are equal, Figures 3.25(d) and 3.25(c). This is a surprising result because it says that the calibration factor is the same, which was not obvious at all a priori. The reason for this result is basically the thickness of the substrates: 0.4 mm is smaller than the pump-probe interaction area (ellipsoid), which is about 2 mm long. The system is not able to distinguish spatial resolution smaller than the pump-probe crossing area. This calculation allows us to measure the optical absorption on substrates and coatings of 0.4 mm-tick samples with the same calibration factor.

3.10 Conclusions

In this chapter, we described the PCI system and presented some crucial issues for a correct calibration of the absorption measurements. The simulation results were useful to deeply understand the principles and many features of the experimental setup. In next chapter, we describe the details on how we upgraded the setup in order to measure KAGRA sapphire substrates and crystalline coatings. During the upgrade work, the awareness developed doing the simulations was very helpful.

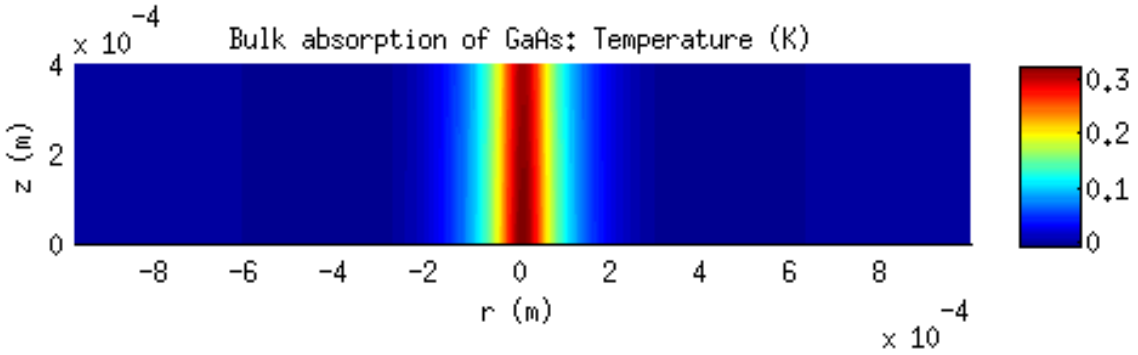

(a) Thermal simulation of bulk absorption

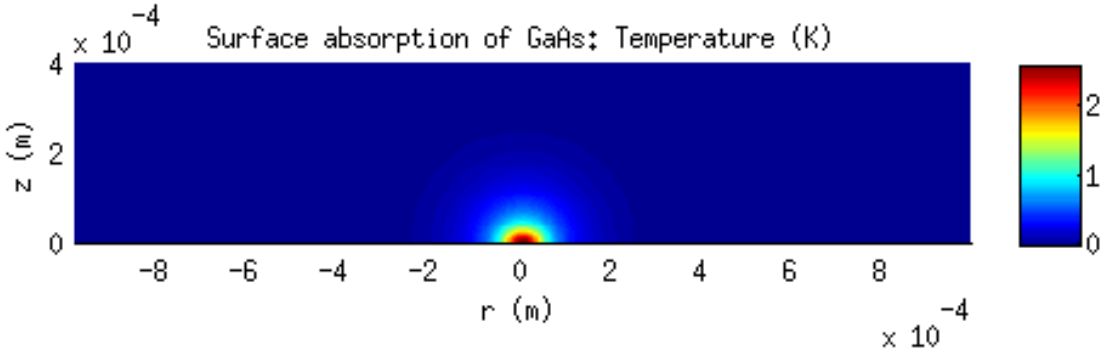

(b) Thermal simulation of surface absorption

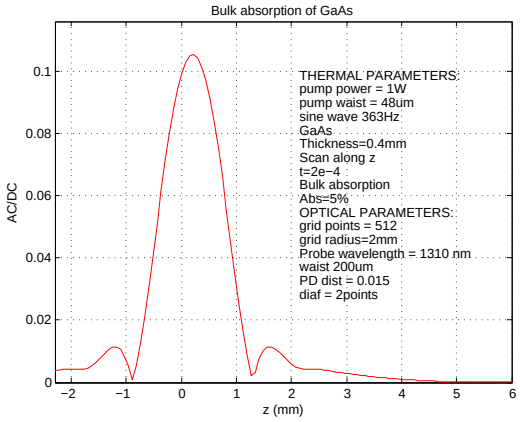

(c) Bulk scan simulation

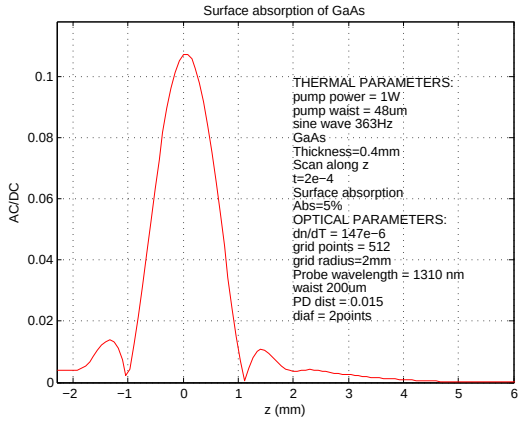

(d) Surface scan simulation

Figure 3.25: Simulation: comparison of surface and bulk absorption of a 0.4 mm-thick GaAs substrate.

Chapter 4

Experimental setup upgrade

The absorption measurements of KAGRA sapphire substrates and of the new large-area AlGaAs crystalline coatings are the main goal of this thesis work. In the original PCI setup, the translation stage was too small to bear the KAGRA test masses. Besides, GaAs materials are not transparent to the 633 nm probe. During this Ph.D., we worked on upgrading the experimental setup in order to overcome these issues. In this chapter, I report the details on the upgrade development, the main problems we encountered and the solutions we adopted.

4.1 Large translation stage

The large translation stage is made by the company Zaber Technologies Inc. It uses step motors to move the samples back and forth with a precision of 8063 steps/mm along the three directions X, Y, and Z. The Z-axis is horizontal and along the laser propagation direction, the Y-axis is horizontal and transverse to the laser propagation direction, and the X-axis is vertical. A pair of linear LST0250A-E01T3 250 mm stages are synchronized to move together along the Z direction, and a pair of linear LST0500A-E01T3 500 mm stages are synchronized to move together along the X direction. The two pairs are controlled by two X-MCB2 controllers. To move along Y there is a single linear LST0300A-E01T3 300 mm stage controlled by an X-MCB1 controller. The three controllers are connected together and communicate with the computer through a USB port. The settings of the stages (speed, acceleration, position limits, lockstep etc.) are controlled through the Zaber Console software [33]. The motion of the stages is controlled and monitored sending string commands via the serial port. Using LabVIEW VIs, it is possible to send commands to move the translation stage. The new setup is able to measure samples of several sizes, from

1 inch in diameter, to 22 cm in diameter and 15 cm in thickness, which corresponds to the KAGRA mirrors size. For different sample sizes, 3 interchangeable mounts are placed on the translation stage. The translation stage is shown in Figure 4.1, and the mounts are described in Figure 4.2.

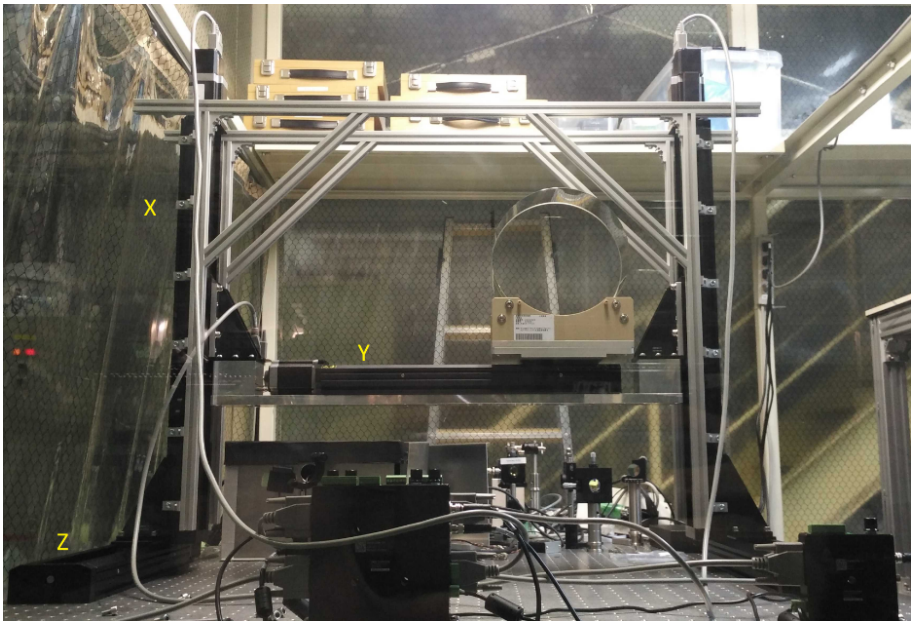

Figure 4.1: Preliminary assembly of the translation stage in its final configuration. To improve the rigidity of the structure, we assembled a cage made of aluminum extruded beams that connects (like a bridge) the two X-axis linear stages. The mount increases the height of the sample. So, we added 2 aluminum spacers and a long shelf to lower the vertical position of the Y linear stage.

4.2 Setup design

Since the AlGaAs crystalline coatings that we want to measure are not transparent to visible light, beside the existent HeNe probe laser (633 nm), we added a second probe with a wavelength of 1310 nm. In order to be able to switch between samples of different materials, the two probes are aligned to meet the pump in the same crossing point at the same angle $\theta = 0.1$ rad, one from the left and the other from the right side of the pump beam. The design of the upgraded setup is shown in Figure 4.3. The advantage of this optical configuration is that to change probe laser it is sufficient to turn off one and turn on the other, with only a little alignment optimization.

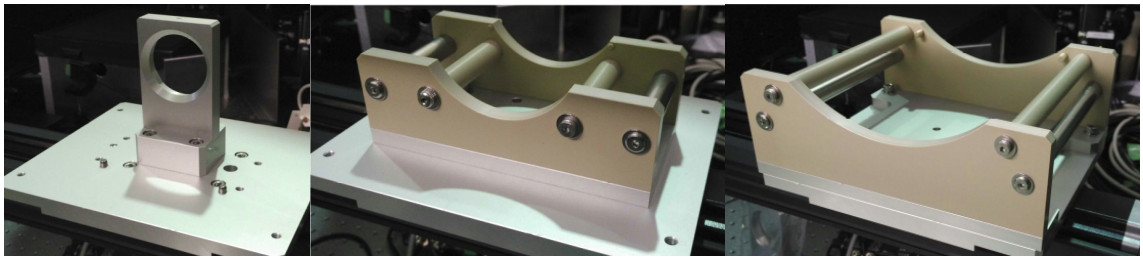

Figure 4.2: From left to right: a small mount for samples up to 2 inches in diameter, a mount for Tama300 mirror size samples (100 mm-diameter × 60 mm), and a mount for KAGRA test masses size sample (220 mm-diameter × 150 mm).

Each probe needs a different photo-detector. For the HeNe, we use a silicon detector (Thorlabs DET10A), and for the infrared, an InGaAs detector (Thorlabs DET10N). We put them on two separated imaging units. Because of the size of the large translation stage, the optical breadboard used in the original setup (see Figure 3.2) has not enough room, so the setup had to be divided into two parts: the lasers input optics on an optical breadboard before the sample; and the imaging units and the power meter on a separate optical breadboard after the sample. The distance between these two breadboards is determined by the translation along the Z-axis which is required to complete a scan of the largest sapphire sample. This amount is 83 mm, according to formula 3.19 plus the sample thickness 150 mm, plus the sample mount thickness 1 cm per side. Since the optical components are on optical boards at different heights, having a 3D drawing of the experimental setup was very helpful when optimizing the distances between the parts on the optical table.

4.3 Laser beams profile

To be able to make a complete scan of the large samples, the pump-probe crossing point must be outside the sample when the sample is at the ends of the translation range. The refraction effect of Figure 3.6, combined with the thickness of the sample, and the requirement that the beams' waist should be at the crossing-point, set a constraint on the choice of the lenses used to focus the pump and the probes. The pump beam waist should be 35 µm. To set the waist at the crossing point position, we had to replace the lens of the original setup with two lenses. A first f=50 mm lens is used to make the beam larger on the second lens, which is a f=100 mm lens placed at 222 mm from the first lens and at 243 mm from the crossing point. The focal length and position of the lenses for the probes were chosen to satisfy

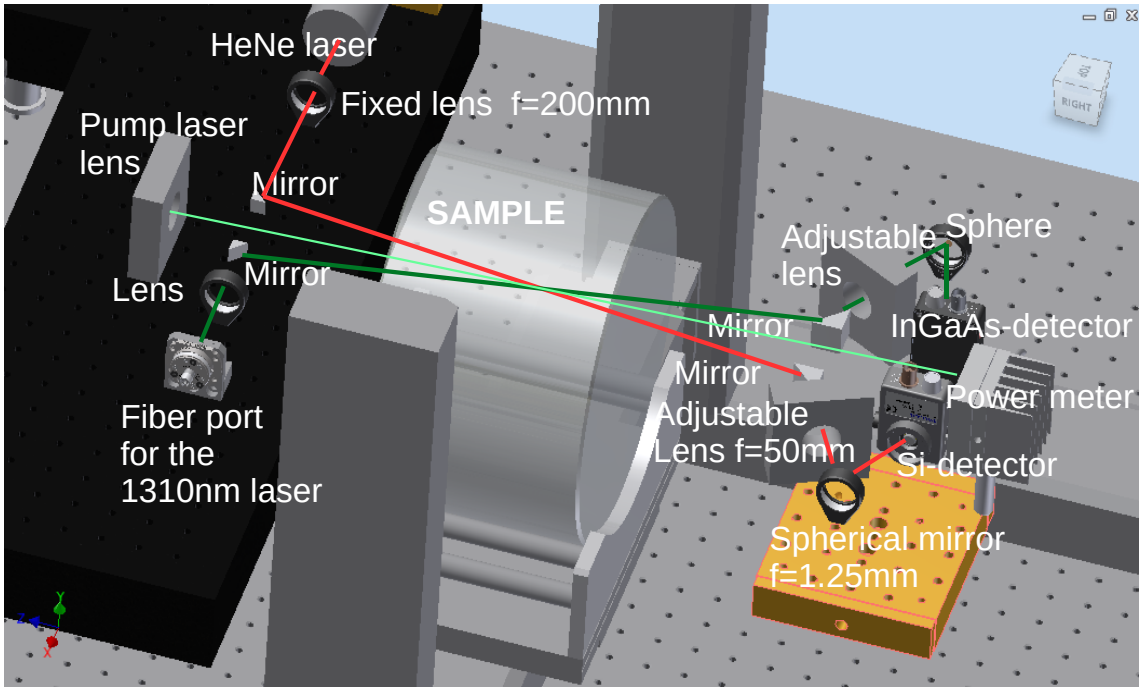

Figure 4.3: Preliminary design of the upgraded setup. The red line is the 633 nm probe beam, the light green line is the pump, and the dark green line is the 1310 nm probe. This 3D drawing is done with the 3D-cad software Inventor Professional 2015, assembling the 3D models of the optomechanical parts.

the requirement that the probes waist should be at least 3 times larger than the pump waist. For the HeNe probe, the lenses are a f=50 mm lens and a f=75 mm lens at about 47 mm from each other. They are placed at only 20 mm from the HeNe aperture. For the 1310 nm probe, there is a f=300 mm lens at about 300 mm from the crossing point. In Figure 4.6 there is a picture of the optical board where the input optics are placed. After setting the lenses and aligning the three beams we measured the beams profiles using a blade moved with the translation stage. The result of the measurement is shown in Figure 4.4. The HeNe beam is 3 times the pump waist while the 1310 nm waist is 5 times larger. According to the SPTS company, the larger the probe, the better, but we wanted to keep the HeNe size the same as in the original setup, so that the calibration on sapphire will not be affected.

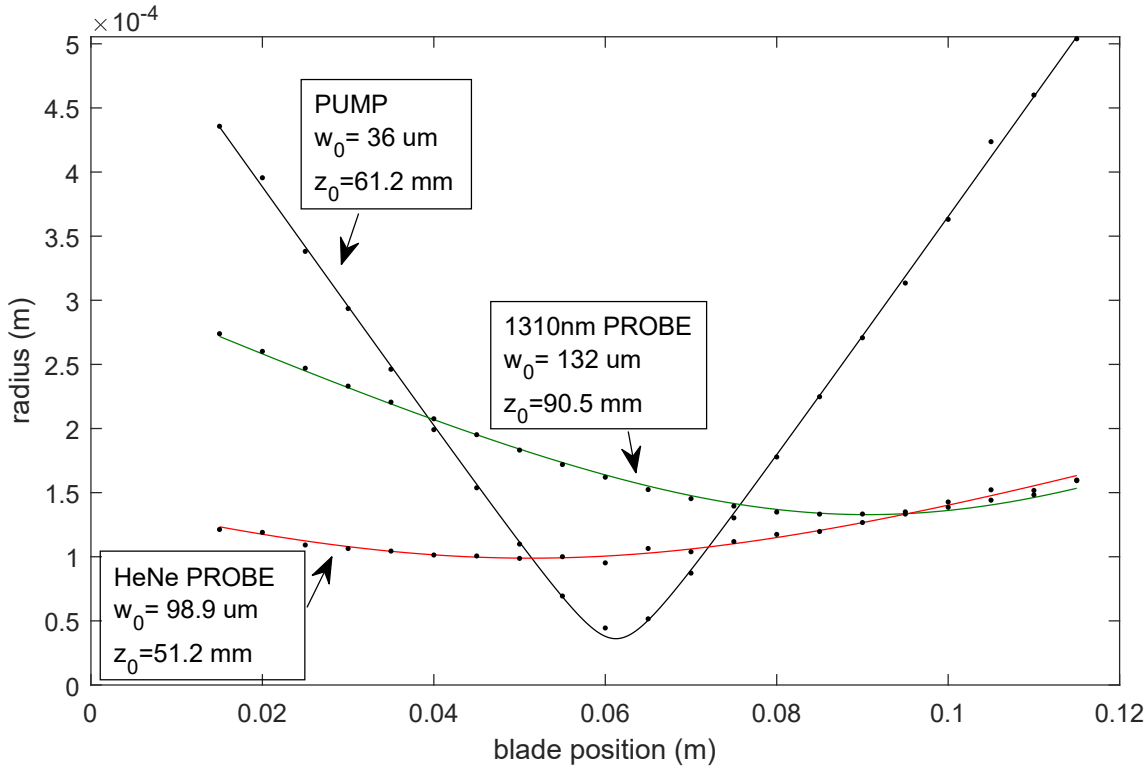

Figure 4.4: Beam profile of the pump and of the two probes. Using a LabVIEW vi, we control the blade that is fixed on the translation stage, and we measure the transmitted power. The blade cuts the beams at different positions and the scan of the blade is fitted with an erf function. Each point in this plot is the result of the fit. Then the beam profiles are fitted and the waists size and waists position are displayed on the plot. The zero of the blade position coordinate is at 172 mm from the mount of the last pump lens. The black line is the pump: the red line is the HeNe probe; and the green line is the 1310 nm probe.

4.4 Pump reflections

Initially, we set the pump perpendicular to the sample and the probe beams at 0.1 rad to the pump, one on the left and one on the right. Then we found a problem, the Fabry-Pérot effect, which is the interference of the pump reflections inside the substrate. This effect is strong if the sample is at a small angle to the beam and the coherence length of the pump is about or longer than the thickness of the sample. In Figure 4.5, there is an example of the fringes found on the surface reference sample, the absorption signal periodically fluctuates by a factor of 2, and there are about 5 fringes/cm. We tried with another sample (same model) and found 25 fringes/cm, which shows that the number of fringes/cm depends on the wedge of the sample.

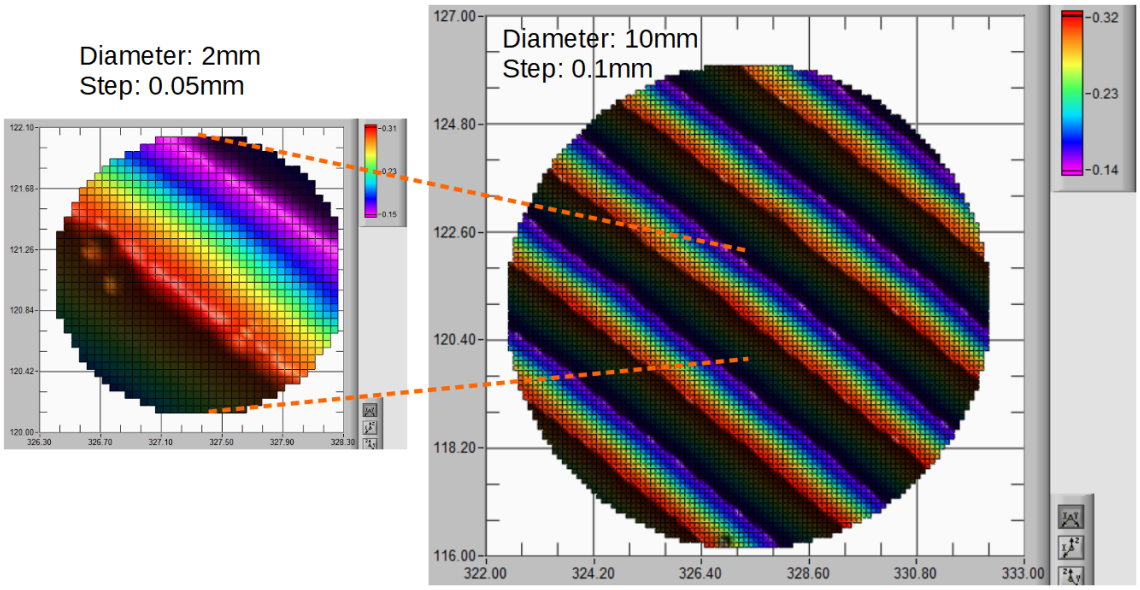

Figure 4.5: Fabry-Pérot effect of the pump perpendicular to the surface. This is a map of the absorption signal on the surface reference sample (Newport FRQ-ND02). The fluctuation is about a factor of 2, and there are 5 fringes/cm, for the wedge of the substrate. Tilting the pump by 2 deg solves this problem reducing the fluctuations below 5% of the signal.

The solution to this problem is to tilt the pump beam by 2 deg or 0.035 rad with respect to the sample surface normal. Doing so, we also had to tilt the probe beams to keep the angle pump-probe at 0.1 rad. Therefore the incidence angle for the HeNe probe on the sample is 0.065 rad and the one for the 1310 nm is 0.135 rad. To do the alignment of the three beams, we put a 200 µm pinhole on the translation stage, moved it along the desired beam path from a LabVIEW software (presented in the next section) with a micrometric precision, and maximizing the transmission

through the pinhole. First, we aligned the beams without lenses using the mirrors, and after placing the lenses then we aligned again by moving the lenses so that the beam is well centered, to minimize aberrations. At the end of this procedure, all the beams pass through the pinhole with a very precise angle and, as seen in Figure 4.4, with the waist near the crossing point.

When measuring high-reflectivity coatings, all the power is reflected back. Since the pump has 2 deg of incidence, an uncontrolled high power reflection might heat up some opto-mechanical part and generate scattering or thermal fluctuations which will affect the absorption signal. We sent the pump reflection to a beam dump by installing a simple mirror between the last focusing lens for the pump and the prism mirror for the HeNe probe. The beam dump transforms the laser power into heat, so, to avoid thermal disturbances, we placed the beam dump outside the optical board. See Figure 4.6 to visualize the setup configuration on the optical board before the sample.

4.5 Demodulation and measurement control

The signal from the photo-detector is sent to the lock-in amplifier SR830 through a BNC cable, the DC component of the signal is separated with a passive RC circuit and sent in the auxiliary input, while the AC component is sent in the front input. The lock-in amplifier demodulates the AC signal mixing it with the reference signal from the chopper and returns the X and Y values, which are the demodulation with the cosine and with the sine at the chopper frequency. Putting X and Y as components of a vector, we calculate the modulus R (in this setup it is called AC signal) and the phase. The integration time is set to 100 ms so the sampling rate is 10 Hz.

With the original setup, the company SPTS provided a LabVIEW based software that controls the system. Unfortunately, after upgrading to a larger translation stage, the software was not compatible. Also, we couldn't edit the source code, so we made a new LabVIEW Virtual Instrument (VI) from scratch, and we added some functions that were not available with the original software. The VIs control the translation stage through the USB serial port, and the lock-in via a GPIB-to-USB adapter. We made two main VIs: one that makes 1D scans of the samples along any of the three directions, and one that makes 2D maps on any of the three planes XY, YZ, XZ. The VIs move the sample, wait some time, read the lock-in output, make the plots and save the data. We implemented two kinds of digital filters in order to

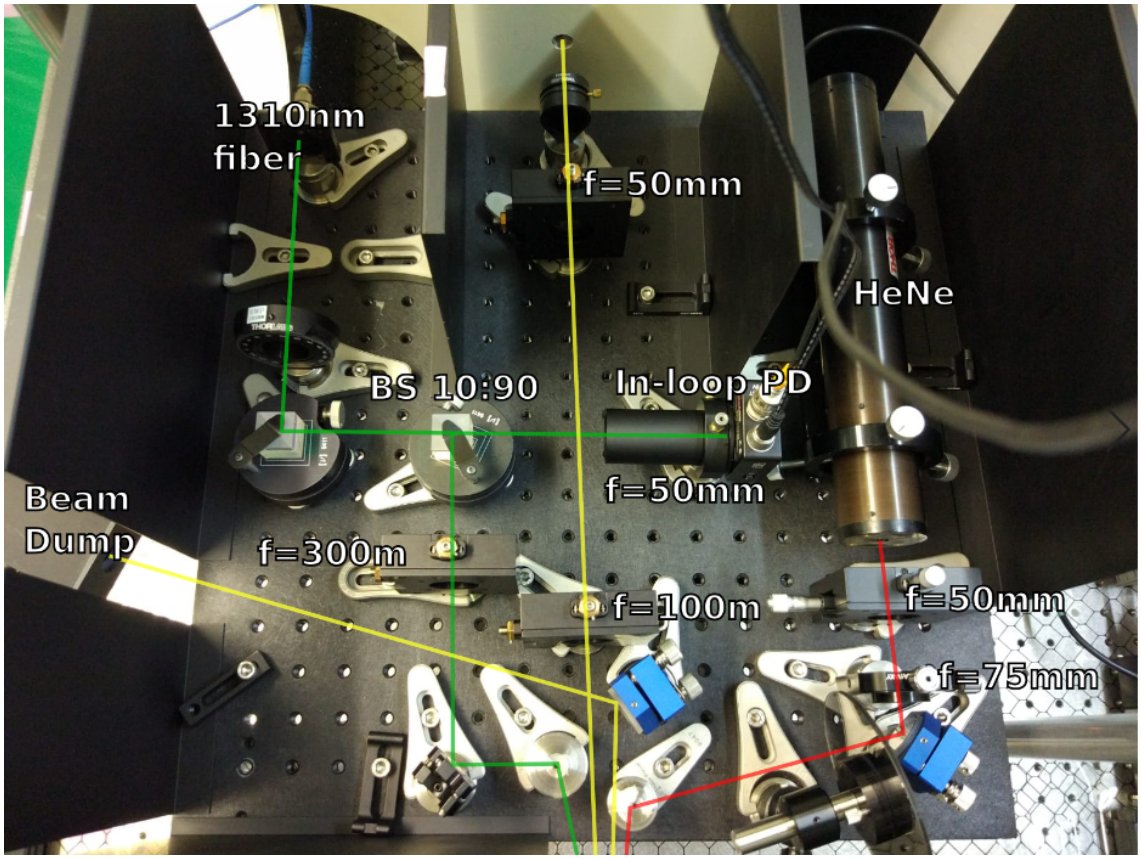

Figure 4.6: Picture of the optical board before the sample. The yellow line is the optical path of the pump that is focused with two lenses, f=50 mm and f=100 mm. The pump reflection is sent on the beam dump outside the optical board. The red line is the optical path of the 633 nm probe which is focused with two lenses, f=50 mm and f=75 mm. The green line is the optical path of the 1310 nm probe which is splitted in two parts: 90% is focused on the sample with a f=300 mm lens, while 10% is focused with a f=50 mm lens (inside the lens tube) on the in-loop photodiode, which is used to control the intensity fluctuation. Inside the lens tube, there are also two long-pass filters: a FEL1250 and a FELH1250, for a total optical density OD=11 at 1064 nm, to prevent the pump stray light to go in the control loop. More details on the control loop are in Section 4.7.

reduce the noise: a median filter that gets rid of the spikes (usually due to the dust crossing the probe), and an average filer. The scan VI it allows to set the initial position of the sample, the scan axis, distance and step, the waiting time, the filters order and the saving file name. The map VI allows to set the map plane, size and resolution. As a new feature with respect to the original, it allows to select between rectangular and circular map, and choose the center and the radius of the map. The map absorption measurement result (AC signal) is displayed on a 3D surface plot. Both the VIs (scan and map) also show the real-time signals in a chart with and without filtering. Figures 4.7 and 4.8 show the front panel of the VIs we developed and used for our measurements.

4.6 Alignment and calibration

As explained in the previous sections, all the beams pass through the same crossing point. Then the pump goes on the power meter and the probes go on their respective imaging units. The one for the 1310 nm probe sits on a linear stage with a micrometric screw with a range of 40 mm, while the one for the 633 nm probe sits on a linear stage with a micrometric screw with a larger range, 80 mm, because it is used to measure large sapphire substrates. The alignment procedure to maximize the responsivity has been described in detail Chapter 3. We maximized the DC signal by centering the beam on the PD, we maximized the AC signal by tuning the position of the pump, and we maximized the AC/DC signal by moving the the imaging unit linear stage. The two imaging units have the same configuration but on the 1310 nm probe one, the beam is not easy to see with the IR card. Therefore, in order to double check the maximization of the responsivity, after finding the sharp image of the blade on the detector (see the previous chapter for more details), we repeated the scan of the surface reference sample for different positions of the imaging unit. The result is interesting and is shown in Figure 4.9. The central peaks of every scan follow the trend shown in the simulation in the previous chapter.

As the PCI method is based on laser interference, the fringes contrast is inversely proportional to the wavelength. So, the 1310 nm probe responsivity is expected to be about half of the 633 nm probe one. The final calibration done with both the probe is shown in Figure 4.10.

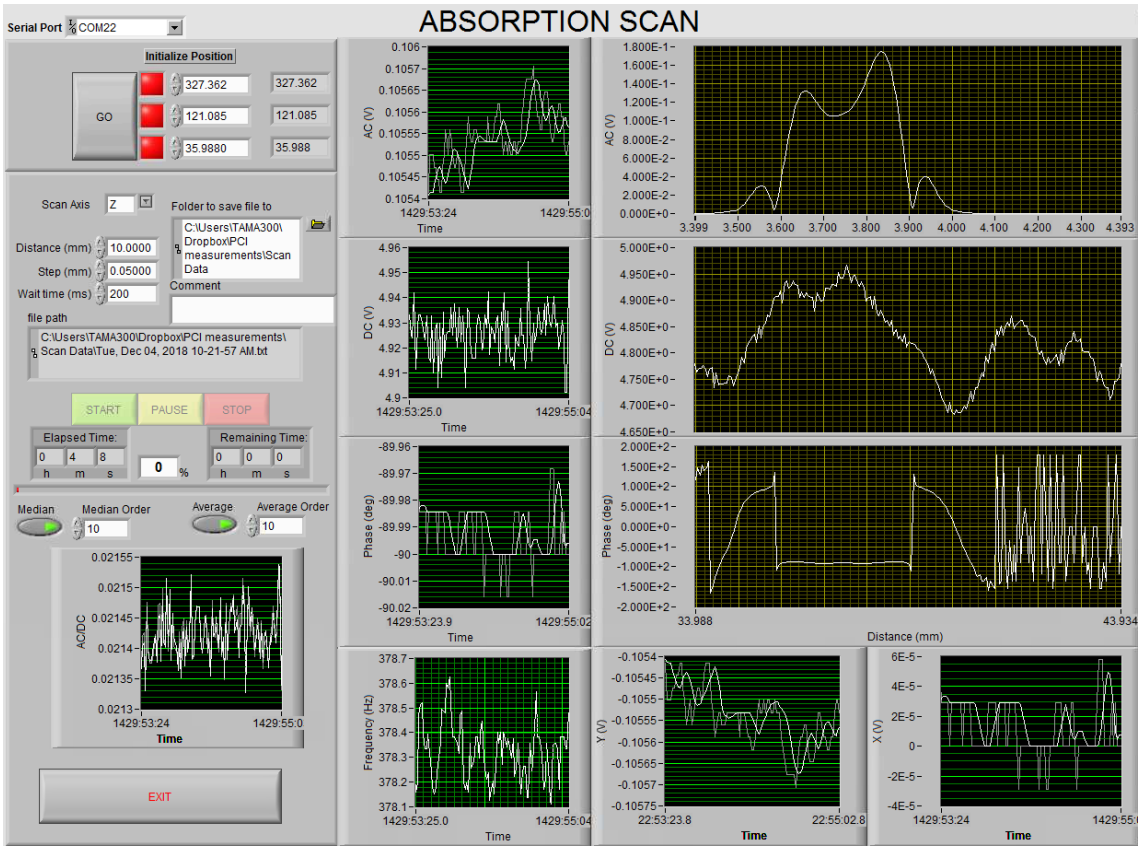

Figure 4.7: Front panel of the VI that make the scans. The button "GO" initializes the communication with the lock-in amplifier and with the translation stage. A subVI sends the measurement settings to the lock-in and starts the data acquisition. We can choose the filter order for the median and the average. The real-time data flow in the charts: the not filtered data in grey, and the filtered data in white. The charts display the AC, the DC, the phase, the chopper frequency, the X and Y lock-in outputs, and the AC/DC. Before starting the scan, we can set the scan axis (X, Y or Z), the initial translation stage position, the distance and resolution of the scan, and the waiting time between the measurements. The file name where to save the data is automatically set as the current date and time. After clicking on the button "START" the scan will step by step show up in the plots on the right: the AC, the DC and the phase of the scan. There is also a progression bar to tell the elapsed and remaining time.

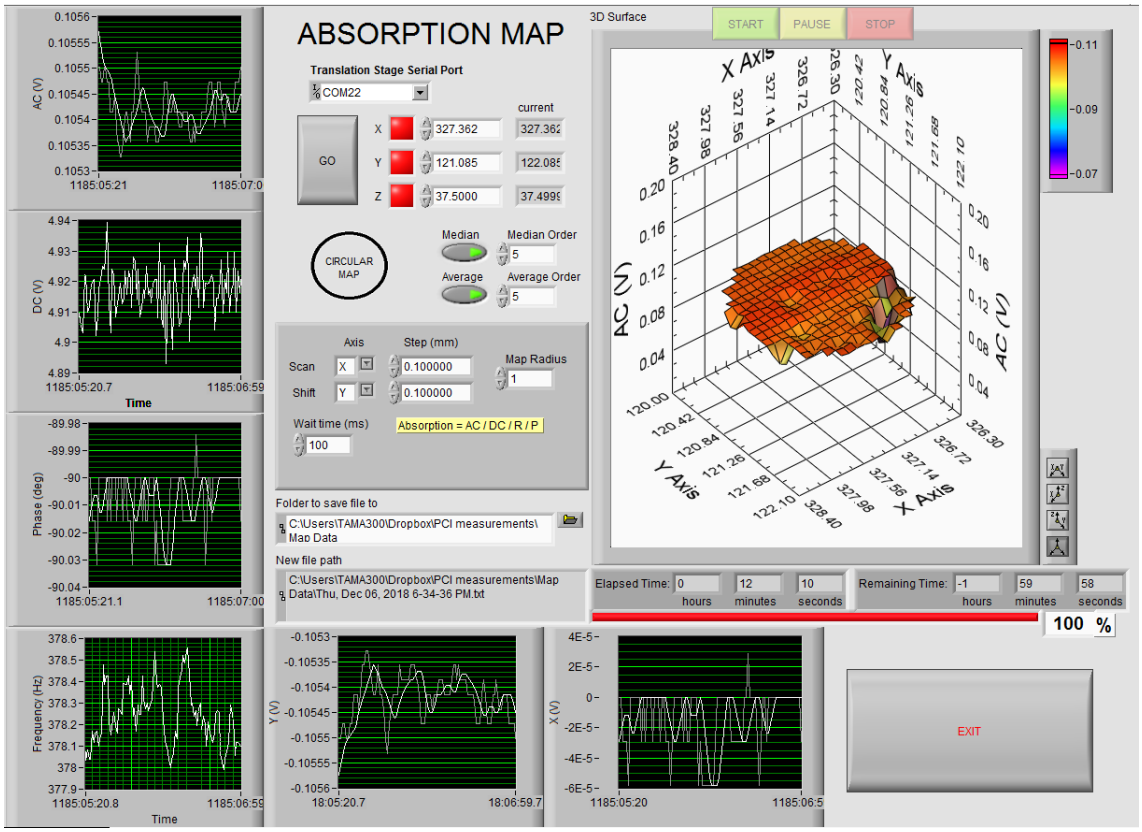

Figure 4.8: Front panel of the VI that make the maps. As for the scan VI, the button "GO" initializes the communication with the lock-in amplifier and with the translation stage. A subVI sends the measurement settings to the lock-in and the data acquisition starts. We can choose the filter order for the median and the average. The real-time data flow in the charts: the not filtered data in grey, and the filtered data in white. The charts display the AC, the DC, the phase, the chopper frequency, and the X and Y lock-in outputs. The scan and shift axis (X, Y or Z) will determine the map plane (XY, XZ, or YZ). Clicking on the "CIRCULAR MAP" we can switch to RECTANGULAR MAP mode. In the case circular map, the initial translation stage position is the center of the map. The resolution is separately set for the two directions. When switching to RECTANGULAR MAP mode, the radius control disappear and the two directions distance controls appear. We can choose the folder where to save the data, and the file name is automatically set as the current date and time. After clicking on the button "START" the map will step by step show up as a AC signal surface in the 3D plot on the right. There is also a progression bar to tell the elapsed and remaining time.

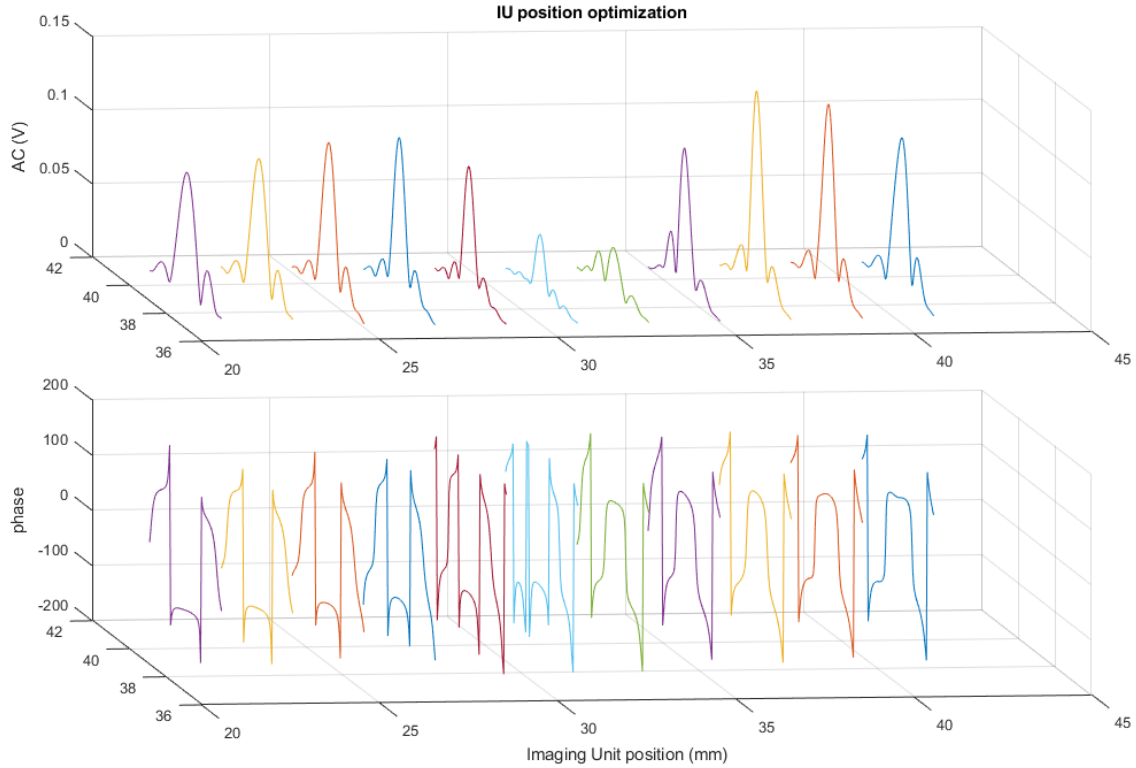

Figure 4.9: Responsivity optimization. Scan of the surface reference sample for different positions of the imaging unit. The AC signal peaks have two maxima and a minimum, while the phase of the peaks has a trend similar to the Guoy phase of a gaussian beam. This trend was already shown with the simulation in the previous chapter. We place the imaging unit at 27 mm: of the two maxima it is the one with the same phase as the HeNe calibration.

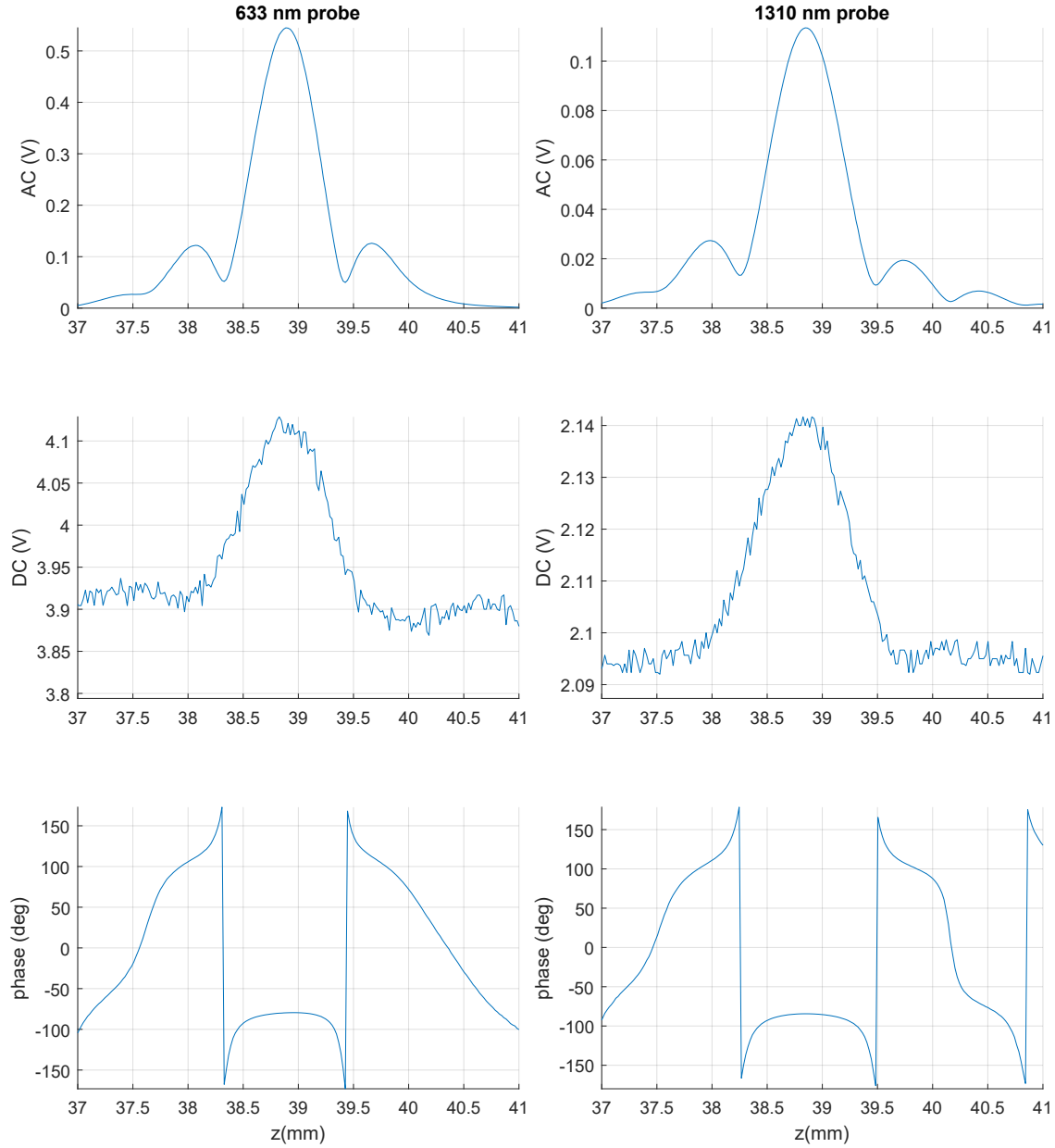

Figure 4.10: Surface calibration sample (Newport FRQ-ND02) scanned along the depth z using the two probes. On the left the HeNe at 633 nm, and on the right the 1310 nm probe. In both the scans, the AC signal central peak is proportional to absorption, pump power and DC, and the side peaks are due to the interference fringes. The DC is almost constant except the central bump which is due to the stationary temperature distribution. The phase plot also shows the typical shape that changes sign at the corresponding AC side peaks. Given the sample absorption Abs=0.2, the pump power P=34 mW and the AC and DC values of the central peak, the responsivities are R=19.4 W^{-1} for the 633 nm probe and R=7.9 W^{-1} for the 1310 nm probe.

4.7 Noise

In this section, I report how we managed to reduce various noises, such as vibrations, temperature fluctuations, dust and probe intensity noise.

4.7.1 Chopper vibrations

An important noise source is the mechanical chopper. The vibrations of the chopper propagate along the optical table causing noise at the modulation frequency. In the original setup the chopper was isolated putting it on a rubber sheet, but in the new setup, the isolation with the rubber was not enough, so we hung the chopper from the ceiling in a way that it doesn't touch the optical table. It is reasonable to think that the new setup is more sensitive to vibration because the probe laser sources and the imaging units sit on two separated optical boards. To shield the acoustic noise of the chopper, we placed a rubber and plastic acoustic panel, and the pump passes through a small hole in this panel.

4.7.2 Probe reflection

Even if the chopper is quite far from the imaging unit, reflections of the probe that reach the chopper generate modulated scattered light that appears in the readout as a constant phase signal and can be confused with absorption signal. We stopped the reflection of the HeNe probe by placing an aperture on the pump beam path.

4.7.3 Cleanness

Dust is an important issue is this kind of high precision measurements with high power lasers for two main reasons. Firstly, when a dust particle passes trough a laser beam, it is seen as a spiky noise in the readout. Secondly, if there is a dust particle on the sample surface, then, when the high power laser passes over the dust, it burns leaving a stain on the surface, and if the surface is coated, it burns the coating as well leaving a permanent damage. To avoid those damages, the absorption measurement system is placed inside a clean-booth. There are two HEPA filters blowing clean air. To avoid the dust coming off the holes of the optical table, we covered the table surface with an anti-static film, the same material of the clean-booth's walls. Before entering the clean space, we placed another clean-booth to wear the clean-suits and where is the computer that controls the system. According to many clean

environment experts, the best way to keep a clean room clean is to remove the dust wiping every day using clean-room compatible tissues and sticky rollers.

4.7.4 Airflow

The wind from the HEPA filters cause temperature fluctuations which make low frequency noise in the setup, with an AC value up to 1 mV. So it is necessary to shield the sensible parts of the setup with black aluminum panels. We also built a box to cover the imaging unit with aluminum extruded beams and black anodized panels.

4.7.5 1310 nm probe intensity stabilization

The infrared probe is a Thorlabs S1FC1310PM fiber coupled laser source. The output is brought to the optical bread board through a polarization maintaining fiber. After aligning the beam and maximizing the responsivity, we did a noise investigation and found that the 1310 nm laser was affected by more noise than the HeNe probe. Indeed, the calibrated noise for the 633 nm probe (for surface absorption) is 0.3 ppm*W, which means that with the maximum available pump power, 10 W, the sensitivity is 0.03 ppm. The calibrated noise with the 1310 nm probe is 4 ppm*W, which is not low enough to measure the absorption of the crystalline coatings. This noise is dominated by the intensity fluctuations of the laser diode. In order to stabilize the laser intensity, we engaged a control loop using the modulation input of the S1FC1310PM. A non-polarizing beam splitter selects 10% of the probe intensity, then a f=50 mm lens focuses it inside the area of the in-loop photo-diode. The rest 90% is used for the PCI setup, and arrives on the detector used for the absorption measurement, which is the out-of-loop photo-diode. The servo is a low noise voltage pre-amplifier SR560 that takes the in-loop PD signal, subtracts the offset from a DC generator, applies a first order low pass filter at 30 Hz, amplifies with a gain of 2000 and sends the correction signal to the modulation input. In Figure 4.11 there is the result of this stabilization loop. The noise in the out-of-loop photo-diode is reduced by 10 dB. This is consistent with the factor of 3 noise reduction in the PCI readout, see Figure 4.11.

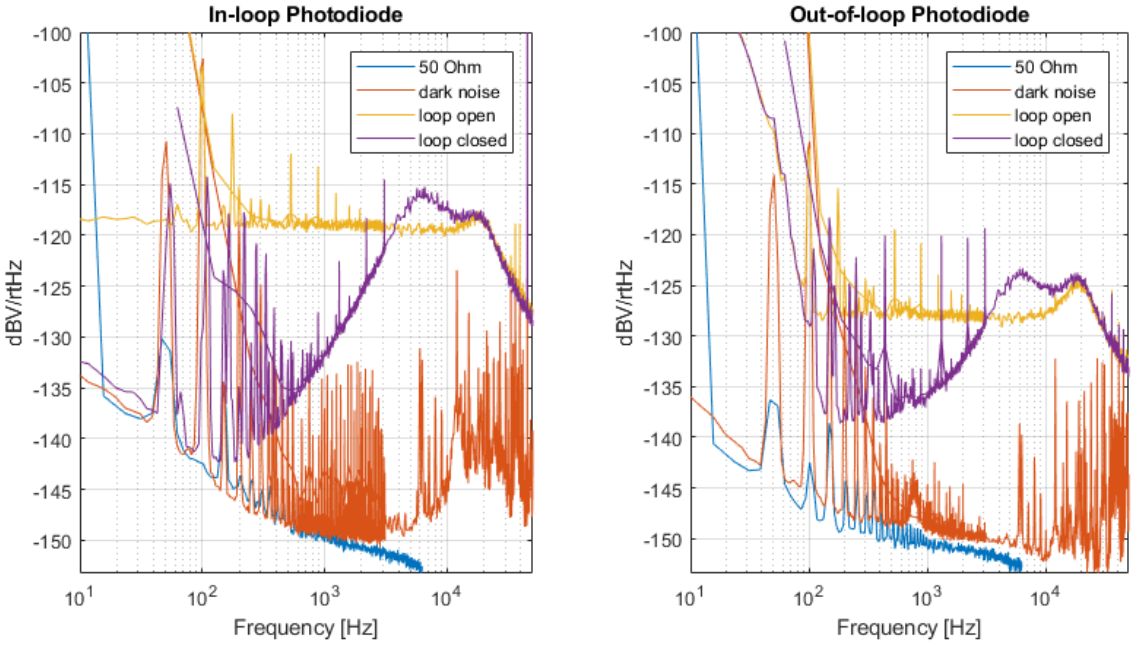

Figure 4.11: 1310 nm probe control loop for the intensity stabilization. On the left, the noise spectra of the in-loop PD and on the right, the noise spectra of the out-of-loop PD. The data are taken with a Yokogawa2400 spectrum analyzer and transferred to the PC through a GPIB port controlled with a LabVIEW VI. The blue curve is the 50 Ω terminator that shows the floor noise of the spectrum analyzer. The red curve is the PD dark noise taken with the probe laser OFF. The yellow curve is the noise without the control loop. The purple curve is the noise with the control loop. On the in-loop PD, the beam is entirely inside the sensitive area, while, in the out-of-loop PD, the beam is much larger than the PD, therefore it is more sensitive to jitter noise (vibrations), and this shows in the spectra with more noise at low frequencies. The noise reduces by 20 dB at 400 Hz in the in-loop PD, and by 10 dB at 400 Hz in the out-of-loop PD.

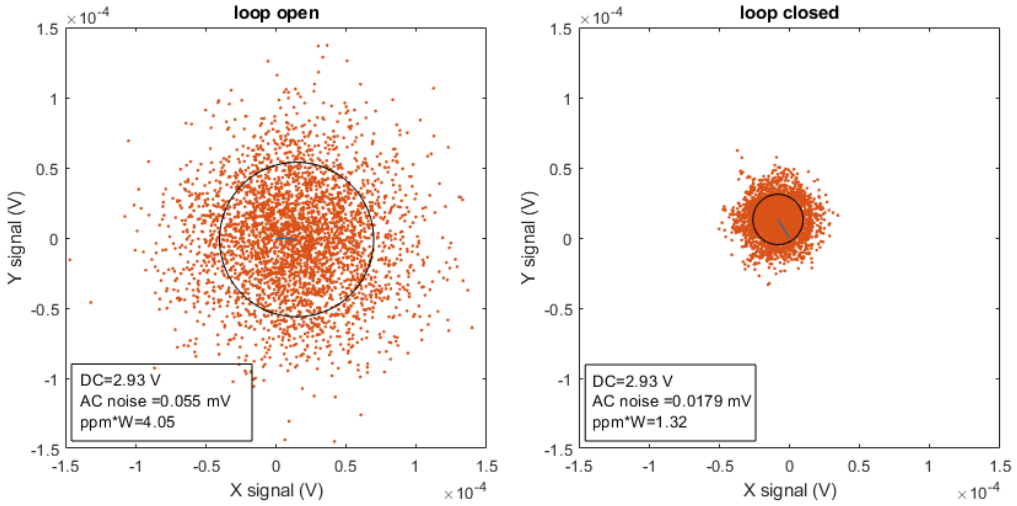

Figure 4.12: Noise reduction in the readout of the 1310 nm probe. With the control loop for the intensity stabilization the noise reduces from 4 ppm*W to 1.3 ppm*W. This means that now, with the maximum pump power, we have enough sensitivity to measure absorption of the order of 0.1 ppm

4.8 Calibration validation

Once the alignments optimization, the responsivity maximization and the noise reduction were done, we tested some samples and compared the results with the other labs to confirm and validate the calibration. For the sapphire absorption, we tested a small sample from Shinkousha and sent it to the SPTS company in Hawaii. The result in Figure 4.13 shows that the calibration is compliant with the original setup company within 20%.

For the crystalline coating absorption, we tested an amorphous coating provided by LMA with an absorption value of 0.65 ppm. We measured it with the 1310 nm probe and found a value of 0.7 ppm, with a good signal to noise ratio.

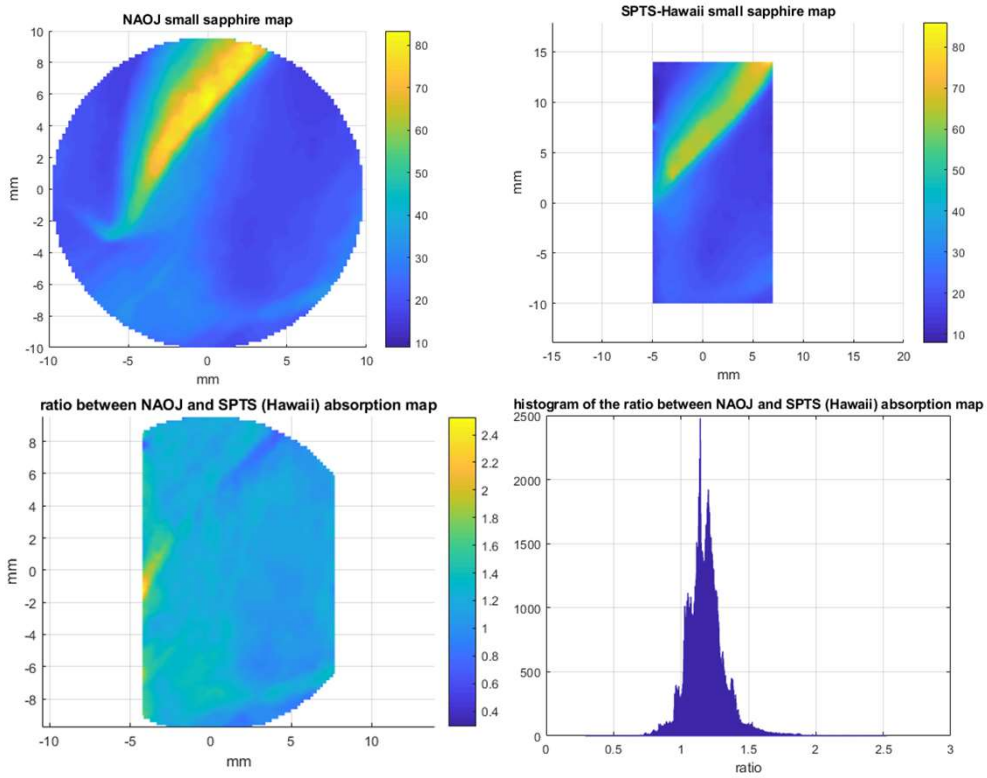

Figure 4.13: Comparison of the absorption measurements on the small sapphire sample from Shinkousha. On the top left, the absorption map done with the upgraded setup at NAOJ (colorbar in ppm/cm). On the top right, the map done on the same sample at the laboratory of the SPTS company. On the bottom left, the map of the ratio. To make the ratio point by point we shifted the maps along X and Y until the minimum of the map standard deviation. On the bottom right, the histogram of the ratio. The result is that there is a ratio of 1.17+/-0.2, which means that the calibration is compatible with the SPTS one.

4.9 Conclusion

We upgraded the setup with a large translation stage to measure large KAGRA substrates and an infrared probe at 1310 nm to measure crystalline coatings. We checked the calibration and found a good agreement with the company that sold us the original setup. We reduced various noise sources and reached a sensitivity of 0.03 ppm with the HeNe probe and 0.1 ppm with the infrared probe. This sensitivity is enough to measure the AlGaAs crystalline coatings which are expected to absorb less that 1 ppm. In the next chapter, we report the measurements we did on several sapphire samples including a KAGRA substrate. In Chapter 6, we report the measurements we did on the crystalline coating.

Chapter 5

Sapphire absorption measurements

As explained in Chapter 2, sapphire absorption is a critical aspect for KAGRA and for future cryogenic detectors. The amount of heat to be extracted by the cryogenic system has to be minimized. The main heat source in the mirror is the optical absorption, which depends on the material optical quality. In this chapter, we present a study of several sapphire substrates quality in terms of absorption. We report the absorption measurements done during this thesis work. In the first section, we show the properties of sapphire. In the second section, we list the measured sapphire substrate samples. In the third section, we report the absorption measurements done on these samples using the upgraded PCI system.

5.1 Sapphire

Sapphire is the crystalline form of aluminum oxide Al_2O_3. The crystal has trigonal hexagonal scalenohedral structure. The unit cell has lattice constants a =4.75 Å and c = 12.98 Å. In nature, sapphire has different colors depending on the contamination with various metals, but the industrial sapphire crystals for optical applications are highly pure, therefore transparent. The typical growth method is the Czochralski process or one of its variants. The alumina is melted in a crucible and a small crystal seed is dipped in the melt while rotating around the vertical axis; then the seed is pulled upward and the melt crystallizes creating the mono-crystal boule. The crystal is grown along the a-axis. Sapphire has refractive index $n = 1.76$ and birefringence 0.008. For the KAGRA mirrors the c-plane was chosen as the mirror surface so that the birefringence doesn't affect the interferometer. In Table 5.1 the main properties

of sapphire are summarized.

Density	3980	kg/m^3
Thermal conductivity	30	W/(m K)
Thermal capacity	760	J/Kg K
Young's modulus	370	GPa
Poisson's ratio	0.22	-
Refractive index	1.76	-
dn/dT	13.1×10^{-6}	1/K

Table 5.1: Sapphire properties

5.2 Samples

The crystal maker company SHINKOUSHA CO., LTD. provides different size of mono-crystals. This company has been working together with the KAGRA collaboration to make crystals of large size and increasingly optical quality.
We have 4 samples that we measured. They are not coated. Here below there is a list of them in order of increasing size:

- 1 small substrate: 1.5 inches in diameter, 8 mm in thickness, 36 g in weight.
- 2 substrates of the same size of Tama300 mirrors:
  100 mm in diameter, 60 mm in thickness, 1.87 kg in weight.
- 1 substrate for KAGRA test mass:
  22 cm in diameter, 15 cm in thickness, 22.7 kg in weight.

To put the samples on the large translation stage, we used the mounts of different sizes shown in Chapter 4.

5.3 Absorption measurements

In this section, we present the results of the bulk absorption measurements of the sapphire samples listed in the previous sections.

5.3.1 Calibration

The PCI system can measure surface absorption and bulk absorption. As presented in Chapter 3 and Chapter 4, we have two reference samples that we use for calibration. For the calibration of sapphire substrate absorption, we use a bulk reference made of Schott glass #12. The thermal properties of Schott glass are different from sapphire, in particular, sapphire has higher diffusivity. The calibration factor R, must be corrected when changing sample material. Since there are many experimental factors that play important role in the calibration, the most accurate way to take them all into account is to find the calibration material correction factor experimentally. The SPTS company made several tests on a large number of materials and found a correction factor of 3.34 between Schott glass #12 and sapphire. This means that the responsivity of sapphire is 3.34 times lower than the reference sample. This is also in agreement with the simulations presented in Section 3.9.2. In other words, the calibrated sapphire measurement result has to be multiplied by this factor. The advantage of this way is that only one reference sample is needed for many materials (provided a factor for each material). The drawback is that, to keep these factors valid on different setups, the experimental parameters such as the chopper frequency, the beam sizes, the angle between pump and probe, and the imaging unit distances must be the same within 10%. At first, when we upgraded, reassembled, and realigned the setup, we set the pump and probe beams to be larger than the original setup. We also did a mistake on how we calculated the pump power inside the sample. This led to a calibration discrepancy that we noticed after we measured all the sapphire samples. After fixing these problems (restoring the correct beams' size and calculating the correct pump power), we measured again the small sapphire sample and found a uniform factor of 2.25 between the old measurement and the new measurement. As reported at the end of Chapter 4, the measurement on the small sapphire sample is compliant with the SPTS company measurement within 20%. The measurement presented in this chapter were taken with the initial upgraded setup, and then re-scaled by the factor of 2.25. Future measurements will not have to be re-scaled.

5.3.2 Small size substrate

This is the sapphire sample that has been measured with our setup several times, and by the SPTS company. In this section, we report the absorption maps that we did, which are compliant with SPTS. In Figure 5.1 there are the circular map at

the center of the sample, the rectangular maps on the XZ plane, and YZ plane. In Figure 5.2 we put together the three maps in a 3D plot, and show the relative size of the maps and the sample. In the captions of the figures, there are the experimental details on the map acquisition.

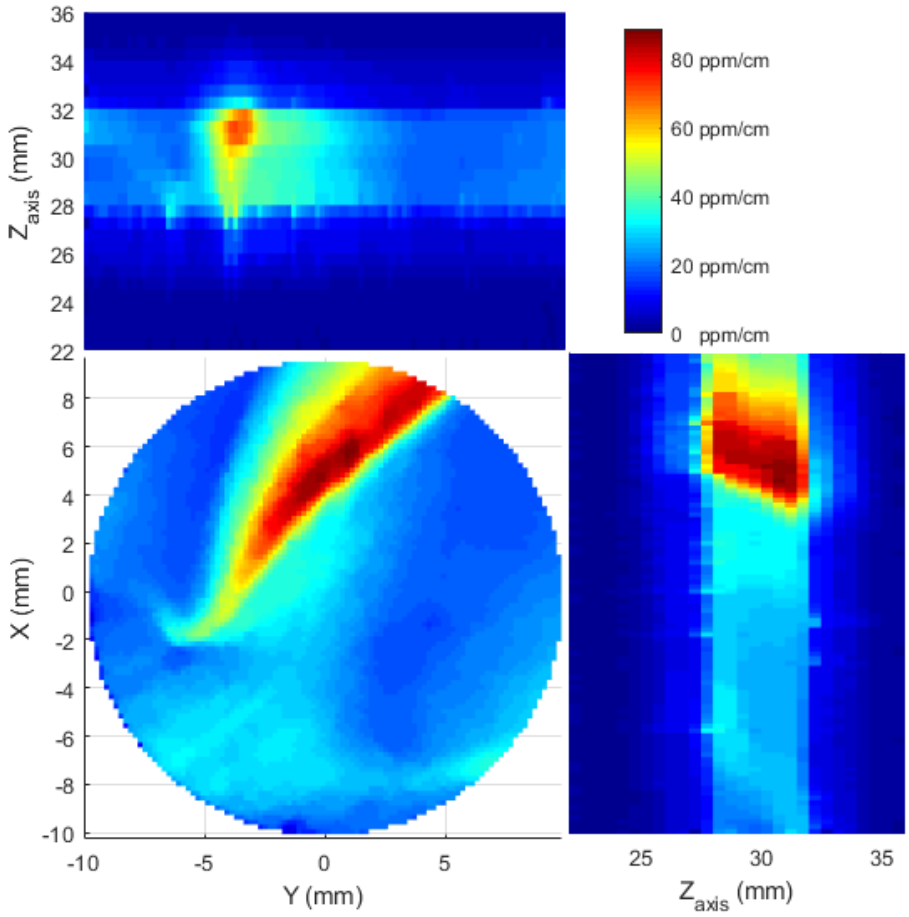

Figure 5.1: In the center, the circular map. It is taken at the half depth of the sample, and it has a diameter of 20 mm and a resolution of 0.2 mm. On the top and on the right, the rectangular maps on the YZ, and on the XZ plane, with a resolution of 0.2 mm along X and Y, and 0.5 mm along Z. The waiting time between two points was 1 s, the digital filters on the time domain are an order 10 median filter and an order 10 average filter. The circular map took about9 hours to be done, and each rectangular map about 4 hours. There is also a median filter of order 3 on the map, to smooth out the peaks which are probably due to some dust on the surface. The dark blue areas on the rectangular maps correspond to the zero absorption outside the sample. X, Y and Z_{axis} are coordinates of the translation stage. As explained in Chapter 3, the refraction inside the sample makes the sample thickness appear 1.81 times smaller, according to the Snell's law.

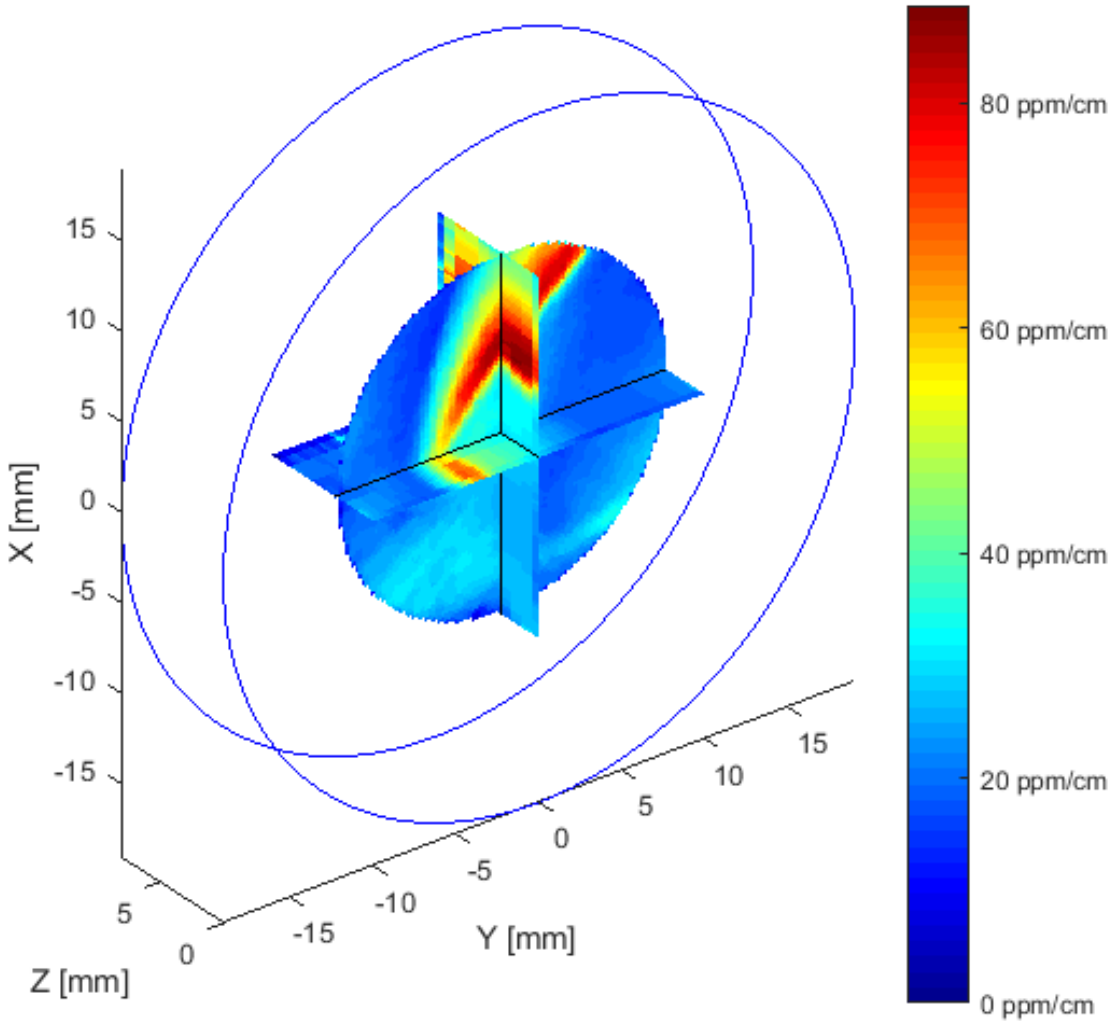

Figure 5.2: The 3D reconstruction of the absorption inside the small sapphire sample. It is a combination of the maps shown in Figure 5.1. To show the relative size of the maps and the sample, the two circles represent the boundaries of the sample. The rectangular maps are stretched along the Z direction by a factor of 1.81 to match the real Z axis. In this plot, the rectangular maps show the real thickness of the sample.

5.3.3 Tama300 mirror size substrate

In this section, we report the absorption maps that we measured on the Tama300 mirror size sapphire substrates provided by Shinkousha.

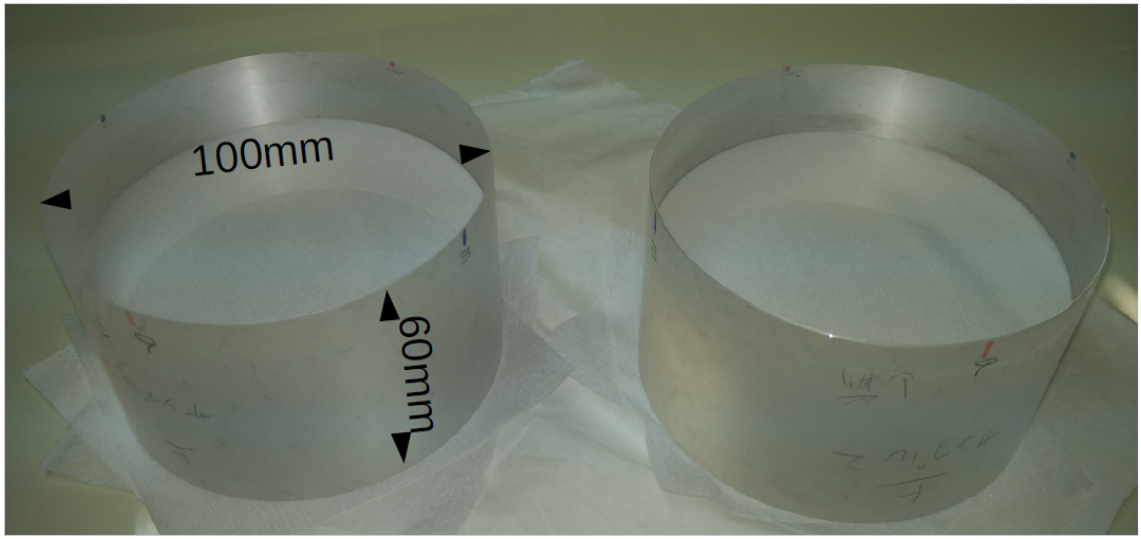

Figure 5.3: Picture of the two sapphire substrates with the size of Tama300 mirrors.

In Figure 5.4 and in Figure 5.6 there are the absorption maps on the Tama300 size Sample #1 and Sample #2. The resolution along the X and Y axis (perpendicular to the laser beam) is 100 µm, which is of the same order of the pump beam size. The resolution along the Z axis is 1 mm, which is of the same order of the length of the pump-probe interaction region. The lock-in integration time is 100 ms. A median filter and an average filter of order 10 are applied to each point measurement. There is a waiting time of 1 s from point to point. This makes the acquisition time about 9 hours for each circular map to be completed. The rectangular maps are on the XZ and YZ planes, they cover the whole depth of the sample and 1 cm along X and along Y around the central axis of the sample. The circular maps have a diameter of 1 cm, they are aligned to the center of the sample and taken at different depths. In Figure 5.5 and Figure 5.7, the final plots of each sample are a 3D combination of all the maps together. The drawn large circles in the 3D plot represent the border of the surfaces of the sample, this gives an visual idea of how large are the maps compared to the sample size. Since the maps are taken during several days, it is important to notice that at the intersection between perpendicular maps, the same color (absorption value) appears. This shows that the system has a good repeatability in time.

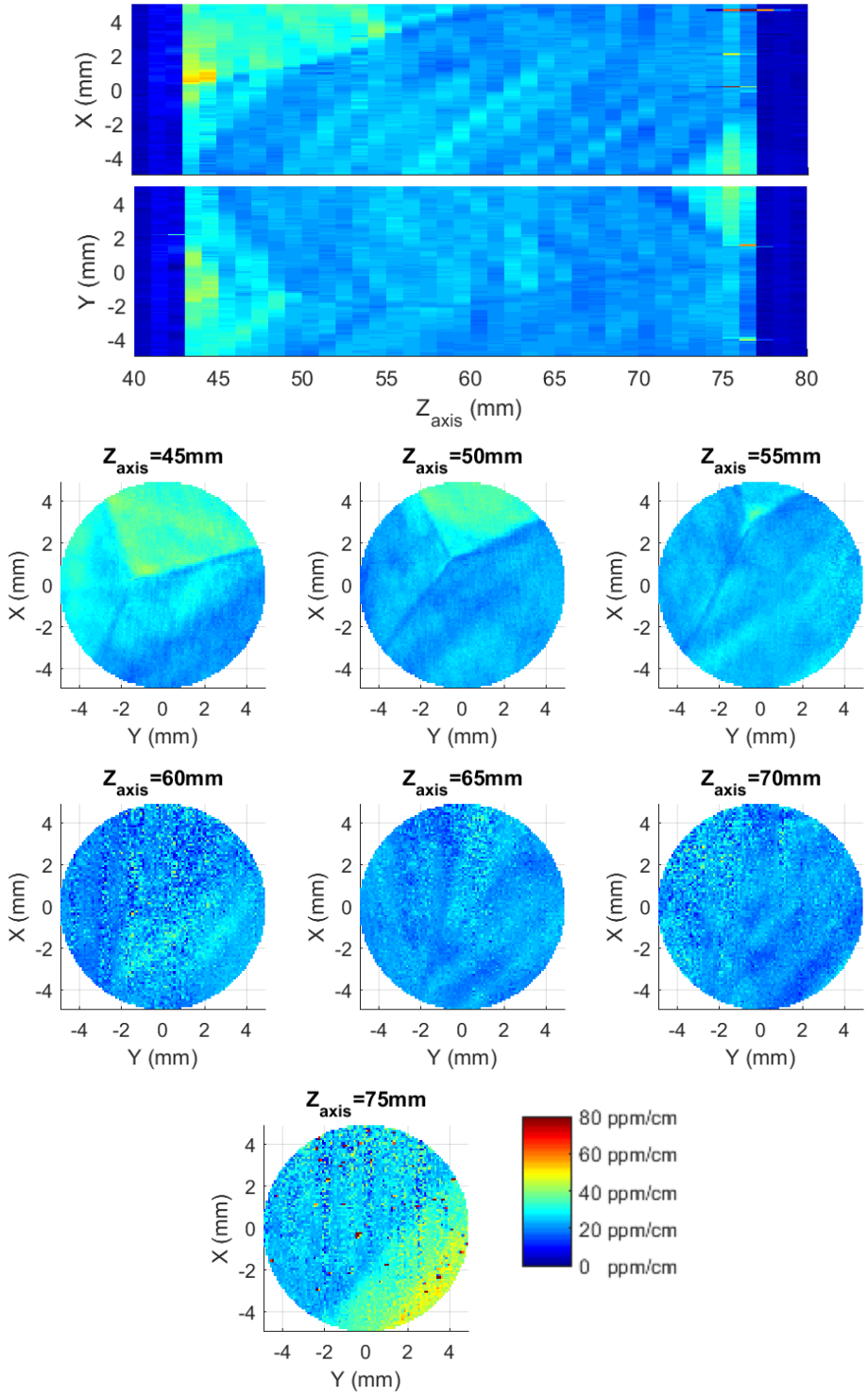

Figure 5.4: Tama300 size Sample #1. Absorption maps. Experimental details are described in the text.

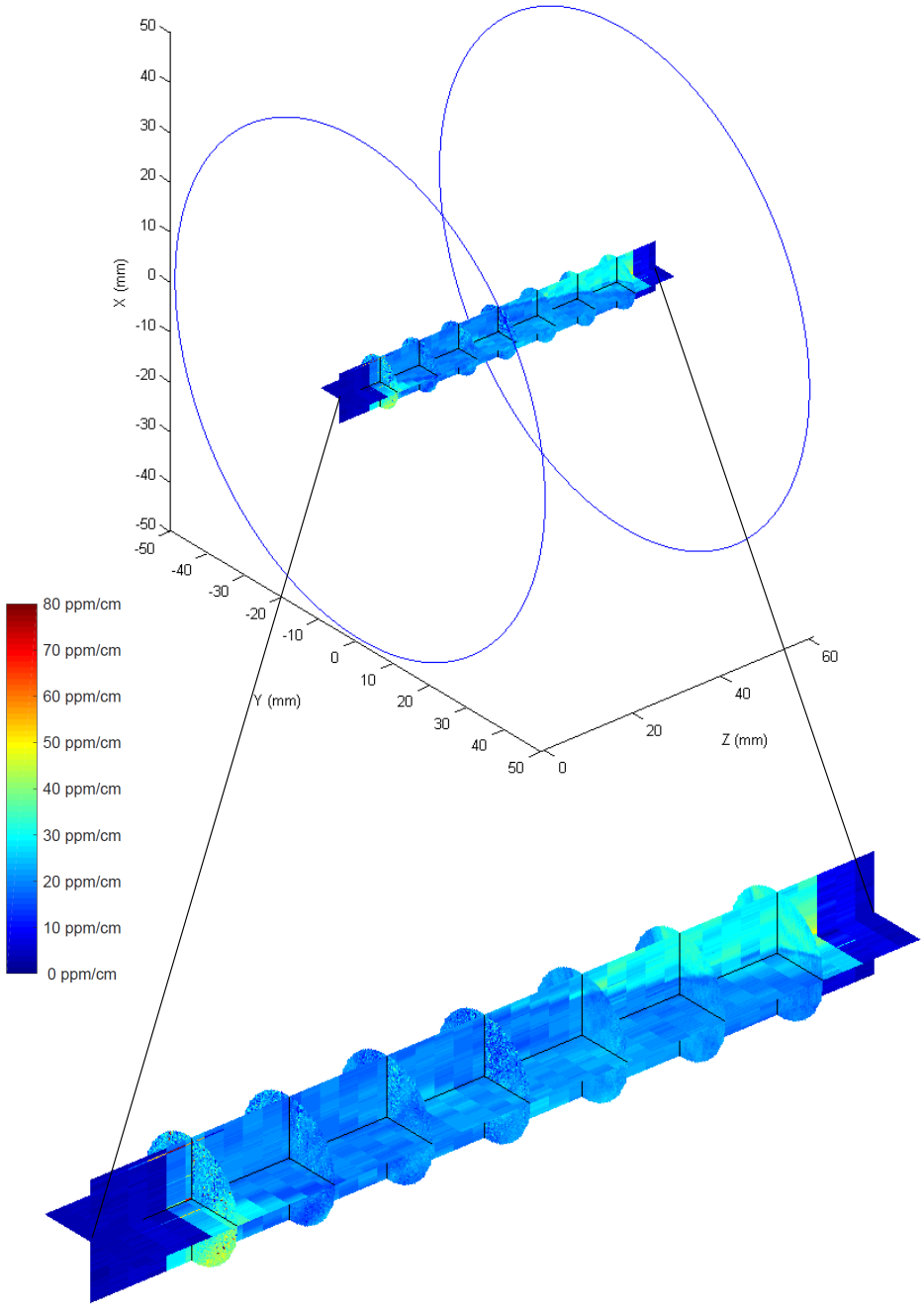

Figure 5.5: The 3D reconstruction of the absorption inside the Tama300 size sample #1. It is a combination of the maps shown in Figure 5.4. On the bottom, a zoom in of the plot to see more details.

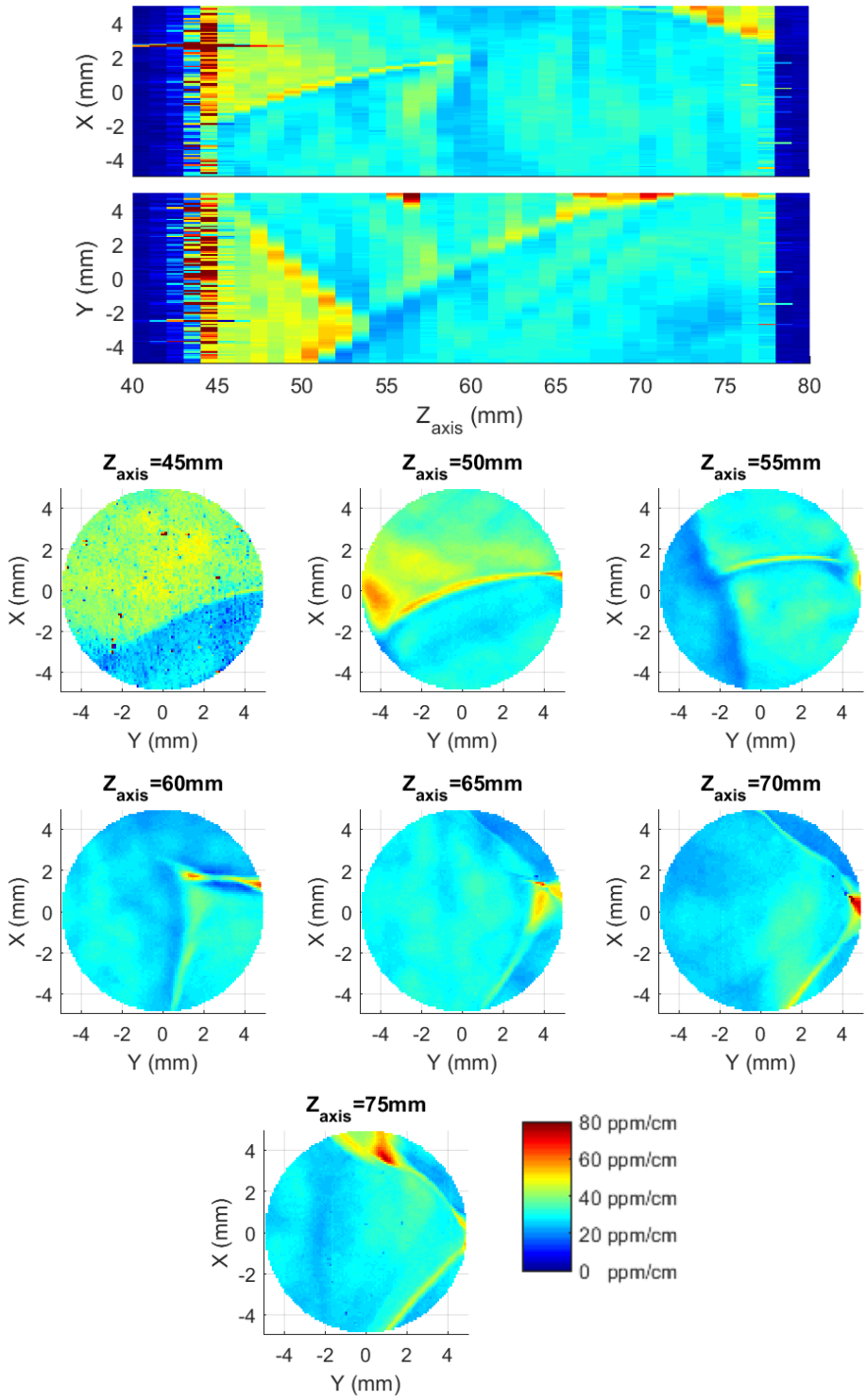

Figure 5.6: Tama300 size Sample #2. Absorption maps. Experimental details are described in the text.

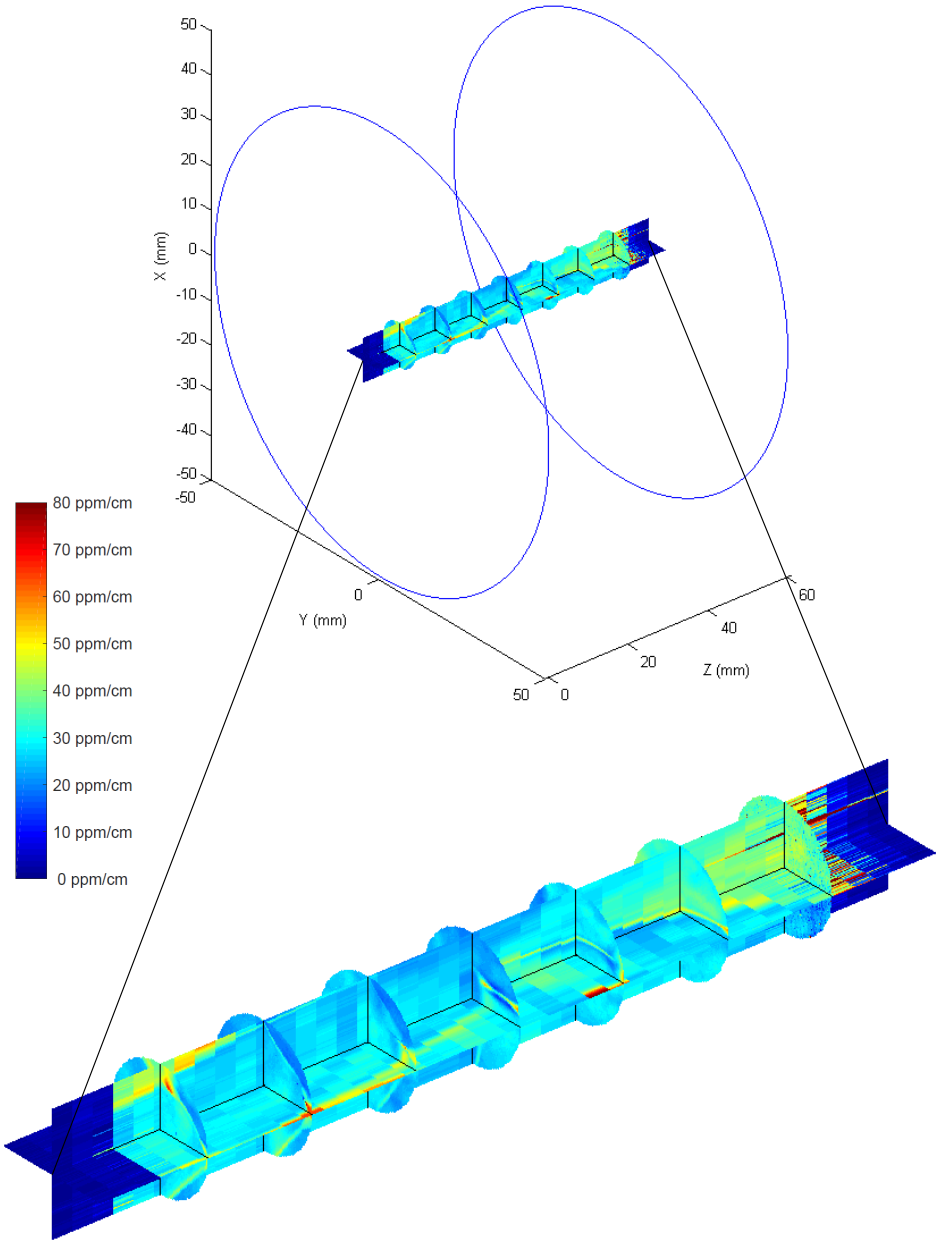

Figure 5.7: The 3D reconstruction of the absorption inside the Tama300 size sample #2. It is a combination of the maps shown in Figure 5.6. On the bottom, a zoom in of the plot to see more details.

5.3.4 KAGRA test mass substrate

In this section we report the absorption maps that we did on a KAGRA sapphire test mass substrate. The sample was manufactured by Shinkousha and tested in Caltech. It didn't fulfill the KAGRA absorption requirements (<50 ppm/cm) so it is currently a spare sapphire substrate for KAGRA. It is labeled substrate #7. The crystal *c*-axis is oriented along the Z axis of the translation stage.

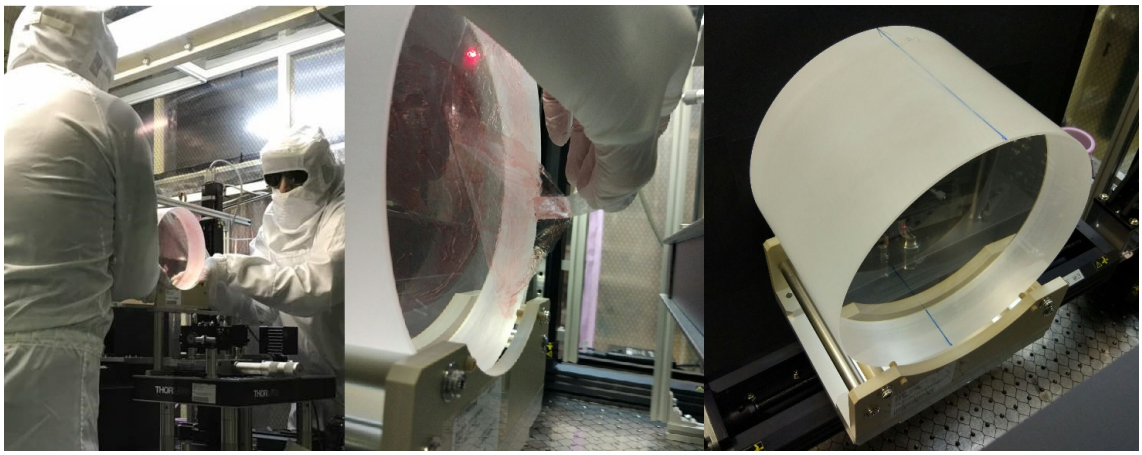

Figure 5.8: KAGRA substrate placement on the translation stage. Before moving the sample, a layer of red First Contact™ polymer is applied on both the surfaces to clean the surface and to protect the sample from contamination or scratches during the transportation. First, we put the substrate on the mount. The mount has two handles, for an easier and safer grabbing of the heavy sample ($\simeq$ 23 kg). Two people are needed to carry the mass safely. We grab the mount handles, and we carry it on the translation stage.

We did three circular maps on the XY plane at three different depth in the sample: at about 1 cm from the first surface, in the center, and at about 1 cm from the second surface. The maps are 120 mm in diameter and 1 mm of resolution, the waiting time is 1 s and the digital filters are an order 10 median filter and an order 10 average filter. The circular maps are shown in Figures 5.9, 5.10, and 5.11. Then we did two rectangular maps on the XZ plane and on the YZ plane that cross the central axis of the sample. The size is 120 mm along X and Y (the same as the circular maps), and 105 mm along Z (enough to scan the sample from one surface to the other). The resolution is 1 mm in both the directions. The rectangular maps are shown in Figures 5.12, and 5.13. In Figure 5.14, we put together the 5 maps in a 3D plot and show the relative size of the maps and the sample.

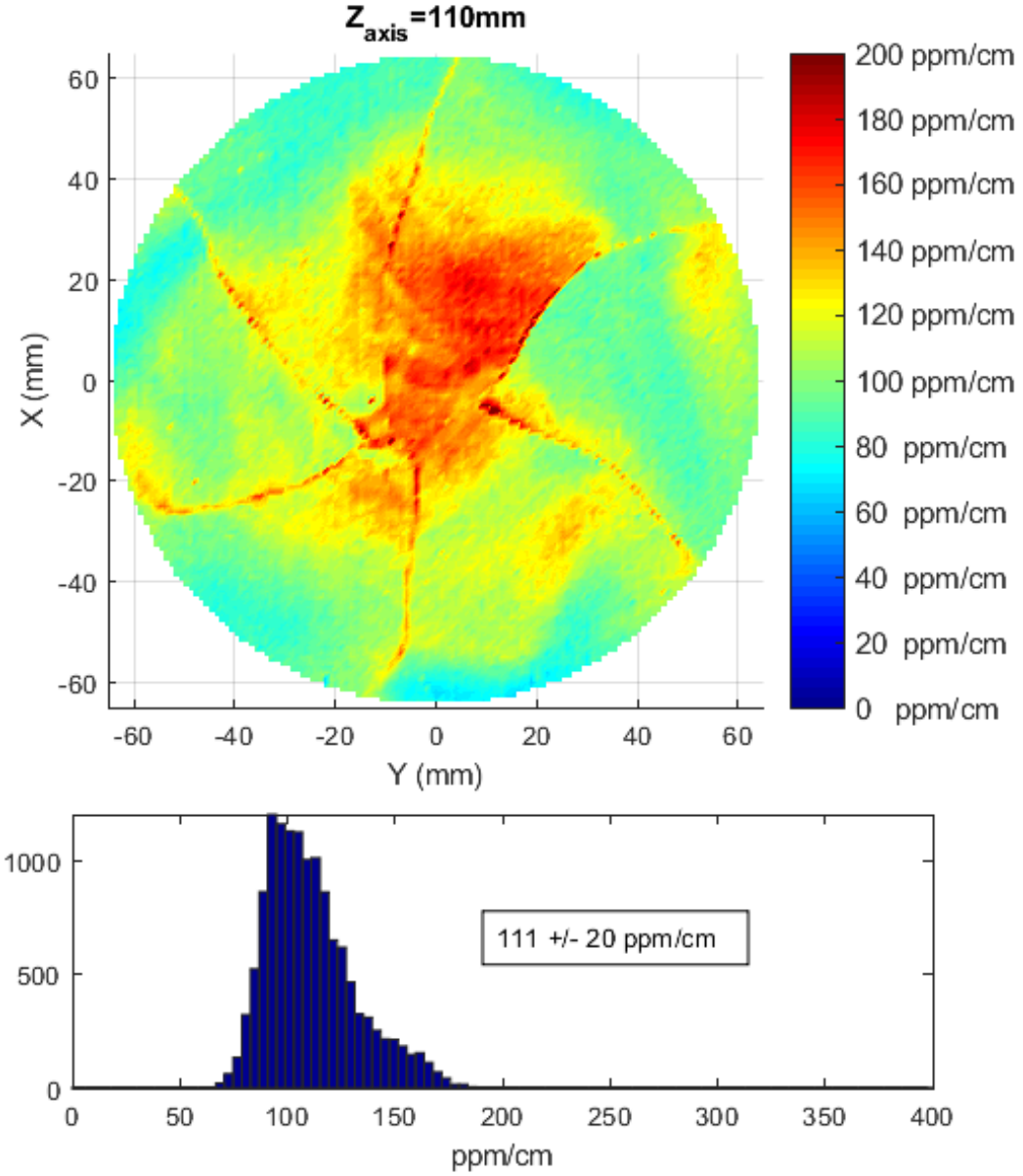

Figure 5.9: On the top, the circular absorption map of the KAGRA substrate at Z=110 mm on the translation stage coordinate, which corresponds to about 1 cm from the first surface. On the bottom, the histogram of the map. We can see the star-like structure that is due to the crystalline structure. The average absorption is 111 ppm/cm.

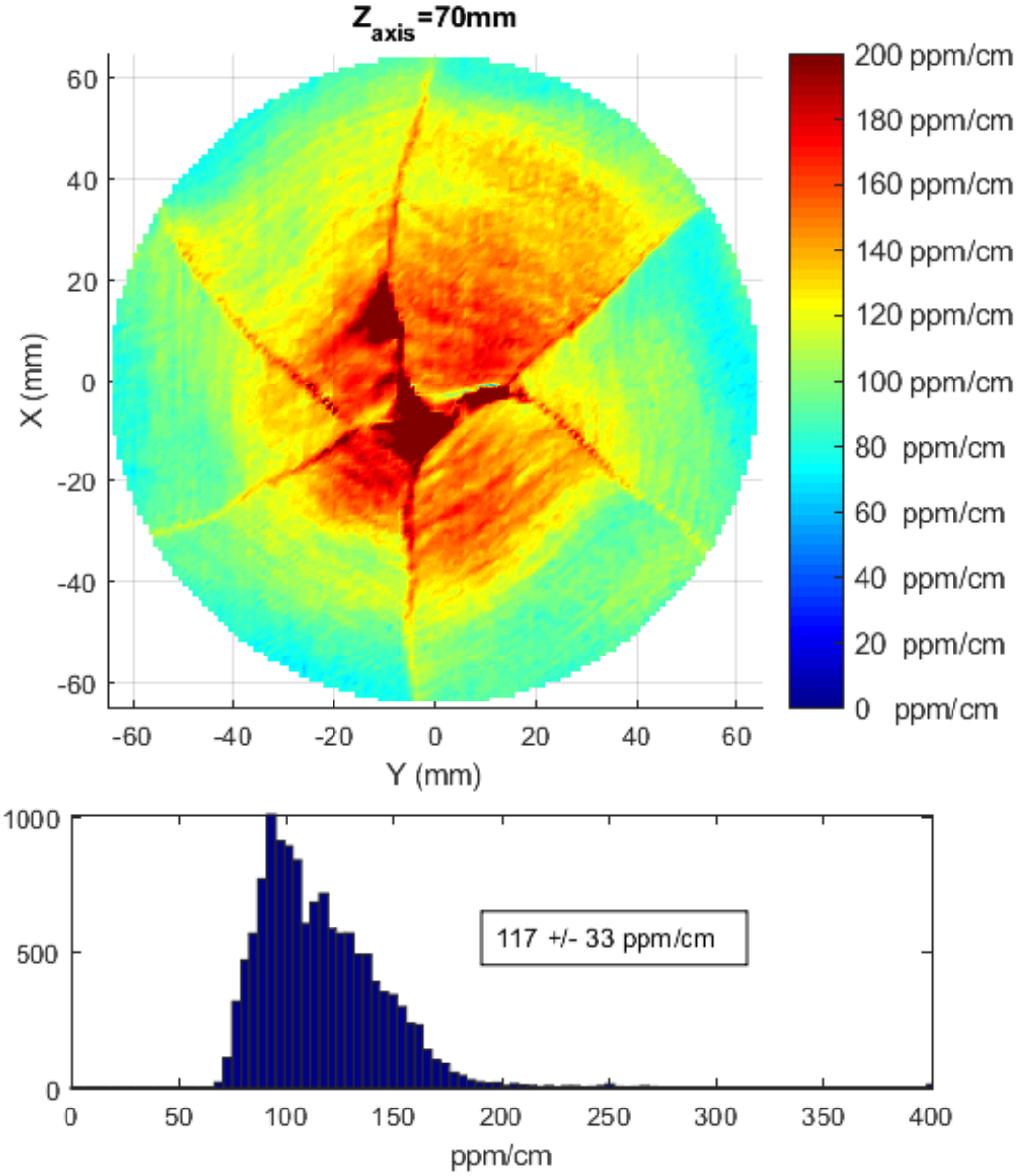

Figure 5.10: On the top, the circular absorption map of the KAGRA substrate at Z=70 mm on the translation stage coordinate, which corresponds to about the center of the sample. On the bottom, the histogram of the map. We can see the star-like structure that is due to the crystalline structure. The average absorption is 117 ppm/cm.

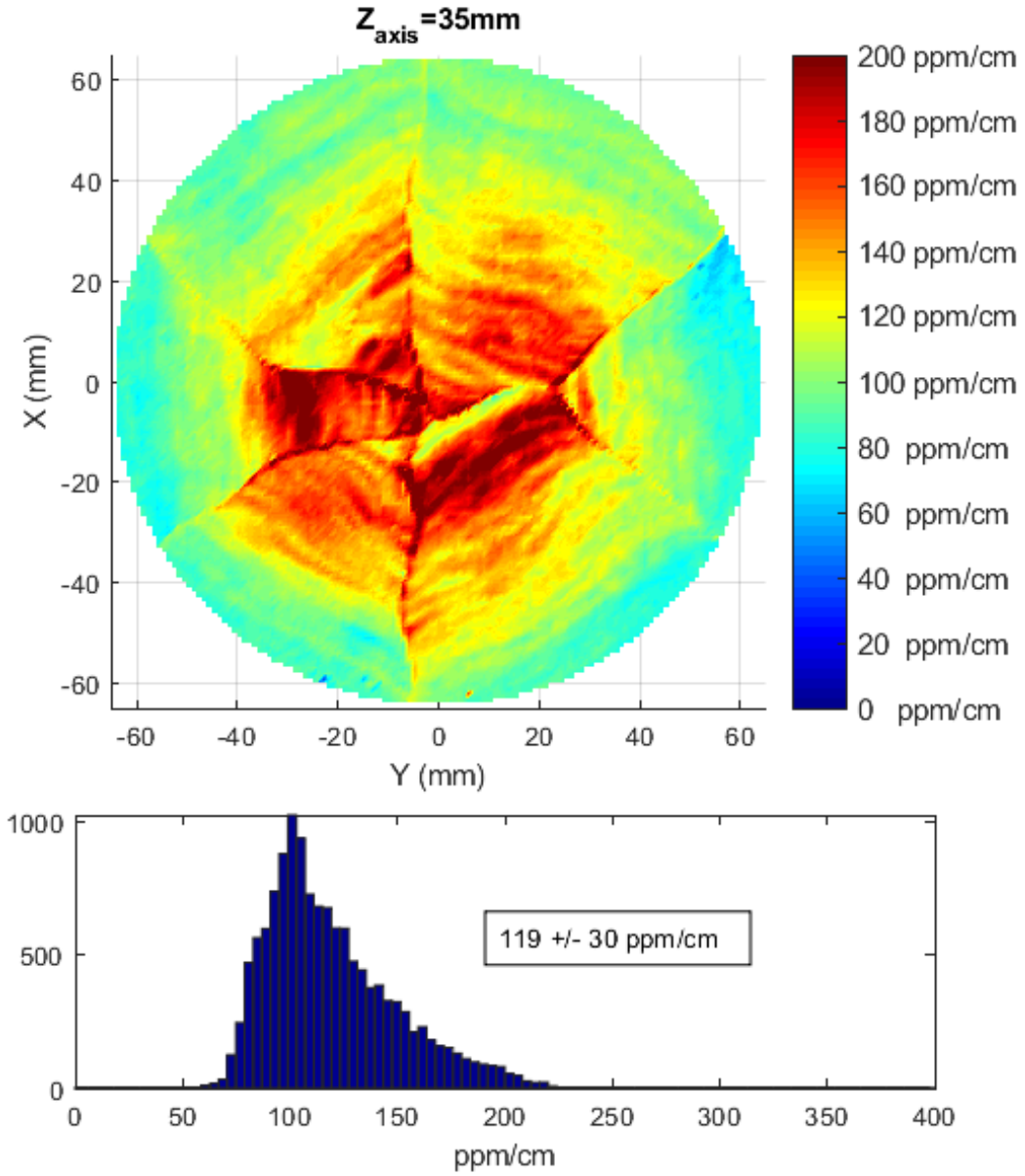

Figure 5.11: On the top, the circular absorption map of the KAGRA substrate at Z=35 mm on the translation stage coordinate, which corresponds to about 1 cm from the second surface. On the bottom, the histogram of the map. We can see the star-like structure that is due the crystalline structure. The average absorption is 119 ppm/cm.

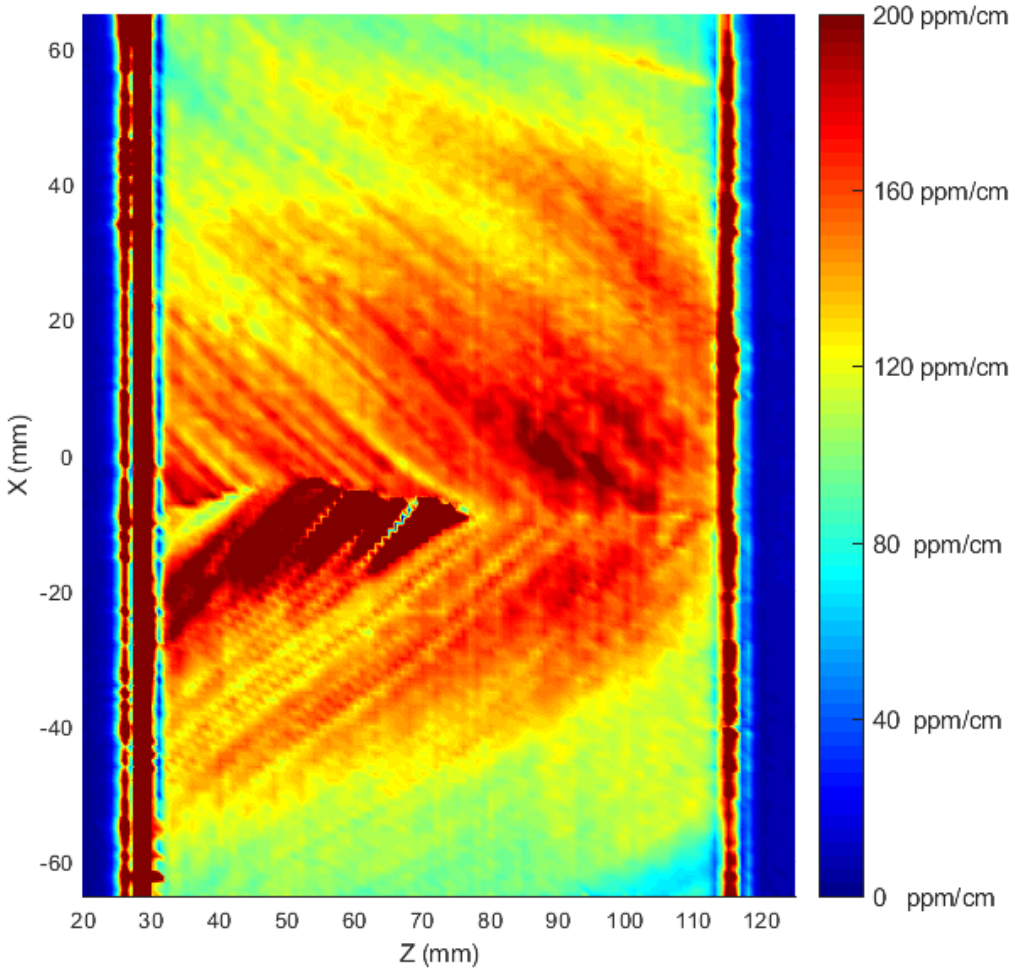

Figure 5.12: Rectangular absorption map of the KAGRA substrate on the XZ plane. As explained in Chapter 3, in the translation stage Z coordinate, we scan the whole sample thickness (150 mm) by moving the sample by 85 mm. At Z=30 mm the crossing point is on the second surface, and at Z=105 mm the crossing point is on the first surface. The dark blue areas correspond to the 0 absorption outside the sample. On the surfaces, there is a large absorption that saturates on the colorbar, probably due to non-optimal polishing. We can see an interesting fish-bone-like structure that shows the crystal growth direction.

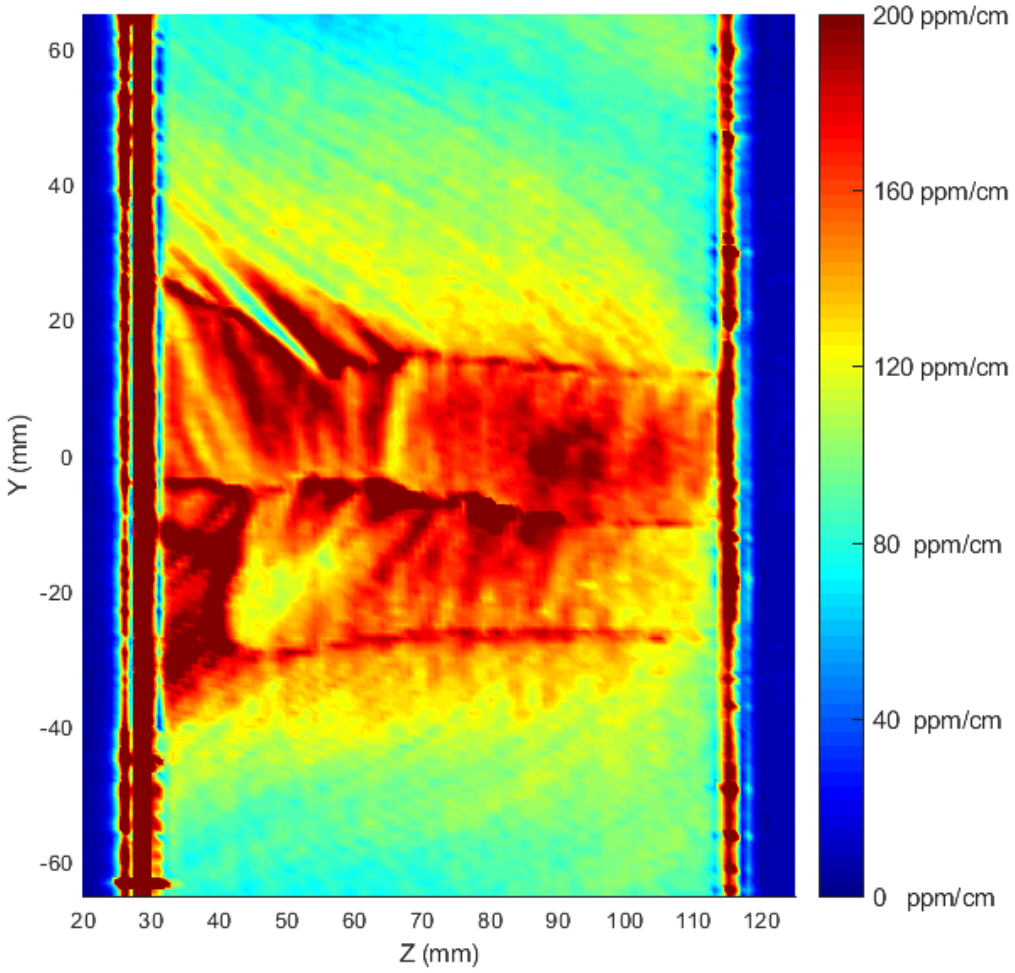

Figure 5.13: Rectangular absorption map of the KAGRA substrate on the YZ plane. As in Figure 5.12, at Z=30 mm the crossing point is on the second surface, and at Z=105 mm the crossing point is on the first surface. The dark blue areas correspond to the 0 absorption outside the sample. On the surfaces, there is a large absorption that saturates on the colorbar, probably due to non-optimal polishing. We can see an interesting fish-bone-like structure that shows the crystal growth direction. Also, there are three main "veins" that correspond to the star-like structure in the circular maps.

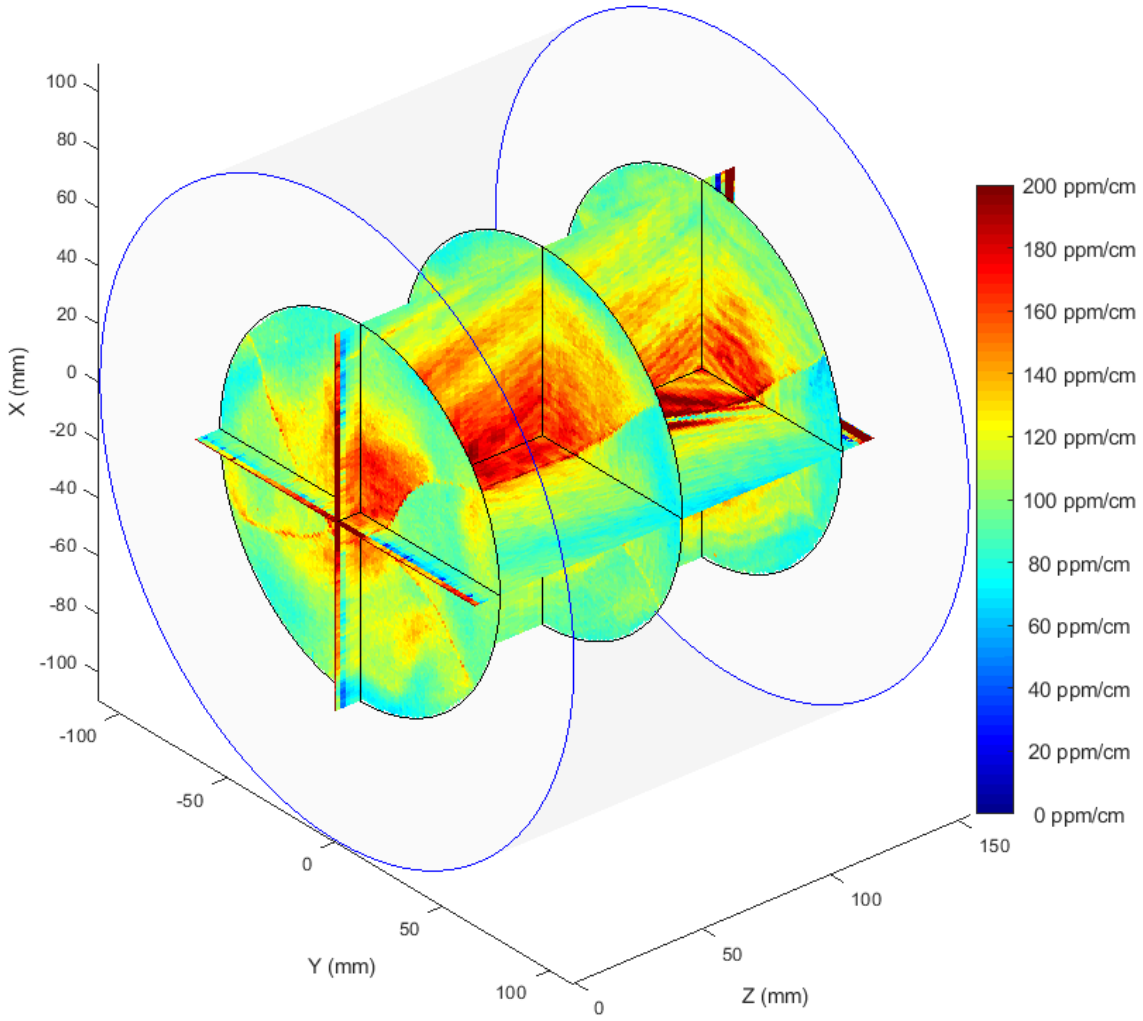

Figure 5.14: The 3D reconstruction of the absorption inside the KAGRA substrate. It is a combination of the maps shown in Figures 5.9, 5.10, 5.11, 5.12, and 5.13. The rectangular maps are stretched to match the real size of the sample. The two blue circles with the gray shadow represent the size of the sample. The absorption value perfectly matches in the intersections between perpendicular maps.

5.3.5 Discussion and conclusions

Our setup has enough sensitivity to measure the absorption of these sapphire substrates with very good signal to noise ratio. We did maps with a resolution that allowed us to see the absorption structures inside the substrates.

In all the KAGRA substrate circular maps, we see an interesting star-like absorption structure. This is related to the sapphire structure, it has an hexagonal symmetry and it is due to the dislocations in the crystal. Rather than being point-like defects, the dislocations tend to propagate during the crystal growth. They originate at the seed, where the crystal growth starts. The rectangular maps show a different section of the substrate. Perpendicularly to the star-like structure, we can see the fish-bone structure, from which we can recognize the crystal growth direction. Most of the absorption is concentrated around the center of the mirror, which is also the rotational axis during the growth. This is not a good thing for the test mass of the interferometer because also the laser power is concentrated in the center of the mirror. We also see a large absorption on the surface. This is because the substrate didn't fulfill the requirements for KAGRA and it was not finely polished for the coating deposition.

The dislocations, and therefore the absorption, strongly depend on the material purity and on the growth procedure. The crystal maker company is doing some investigation and continuous improvements in this aspect. The goal of this thesis was to characterize the sapphire substrates. Until now, only 2D maps of the sapphire absorption at different depth were made. With the setup developed during this Ph.D. thesis, we are now able to make 3D maps, which means to resolve the absorption along the z-axis continuously. As we saw in the results in Figure 5.12, Figure 5.13, and Figure5.14, this new setup allowed to get new information about the absorption structure inside the crystal. In the smaller sapphire substrates we didn't see such interesting absorption structures as much as in the large substrate. This shows that, as the size increases, it is more difficult to make low and uniform absorption crystals. As a plan for the future, these results are going to be shared with the crystal makers, in a collaboration that will allow further improvement of sapphire quality.

The future upgrades of next generation gravitational wave detectors go in the direction of increasing the test masses size. With our setup, after small upgrades of the translation stage, it will be possible to measure even larger substrates and collaborate with the crystal maker to scale up the size of high quality sapphire

substrates.

Chapter 6

Crystalline high-reflectivity coatings characterization

The current sensitivity of the second generation gravitational wave detector is limited at mid-frequencies by thermal noise. As introduced in the first chapter, there are many contributions to thermal noise, such as the suspensions, the substrate and the coating. In this chapter we present an R&D work aimed to reduce thermal noise in high-reflectivity coatings for future upgrades of KAGRA. In Section 6.1 we explain the motivation of this R&D work. In Section 6.2 we describe the novel coatings produced by the company "Crystalline Mirror Solution". In Section 6.3 we show the results of the absorption measurements that we did at LMA using a photo-deflection method, and at NAOJ using the PCI setup developed in this Ph.D. Thesis and described in Chapter 4. In Section 6.4 we present the optical performance measurements that we did in collaboration with LMA and that have been published [2]. In Section 6.5 we present the result of the direct thermal noise measurement that we did at MIT using an advanced setup developed by LIGO.

6.1 Introduction

As explained in the first chapter, Brownian fluctuations are related to mechanical dissipation. The mirror thermal noise power spectral density is proportional to the Boltzmann constant k_B, the temperature T, the coating mechanical loss angle ϕ, and the inverse of the frequency f, namely $G(f) \propto k_B T \cdot \phi \cdot 1/f$. The loss angle is the parameter that describes the coating mechanical quality factor $Q = 1/\phi$, where ϕ is defined as the imaginary part of Young's modulus $E = E_0[1 + i\phi]$ [34]. Current dielectric silica and tantalum pentoxide (SiO_2/Ta_2O_5) multilayer high-reflectivity

coatings deposited by ion beam sputtering (IBS) have loss angles of the order of 10^{-4} [35]. Pushing to lower loss angles on this amorphous materials would require the development of thin film with lower mechanical losses. Given the exceptionally high mechanical Qs found in bulk glasses (i.e. melt grown synthetic silica), through modifications to the deposition process, it may be possible to significantly reduce the mechanical dissipation in amorphous coatings. However, despite the effort, small improvements have been achieved so far on this side.

In contrast, high-reflectivity interference coatings based on substrate-transferred crystalline coatings have already demonstrated significant reductions in mechanical loss [27]. For this alternative solution, the challenge remains in scaling-up the manufacturing process. New optical materials for high-reflectivity coatings based on epitaxial or single-crystal materials are currently under investigation. Fabrication of such coatings is a technological challenge because optical applications such as atomic clocks and interferometric gravitational wave detectors require extremely high material purity, excellent surface quality, and, in the case of gravitational wave detectors, large coating diameters, typically of 20 cm and beyond. Substrate-transferred epitaxial multilayers based on single-crystal GaAs/AlGaAs heterostructures are promising candidates for alternative low-loss and high-reflectivity mirror coatings. These coatings have been demonstrated to provide a tenfold reduction of Brownian noise, compared with amorphous coatings, with a reduction of the mechanical losses down to $\phi = 2.5 \times 10^{-5}$ at room temperature [27], and the potential for a loss angle below 5×10^{-6} at cryogenic temperatures [28]. In addition to low losses, high-precision laser interferometers require the mirrors to have very low total integrated scattering, below 10 ppm, to reduce stray-light phase noise. Since scattering is mainly caused by the surface roughness, the coating's micro-roughness must be very low. Moreover, absorption should be well below 1 ppm to minimize thermal lensing and to maintain a low base temperature in a cryogenic interferometer like KAGRA. Given the requirement of high-reflectivity, stringent thickness control is necessary to maintain the target transmission value. In the following sections, we present the characterization of the optical performance of the first large-area (5 cm diameter) crystalline coatings. This characterization was carried out to understand the current state of the technology and to provide motivation for further developments.

6.2 Large-area crystalline coatings

The samples for this study are high-reflectivity multilayer mirrors designed for a center wavelength of 1064 nm at room temperature. The interference coatings are based on a Bragg structure made of 35.5 doublets of epitaxial GaAs/$Al_{0.92}Ga_{0.08}As$ layers grown via molecular beam epitaxy (MBE). These layers are originally grown on a 15-cm diameter GaAs wafer with negligible lattice mismatch with the low-index $Al_{0.92}Ga_{0.08}As$ layer. The authors would like to stress that the maximum continuous diameter of the crystalline coating ultimately depends on the dimensions of the original GaAs growth wafer. Currently, 20-cm diameter GaAs wafers are commercially available and larger diameters up to 40 cm can be custom-grown. Following lithography and chemical etching processes, coating discs are defined and removed from the growth wafer. These disks are then directly bonded to the final optical substrate, in our case comprising planar fused silica and sapphire. Here, the substrates are 0.5-mm thick with a diameter of 50.8 mm (2 inches). The completed fused silica mirror is shown in Fig. 6.1.

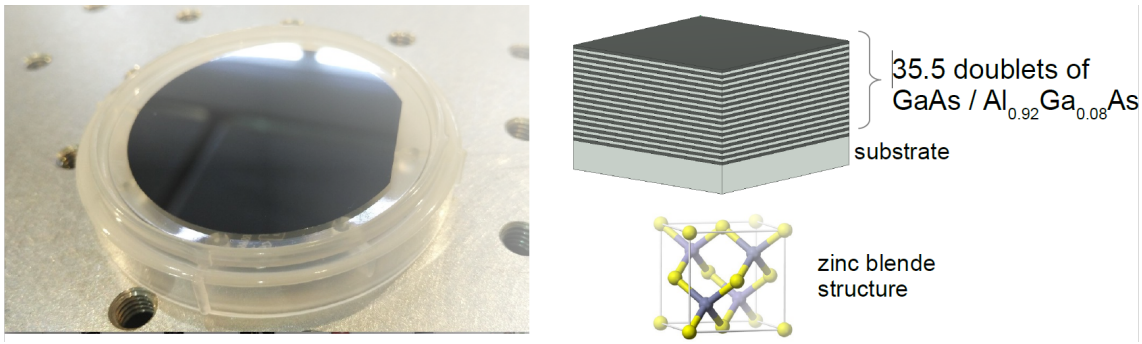

Figure 6.1: On the left: photograph of a substrate-transferred 35.5-period GaAs/ $Al_{0.92}$ $Ga_{0.08}As$ multilayer on a 2-inch diameter × 0.5-mm thick fused silica substrate (lying on a plastic carrier). On the right: drawing of the layers structure and representation of the crystalline structure of the layers material.

Following the transfer process, the mirrors were inspected for bonding defects. Defect points larger than 100 µm are shown in Fig. 6.2 and Fig. 6.3. We also measured the number of defects using a Micromap system (described in Section 6.4). Fig. 6.4 shows the results of the defect mapping tests. The defect density is about 0.85 defects/mm^2, which is comparable with the coating of the End Test Masses of LIGO/Virgo whose defect density is about 0.7 defects/mm^2. However,

we find that the total number of large defects (at the 100 µm or greater size scale) is higher than that of the test masses of Virgo. It is important to note that these samples were among the first crystalline coating prototypes manufactured at this size scale. Note that the substrates employed for these tests, described in detail in Section 6.4, consisted of semiconductor-grade fused silica and c-axis oriented sapphire wafers. To the best of our knowledge, the surface quality of these samples was specified to guarantee excellent yield in bonding. However, in the course of our process development efforts, it became clear that the final substrates possessed properties that were not ideal for direct bonding. As a consequence of these non-ideal surface properties, coupled with a finite surface defect density of the epitaxial material, we were left with the aforementioned large defects at the bond interface. In terms of the limiting surface properties, the fused silica substrates exhibited larger than ideal micro-roughness, while the sapphire samples had an excessively poor surface figure (typically specified as bow/warp for these semiconductor-relevant substrates). The use of optimized epitaxial material with a lower surface defect density, in combination with high-quality "bulk" super-polished substrates, would significantly reduce the defect density in such large-area optics employing crystalline coatings.

6.3 Absorption measurements

In this section, we present the results of the absorption measurements performed with two different setups, a photo-thermal deflection system at LMA and the PCI setup developed during this thesis work in the laboratory of TAMA300 at NAOJ.

6.3.1 Measured at LMA

The absorption system in LMA is based on the photo-thermal deflection method. This technique has been used for many years and is well documented in the literature [38, 39, 31, 40]. In this test, a 1 W pump laser at 1064 nm is modulated with an optical chopper at 210 Hz, in order to periodically heat the sample. The temperature change is proportional to the laser power and to the absorption rate. Since the temperature gradient distribution induces a corresponding refractive index gradient, we use the resulting thermal-lens effect in order to sense the temperature change. A probe laser at 1310 nm (employed as GaAs is transparent at this wavelength) passes through the heated region which imposes a non-uniform wavefront

Defect #	Size (µm)	Defect #	Size (µm)
1	200	10	63
2	85	11	55
3	62	12	121
4	186	13	185
5	65	14	98
6	60	15	117
7	75	16	76 &68
8	75	17	52
9	52	18	271
		19	51

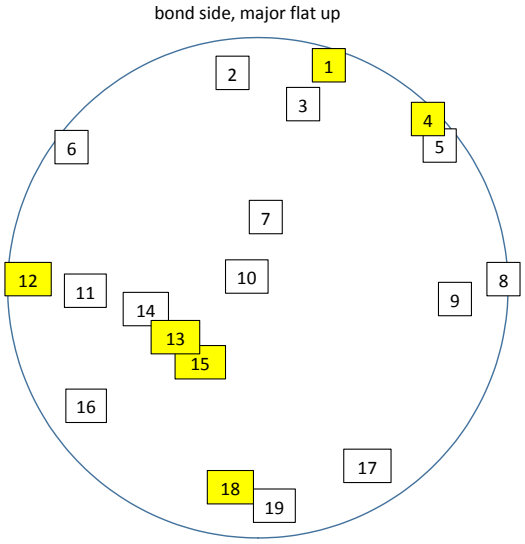

Figure 6.2: Defects observed in the crystalline mirror coating transferred to fused silica [36]. Larger defects are highlighted in yellow. As described in the text, we identify a larger than desired count of visible defects. These defects are not intrinsic to the substrate-transfer coating process, but arise as a consequence of either macroscopic defects in the epitaxial films or, in this case, primarily from the poor surface quality (micro-roughness and figure) of the thin wafers and the resulting non-uniform propagation of the bond wave.

Defect	Size (µm)
A	216
B	690
C	1304
D	957
E	1462
F	941
G	171
H	875
I	250

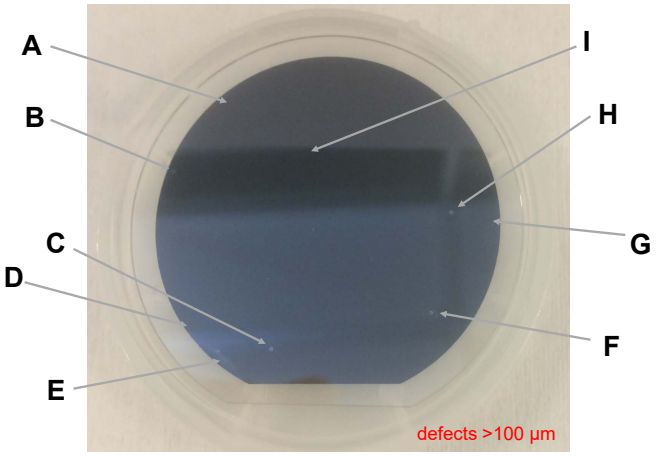

Figure 6.3: Defects observed in the crystalline mirror coating transferred to sapphire. As with the sample transferred to the silica substrate, we identify visible defects as a consequence of non-ideal bonding conditions [37]. Defects larger than 100 µm are indexed with the letters A-I.

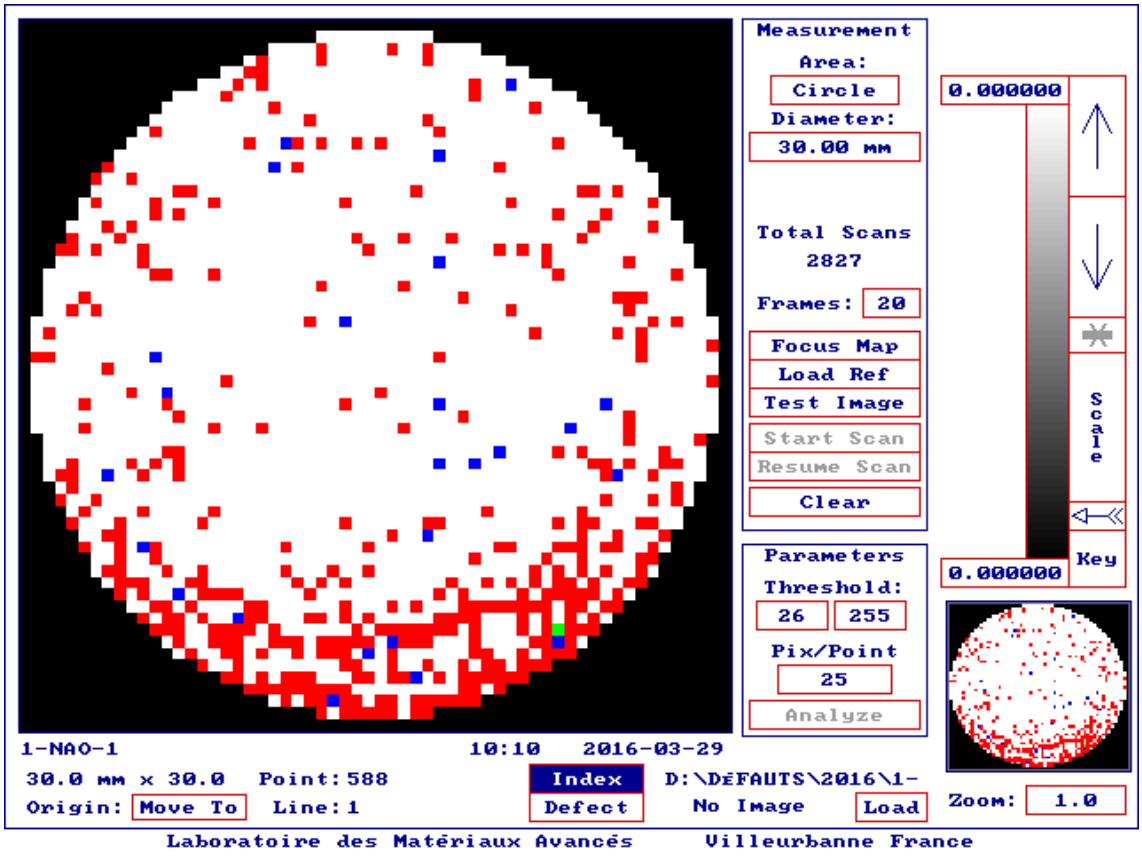

Figure 6.4: Details of the defect count measured with the Micromap setup at LMA for the crystalline mirror coating transferred to sapphire. In this test we record 588 points, 1 line, and 21 regions covering the 2-inch diameter sample surface. The red dots correspond to small defects (<5 µm) and blue dots to large defects (>5 µm).

phase shift that deflects the probe beam. Then, a position-sensitive detector measures the deflection, and this signal is demodulated by a lock-in amplifier to improve the signal to noise ratio. Since the demodulated signal is proportional to the temperature change, using the proper calibration, the absorption rate is measured. The calibration is done using a reference sample, a mirror on a silica substrate, with a known absorption rate of 8.1ppm. The signal is linear with the absorption, so the calibration procedure is a simple proportion. To get rid of long-time fluctuations of the experimental/environmental parameters, the calibration signal was measured on the same day of the measurement. The sensitivity is better than 1 ppm for fused silica samples. Sapphire has a higher thermal diffusivity, so the thermal lens effect is smaller and the sensitivity is worse. The absorption measurement is taken at a single point near the center of each sample. The absorption is very low for both samples. In the case of the coating on the fused silica substrate, the signal is ≤ 0.8 ppm which

is comparable to the setup sensitivity. This result is similar to what is previously reported [41]. In the case of sapphire, the absorption signal is below the noise floor of the measurement. This is because of the above mentioned thermal diffusivity.

6.3.2 Measured with PCI at NAOJ

We used the PCI setup developed during this thesis work and described in Chapter 4 to measure the absorption map of the crystalline coating transferred on the fused silica substrate. The reference sample that we used for the calibration is a Neutral Density filter FRQ-ND02, a silica substrate coated with a thin layer of INCONEL [42] that absorbs 20% at 1064 nm. The calibration scan is done with 35 mW of pump power and it is shown in Chapter 4. The result of the scan is a calibration factor R=7.9 W^{-1}, and a phase of -85 °.

We measured the crystalline coating transferred on the fused silica substrate. First, we did a scan along the depth of the sample (Z axis), then, we set the Z-axis on the position of the scan maximum, and we made a map on the XY plane. We remind that the formula for the absorption is Abs=AC/DC/P/R, where AC is the demodulated signal from the lock-in amplifier, DC is the continuous component of the photo-detector output, P is the pump power, and R is the calibration factor. The result of the scan is shown in Figure 6.5, and the result of the absorption map is shown in Figure 6.6. In addition to the order 50 digital median and average filters, we apply the phase filter that removes the components orthogonal to the signal at -85 °, which is the phase of the pure absorption signal from the calibration sample.

Looking at the absorption scan in Figure 6.5, we notice some interesting facts: the characteristic side peaks, due to the interference nature of the signal, are covered by the noise; besides, the FWHM of this scan is 1 mm, larger than the one in the calibration scan, which is 0.7 mm; also, the value of 3 ppm seems to be in disagreement with the value of less than 1 ppm measured at LMA. The absorption map in Figure 6.6 shows a very uniform absorption value of 3 ppm, according to the histogram, the standard deviation from the mean value is limited by the system noise. On the maps we also see many defects: there are 2 peaks of absorption per mm^2 that saturate the colorbar (above 5 ppm).

6.3.3 Discrepancy between LMA and NAOJ results

To explain the discrepancy between the absorption measurement at LMA and the absorption measurement at NAOJ, we have to consider that the AlGaAs coating

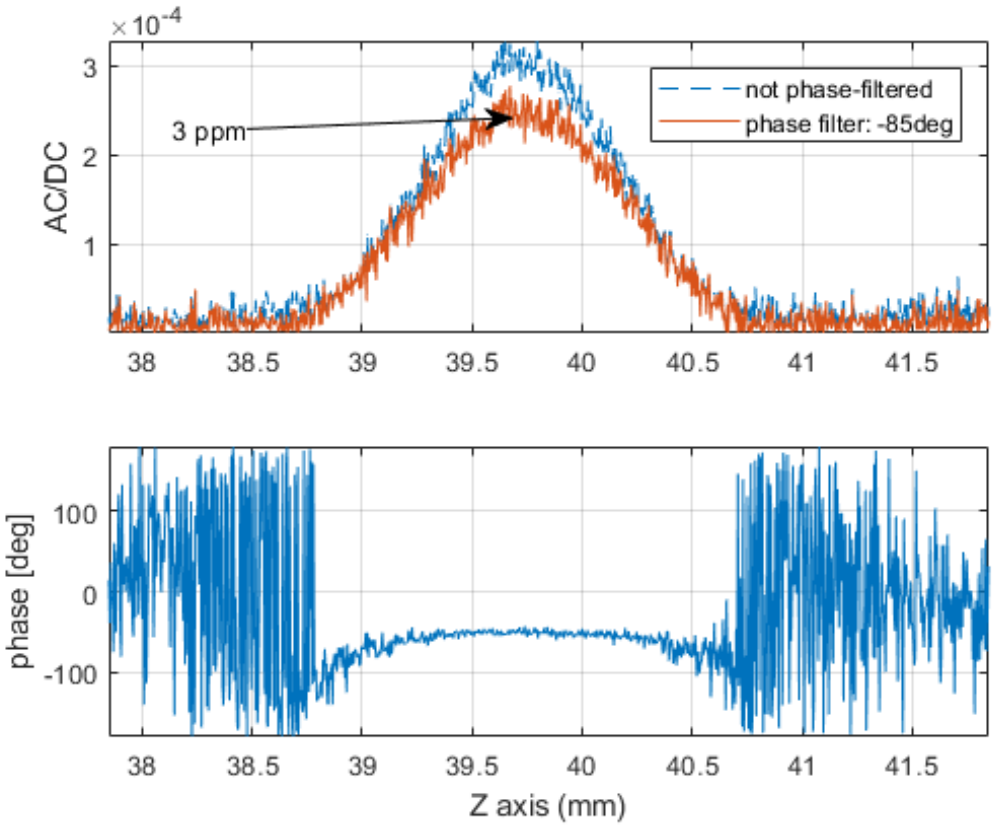

Figure 6.5: Scan along the sample depth of the crystalline coating transferred on a silica substrate. The measurement is done with a pump power of 10 W (after the chopper). The data is digitally filtered with an order 50 median filter and an order 50 average filter. The waiting time between two consecutive points is 5 s. The total acquisition time is 3 hours. The blue line is the AC/DC data with median and average filters only, while the red line is the AC/DC data with median, average, and phase filter at -85 °. The calibrated value is 3 ppm.

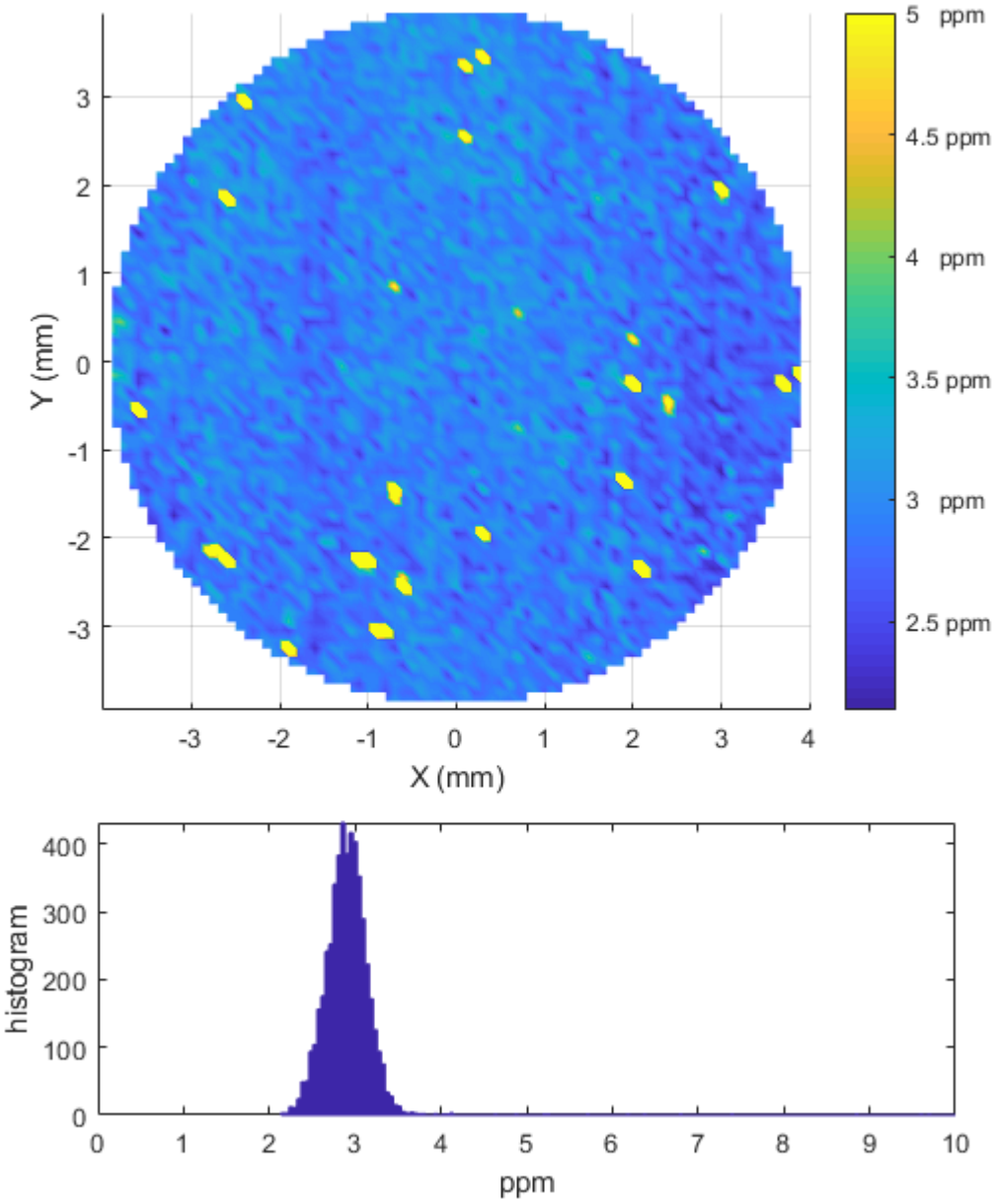

Figure 6.6: Absorption map around the center of the crystalline coating transferred on the fused silica substrate. The map is 8 mm in diameter and has a resolution of 100 µm. The data is digitally filtered with an order 50 median filter, an order 50 average filter, and a phase filter at -85 °. The waiting time between two consecutive points is 5 s. The total acquisition time is 9 hours. There are 23 peaks above 5 ppm, which means about 2 defects/mm^2. Apart from these peaks, the map is very uniform: on the bottom, the histogram shows a mean value of 3 ppm and an FWHM of 0.5 ppm, which is dominated by the noise of the system.

gives a non-negligible contribution to the absorption signal. Indeed, the coating thickness, 5.8 µm, is comparable with the thermal length in the silica substrate, $\sim$ 27 µm at 380 Hz. Also, the dn/dT of the coating, 366×10^{-6} for GaAs and 179×10^{-6} for AlGaAs, is more than one order of magnitude larger than the dn/dT of silica, 12.9×10^{-6}. In the reference sample, instead, the coating thickness is of the order of 10 nm, this means that the absorption signal is generated only in the substrate.

In the photo-deflection system at LMA, the pump beam is larger than the probe and the modulation frequency is smaller (210 Hz). In this conditions, the temperature penetrates more in the substrate, so the contribution from the coating is lower and the calibration is more accurate.

The diffusivity of GaAs, $31 \times 10^{-6}\,m^2/s$, is much larger than the fused silica, $0.84 \times 10^{-6}\,m^2/s$, this causes a wider temperature distribution along the coating surface with respect to the reference sample scan, which makes also the scan peak wider than in the reference sample scan.

We run the numerical simulations presented in Chapter 3, and compared the phase shift distribution on the AlGaAs coating and on a fused silica coating. In Figure 6.7 there is the result of this calculation. The wider distribution of the phase shift in the case of AlGaAs coating, explains the wider peak in the measured scan. According to SPTS there is also a thermal resistance in the interface between the coating and the substrate. This effect can't be included in our simulation, but can definitely cause the absorption value to be larger than the real one because it "traps" the heat inside the coating.

In order to verify this explanation experimentally, SPTS suggested calibrating the crystalline coating differently, without using any calibration sample. The SPTS company already uses this alternative method and it can also be done in our setup. The alternative calibration method uses the fact that the GaAs absorbs most of the visible light. So, by using a low power green pump laser with the same size as the 1064 pump, all the incident power is absorbed (except the Fresnel reflection) and the absorption signal will be the same as if the pump was at 1064 nm and partially absorbed. Knowing the green pump power we can calibrate the absorption. Then, changing back to the high power pump at 1064 nm we can measure the absorption without using the reference sample. The most important thing is to have exactly the same size for the two pumps, and also have a precise measurement of the pump power. The results from SPTS show a calibration factor of 3 which explains the discrepancy between the measurement at NAOJ and the measurement at LMA. We

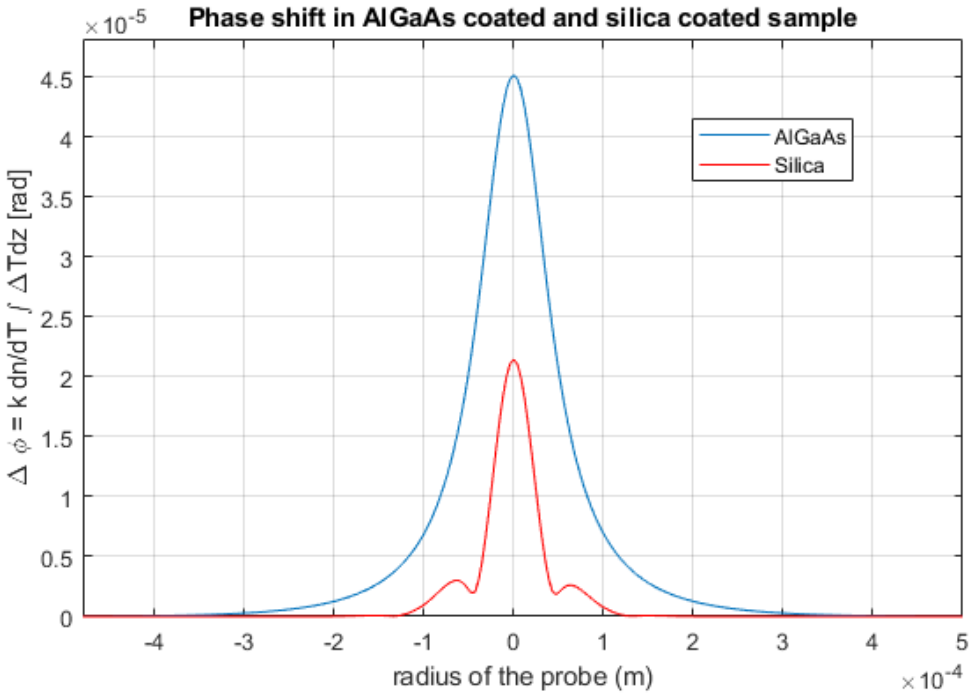

Figure 6.7: Phase shift distribution as a function of the radial distance from the center of the thermal lens. The contributions from the coating and from the substrate are added. The red line is the case of silica coating on silica substrate; the blue line is the case of AlGaAs coating (5.8 µm) on silica substrate. The phase shift of the AlGaAs coated sample is twice higher and twice wider than the case of silica.

are planning to do this alternative calibration on our setup.

6.4 Optical characterization measurements

In this section, we present the optical characterization measurements performed in collaboration with Laboratoire des Matériaux Avancés (LMA). The transmission spectra were made with a spectrophotometer located at the Advanced Technology Center in NAOJ. The single wavelength transmission measurement, the single point absorption measurement, the scattering maps and the roughness maps were done using experimental setups located at LMA. In this section, we describe these setups and present the measurement results on the crystalline coating samples.

6.4.1 Transmission

The transmission spectra of the two crystalline mirror samples are measured with a commercial spectrophotometer (SolidSpec-3700 [43]). The measured wavelength range spans from 890 to 1400 nm, with the resolution determined by the monochromator slit width. We chose 0.5 nm to have resolved spectrum peaks and a reasonable signal to noise ratio. We measure the transmission spectra, shown in Fig. 6.8, and compared it with calculated transmission curves based on a transmission matrix model. The amplitude of the oscillations is greater on the fused silica sample than the sapphire sample because of the larger difference in refractive index between the coating and the fused silica substrate. The transmission of the mirrors at 1064 nm was too low to be accurately measured by this spectrophotometer, so a 1064 nm laser and a detector were used to make this measurement. The transmission is 6 ppm for both substrates. This result is in very good agreement with the calculated transmission values. Note that the mirror stop bands of the two samples are slightly offset as each was produced in a separate growth run. As designed, these coatings have a nominal transmission of 9 ppm when transferred to a low-refractive-index substrate. Transmission matrix modeling shows that the lack of an AR coating on the backside of the silica and sapphire wafers yields the observed reduction in transmission to 7 ppm on fused silica and 6 ppm on sapphire due to the additional back-reflection from the substrate/air interface assuming constructive interference, yielding a reasonable match with the experimental values.

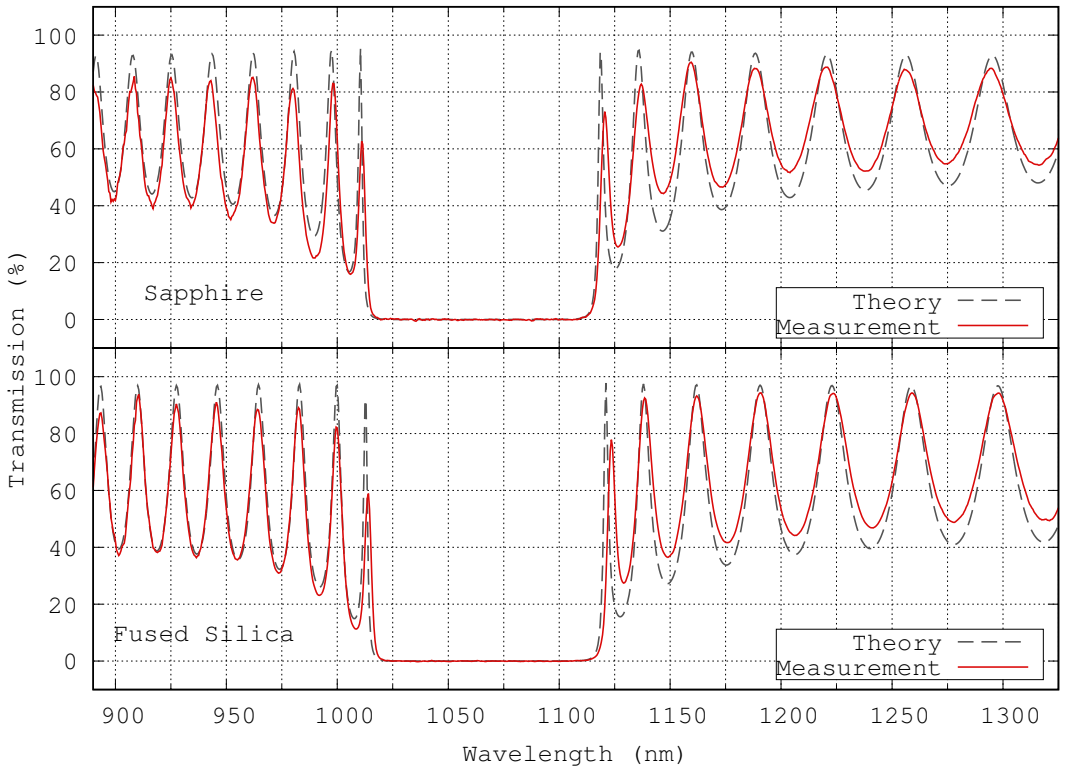

Figure 6.8: Transmission spectra of the two crystalline mirror samples measured via spectrophotometry. The measured and theoretical transmission spectra are in very good agreement as shown in the plots. The slight offset in the mirror stopbands is a consequence of the use of material from two separate crystal growth runs. Additionally, the satellite peaks show a variation in magnitude due to the different refractive indices of the substrates (fused silica n=1.449 and sapphire n=1.754 at 1064.0 nm).

6.4.2 Scattering

To measure the scattering at 1064 nm, we use a complete angle scatter instrument named CASI [38]. It is shown in Figure 6.11. In this setup, a 200 mW laser impinges on the mirror surface with an angle of 4°, then a photo-detector measures the scattering at 14° in the same plane of incidence. The PD is installed at 57 cm from the surface of the mirror, which means about 10 cm from the center of the reflected beam. This is the bidirectional reflectance distribution function (BRDF) value in sr^{-1} for those angles. A translation stage moves the sample in order to make a map of the scattering on the surface of the sample. The map resolution is 2 mm. In order to obtain the total integrated scattering (TIS) in ppm, the BRDF value should, in principle, be measured and integrated over all the scattering angles. Instead of doing this for each measurement, we employ a conversion curve. The conversion curve is

generated by scanning the scattering intensity as a function of the scattering angle in the plane of incidence (for a given incidence angle). Then a rotational symmetry around the reflected beam (outside the plane of incidence) is assumed so that the scattering can be easily integrated around the reflected beam. This assumption is true for low scattering optics. Fig. 6.9 shows the map of the BRDF scattering of the fused silica sample on a 30 mm-diameter area and Fig. 6.10 shows the map of the BRDF scattering of the sapphire sample on a 35-mm diameter area.

The TIS averages on the maps are 9.5 ppm for the fused silica sample and 6 ppm for the sapphire sample. These values are comparable with currently used amorphous coatings and match the requirements for application in current gravitational wave interferometers [25].

6.4.3 Roughness

As scattering is mainly driven by surface roughness, we further investigated the surface quality of the samples. The roughness was measured with a commercial optical profilometer (Micromap 550). It measures the surface height by using a Fizeau interferometer [44]. The experimental setup is shown in Figure 6.11. The resolution of the map is 1.28 µm and the size is 300 µm × 300 µm. Raw 2D data are processed by removing the tilt and the curvature in order to get rid of most of the distortions that may come from the instrument optics. To realize such corrections, the map matrix is expanded on the Zernike polynomials space, then the first components are subtracted from the map: the Z_0^0 component for the offset, $Z_1^{+1,-1}$ components for the tilt, the Z_2^0 component for the radius of curvature, and the $Z_2^{+2,-2}$ components for the astigmatism. A Power Spectrum Density (PSD) of the surface height is used to quantify the properties of the surface. Although a 2D Fourier transform is calculated from the 2D data,

$$C^{2D}_{q_x,q_y} = \frac{1}{L_x L_y}\left|\frac{1}{L_x L_y}\sum_{x,y} h_{x,y} e^{-i(q_x x + q_y y)}\right|^2 \tag{6.1}$$

where $h_{x,y}$ is the surface height and L_x and L_y are the map dimensions, a 1D plot summarizes the main features of the surface. In particular, assuming that the roughness is isotropic, an easier-to-read 1D PSD is calculated from the 2D Fourier

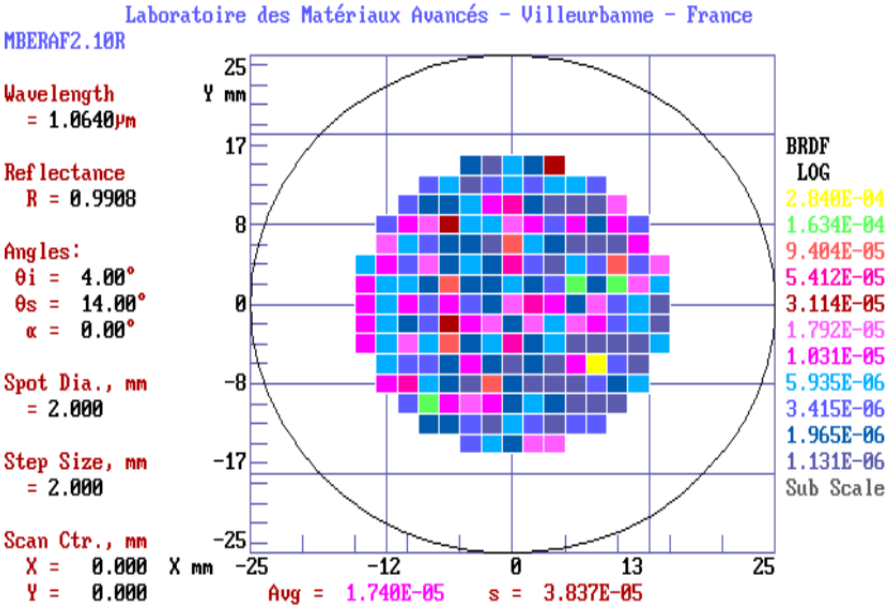

Figure 6.9: BRDF map of the coating on fused silica substrate. The average corresponds to 9.5 ppm.

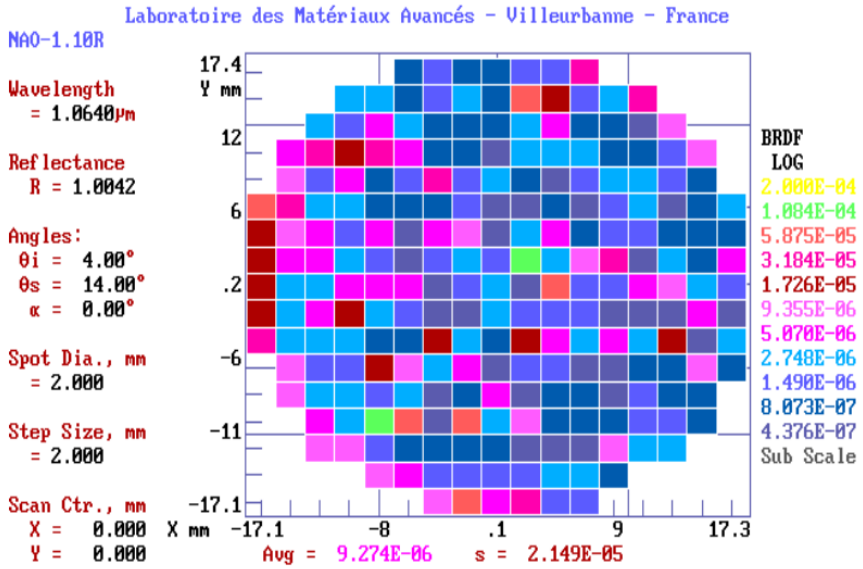

Figure 6.10: BRDF map of the coating on sapphire substrate. The average corresponds to 6 ppm.

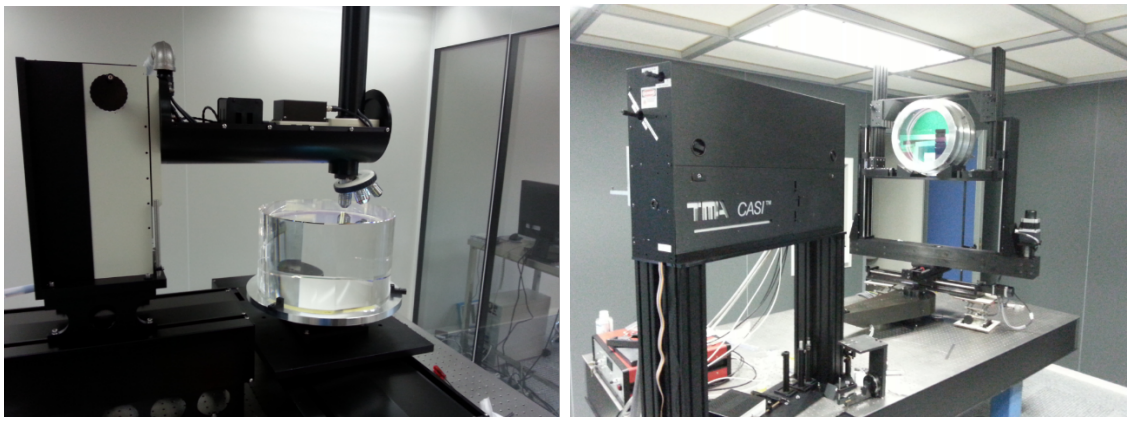

Figure 6.11: Photo of the experimental setups in LMA. On the left the scatterometer CASI. On the right the Micromap.

transform by averaging over all wavevectors where $|\vec{q}| = q$,

$$\mathrm{PSD}(q) = \frac{q}{2\pi^2} \int_0^{2\pi} C^{2D}(q\cos(\phi), q\sin(\phi))d\phi. \tag{6.2}$$

Finally the surface roughness is expressed as the root mean square (RMS) value, calculated as the standard deviation of the surface height or as the integral of the PSD [45, 46]. The roughness measurements are shown in Fig. 6.12 and the PSD is plotted in Fig. 6.13. The RMS roughness of the fused silica sample is 9.08 Å on substrate and 7.73 Å on coating, while for the sapphire sample it is 1.10 Å on the substrate and 1.08 Å on the coating. There is a difference of almost one order of magnitude between the coating roughness RMS of the fused silica sample and the sapphire sample. By looking at the PSD in Fig. 6.13, it can be seen that in general the roughness is limited by the substrate. Furthermore, we can notice that for the fused silica sample, at higher spatial frequencies, the coating roughness is lower than the one of the substrate. Also by looking at the maps in Fig. 6.12, it is clear that the coating on fused silica is smoother. A possible explanation of this is that in the case of fused silica, the coating does not perfectly follow the substrate surface roughness at short length-scales so that the final mirror roughness is determined by the smoother surface of the coating.

It is important to note that the employed substrates, both the fused silica and sapphire wafers, are not optimized for bonding given their non-ideal surface quality, both in terms of excess micro-roughness (in the case of fused silica) and imperfect surface figure (typically quoted as bow and warp in semiconductor parlance). The relatively large bow/warp figures of >10 µm are caused by polishing and internal

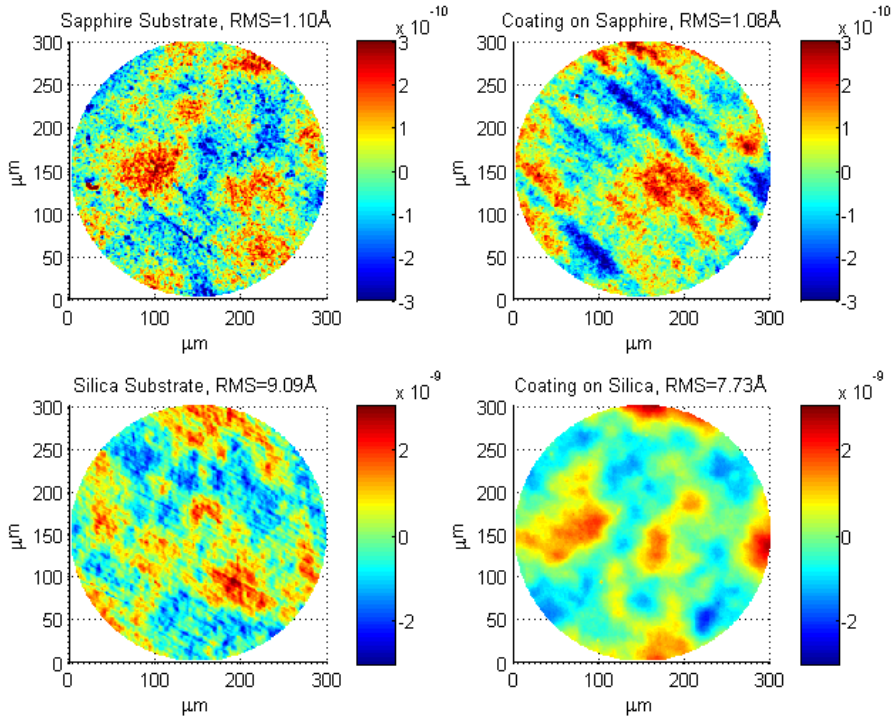

Figure 6.12: Roughness of the substrate and coating for both of the sapphire and fused silica samples. The roughness of the sapphire sample remains effectively unchanged after the coating process. For fused silica though, a significant flattening effect is visible.

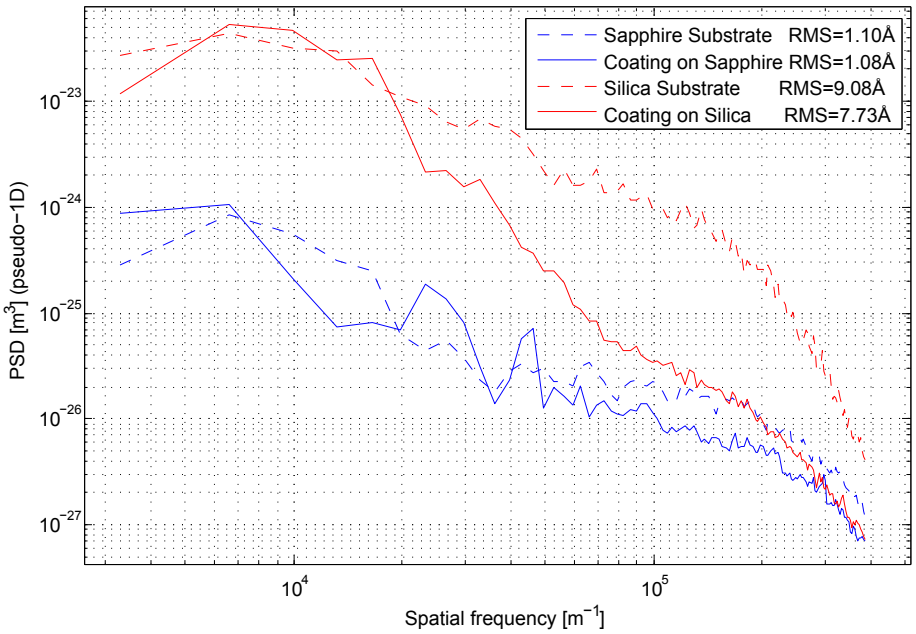

Figure 6.13: Roughness PSD of uncoated (dashed lines) and coated (solid lines) sapphire (blue lines) and fused silica (red lines) samples. In the case of fused silica, the original substrate roughness is more than one order of magnitude larger for length scales around 10 µm.

material stress, especially for the fused silica, of these thin wafers. Ultimately, the resulting non-ideal flatness drives many of the large defects in the samples due to non-uniform bond-wave propagation. Another driver for a subset of the defects is intrinsic/embedded defects in the epitaxial films themselves. Future tests would benefit from the use of high-quality bulk optical substrates with improved surface quality (micro-roughness and surface figure). The optical performances of the two crystalline coating samples are summarized in Table 6.1.

Measurement	**Coating on silica substrate**	**Coating on sapphire substrate**
Transmission @1064 nm	6 ppm	6 ppm
Scattering @1064 nm	9.5 ppm	6 ppm
Coating Roughness	7.7 Å RMS	1.1 Å RMS
Substrate Roughness	9.1 Å RMS	1.1 Å RMS

Table 6.1: Optical performances. Transmission and scattering are measured at 1064 nm. The roughness is measured on a 300 µm length-scale.

6.5 Thermal noise measurement

In the LIGO laboratory of the Massachusetts Institute of Technology (MIT), a new setup is able to measure directly the coating thermal noise. The article that presents the setup has been published recently [47]. We brought the crystalline coating samples described in the previous sections of this chapter to MIT to test them. In this section, we describe the experimental setup and how we measured the coating thermal noise of our samples.
Usually, the coating thermal noise estimation is made measuring the material parameters such as Young's modulus, Poisson's ratio, and the loss angle, and then putting the parameters in a model for the multilayer coating thermal noise. To get rid of the parameters uncertainties, a direct thermal noise measurement setup is needed. Several setups, that make use of free-space Fabry-Pérot suspended cavities, have been developed. But, since the readouts of these systems are in the transmission of the cavity, the sensitivity is limited by the reflectivity of the coatings. The novelty of the experimental setup developed at LIGO/MIT is that the sample is the folding mirror of a folded cavity, so there is no upper limit in the reflectivity of the measured coating.

6.5.1 Working principle

As explained in the first chapter, the Fluctuation-Dissipation Theorem relates the material mechanical dissipation to the surface position fluctuations, and the heat dissipation to temperature fluctuations. A laser beam reflected by a mirror experiences a phase noise due to the position fluctuations of the mirror's surface (Brownian noise) and to the temperature fluctuations (thermo-optic noise). The crucial point of this method is that different regions of the mirror surface generate uncorrelated phase noise. Provided two spatially different modes that resonate together in a Fabry-Pérot cavity, it is possible to suppress the common noises, so that the remaining noise is dominated by the mirror thermal noise.

There are three modes resonating in the folded cavity, the fundamental mode TEM00 and two second-order higher modes TEM02 and TEM20. The TEM00 is used to lock the cavity to the laser. The TEM02 and TEM20 are used to sense the coating thermal noise. In order to make the higher order modes resonate, the input beams are shifted in frequency by the spacing between modes according to

the formula for the higher modes resonance frequency

$$f_{nmq} = f_0 + q f_{\mathrm{FSR}} + (n+m)\delta f \tag{6.3}$$

where f_{FSR} is the free spectral range, n and m are the transverse mode indices, q is the axial mode number, and δf is the transverse mode spacing:

$$\delta f = -f_{\mathrm{FSR}} \frac{\phi_G}{2\pi} \tag{6.4}$$

where ϕ_G is the Gouy phase shift per round trip. The frequency shifted modes resonate as higher order modes inside the cavity. Since the cavity couplers have an imperfect radius of curvature, the two higher modes resonate at slightly different frequencies. The two higher modes are locked to the cavity with a control loop; a part of the injected beams is extracted and overlapped to generate a beat-note, which is demodulated using a reference signal at the frequency difference between the higher modes. The common noises such as table vibrations don't show up in the beat note, so the uncorrelated thermal noise of the folding mirror (i.e. the sample to test) dominates the spectrum of the beat-note and can be measured.

6.5.2 Experimental setup

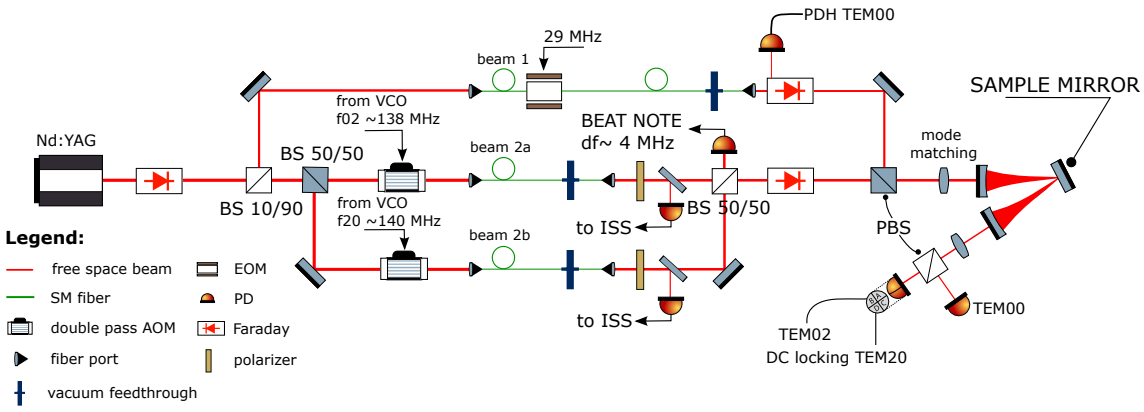

Figure 6.14: Diagram of the experimental setup. From the article that describes this setup [48].

The core of the experiment is the folded cavity where the folding mirror is the sample to test. The hole cavity is placed in a vacuum chamber to get rid of acoustic noise, wind, temperature fluctuations and other noises that may come from the air in the cavity. The coupling mirrors have a radius of curvature $R = 50\,\mathrm{mm}$ the cavity

nominal length is $L = 98\,\mathrm{mm}$. The folding angle is 17.23°. Given these parameters, the waist size ω_0, the free spectral range f_{FSR} and the transverse mode spacing f_{TMS} are

$$\omega_0 = \sqrt{\frac{\lambda\sqrt{L\epsilon}}{\pi}} \simeq 49\,\mu\mathrm{m} \tag{6.5}$$

$$f_{\mathrm{FSR}} = \frac{c}{2L} \simeq 1.53\,\mathrm{GHz} \tag{6.6}$$

$$f_{\mathrm{TMS}} = \frac{c}{\pi L}\sqrt{\frac{\epsilon}{R}} \simeq 144\,\mathrm{MHz} \tag{6.7}$$

where $\epsilon = R - L/2$.

Figure 6.15 shows the vacuum chamber and the folded cavity. The crystalline coating sample was too large to be mounted on a 1 inch mirror mount, so an adaptor made of peek plastic was made specially for this sample. The adaptor is inserted in the mirror mount to align it with. The laser source at 1064 nm is split into 3 beams, so that they all share the same frequency and intensity noise. One beam is used to lock the cavity. The beam reflected from the cavity is used to produce the Pound-Drever-Hall error signal [49] used in the control loop. Before entering the cavity, all the three beams are TEM00. To make the other two beams resonate as higher modes in the cavity, they are shifted in frequency using two double pass Acusto-Optic-Modulators. Since the frequency spacing between the TEM00 and the higher modes is around 288 MHz, the AOMs are controlled by two Marconi radio-frequency generators set at around 144 MHz. In order to be able to separate the TEM00 from the higher modes, the polarization of the higher modes beams is rotated by 90° with respect to the TEM00 beam polarization. The beams enter the cavity through optical single mode fibers. The polarization is controlled using fiber paddles which introduce the stress in fiber and rotate polarization to the desired orientation. Since these fibers are single mode they are very sensitive to technical noises so also intensity stabilization loops are needed to suppress polarization jitter before the cavity input.

In Figure 6.16 there are the resonant modes transmitted and detected by two cameras. The higher modes are locked to the cavity using two separate control loops. To make a Pound-Drever-Hall error signal for each of them, the two transmitted higher modes are detected separately using a quadrant-photo-detector. While the common noises are suppressed by the TEM00 control loop, the information of the thermal noise is contained in the control loops of the higher modes. The transmitted

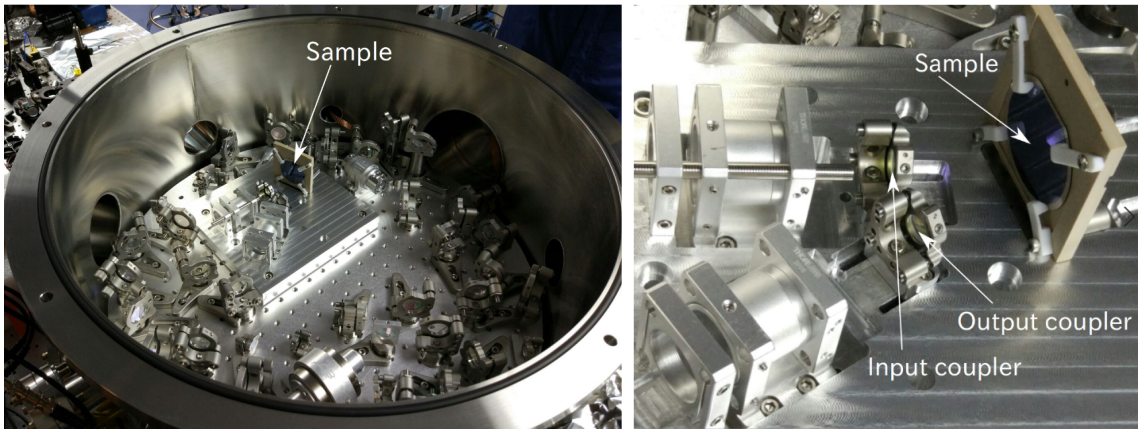

Figure 6.15: On the left, a picture of the vacuum chamber with the cavity inside. On the right, a picture of the cavity with the sample mounted on the peek adaptor.

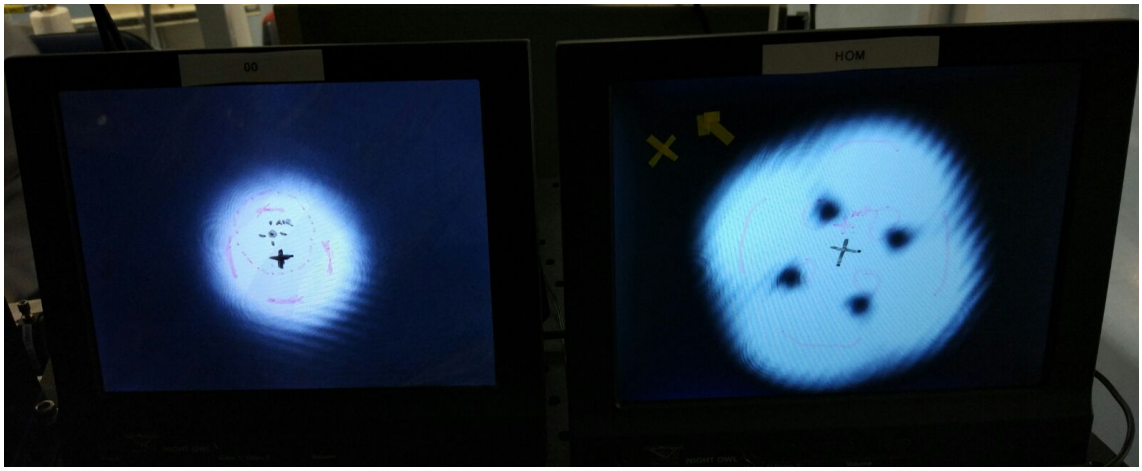

Figure 6.16: The display of the cameras that monitor the resonant modes. On the left the TEM00 and on the right the overlap of the TEM02 and TEM20. It is possible to separate the fundamental mode from the higher modes because they have perpendicular polarizations.

higher modes are therefore overlapped to make a beat note. The resonance frequencies of the two higher modes are slightly different because of the non-homogeneous radius of curvature of the couplers. The frequency difference is tuned to 5.4 MHz by rotating a coupler relatively to the other. The beat-note is demodulated at this frequency using a standard phase locked loop (PLL). A third Marconi generator is used as reference radio-frequency source. The PLL down-converts the beat to DC, and the residual phase noise is the final measurement of coating thermal noise.

6.5.3 Noises

Provided the common noise suppression, the demodulation output of the beat-note shows the sum of several noise contributions. A summary of the noise sources follows:

- The mechanical vibrations of the parts in the cavity are mostly suppressed by the TEM00 control loop, but some residual coupling with the cavity length is due to the different frequency of the higher modes and to the backscattering of the sample. The motion of the coupling mirrors also causes longitudinal motion that make phase fluctuations and power fluctuation.

- Photo-thermal noise is caused by power fluctuations inside the cavity. When the temperature of the coating changes, the thermal expansion makes the power fluctuations couple to the cavity length.

- The radio frequency (rf) oscillators used to drive the acousto-optic modulators and for the control loops, have frequency noise. Due to the finite bandwidth of the control loops, this noise is amplified at higher frequencies. The effect on the beat-note is above 200 Hz, where the noise floor rises toward the unity gain frequency of the higher order modes control loops.

- A large part of the white noise floor is the photons shot noise, which is unavoidable. Another part is explained by the down-conversion process: higher frequencies fluctuations, due to the imbalance of the cavity poles of the higher order modes, are down-converted to the audio-band through the non-linear demodulations used to produce the PDH signal.

Further details on these noises are in the article by S.Gras et al. [47].

6.5.4 Results

The result of the measurement is plotted in Figure 6.17. There are the spectra of the beat-note between the high-order modes, that gives the information of the thermal noise. Comparing the thermal noise of the aLIGO amorphous coating on fused silica substrate, and the AlGaAs crystalline coating on fused silica substrate, we see that the crystalline coating gives a thermal noise which is a factor of ∼2 lower than the amorphous coating.

The conversion from Volts to meters is taken in two steps. First, Volts are converted to Hz, this is the direct conversion using the modulation value of the PLL loop. The third Marconi is set to 282 Hz/V. The conversion from Hz to meters comes from the cavity length measurement, $d\nu/\nu = dL/L$, where L is the cavity length and ν is the laser light frequency.

We also measured the cavity pole of the higher modes by changing the Marconi's frequency until the transmitted power was half of the maximum. In Table 6.2 there are the measurements of the cavity poles for each high order mode in the case of the fused silica sample.

	Power (V)	Marconi (MHz)	Cavity pole (kHz)
Mode A	0.843	144.080840	
	0.4215	144.06159	39.5
Mode B	0.846	142.008050	
	0.4230	142.023800	31.5

Table 6.2: Fused silica sample cavity pole measurements. Naming the higher modes TEM02 or TEM20 depends on the choise of coordinates, so we call them Moda A and Mode B.

Notice that mode A and B have different cavity poles. Common mode rejection in this case is not ideal and can result in bad frequency noise rejection at high frequency. This may explain the large noise at higher frequencies in the plot in Figure 6.17. According to the cavity parameters, the nominal cavity pole is 20 kHz. We measured the cavity pole for SiO_2 and Al_2O_3 substrates to be 39 kHz and 26 kHz, respectively. Both cavities show similar high-frequency noise. So the high-frequency noise is not entirely clear to be caused by the low finesse of the cavity.

Looking at the plot in Figure 6.17, it's easy to notice that the sample with crystalline coating on fused silica makes lower noise than the one on sapphire substrate. Assuming that the same crystalline coating on the two substrates makes the same coating thermal noise, the difference has to be explained by the contribution coming

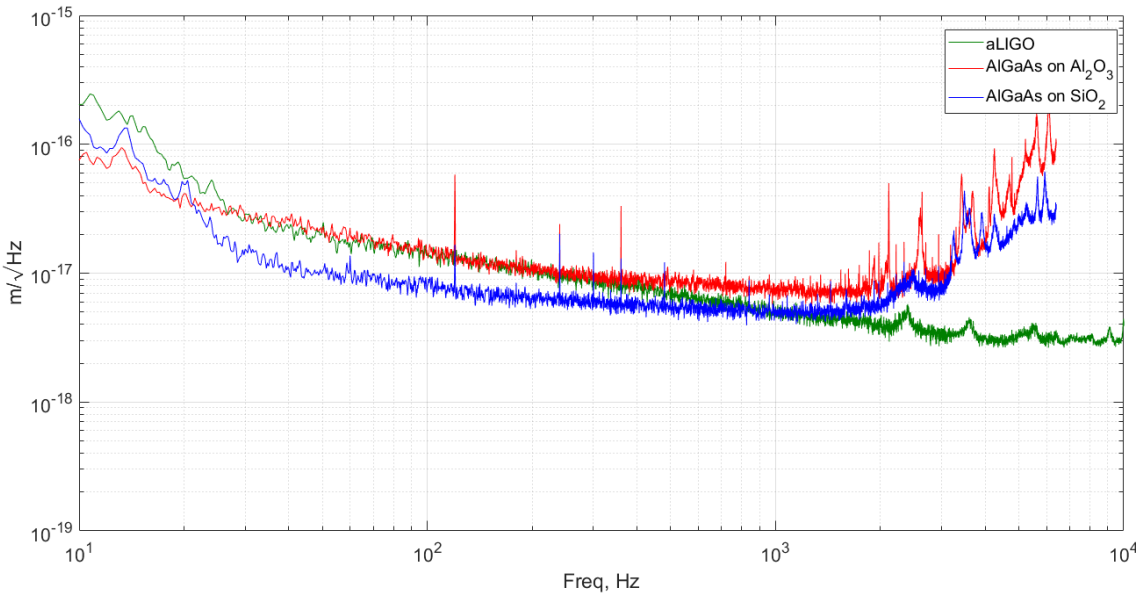

Figure 6.17: Beat-note spectra for 3 samples at room temperature: AlGaAs crystalline coating on fused silica substrate (in blue) and on sapphire substrate (in red); aLIGO amorphous coating on silica substrate (in green), previously measured with the same setup. At lower frequencies, the seismic noise dominates. At higher frequencies, the electronic noise dominates. The most sensitive spectrum region for the coating thermal noise is between 20 Hz and 1 kHz. The great result of these measurements is that the thermal noise of the AlGaAs crystalline coating on silica (in blue) is about a factor of 2 lower than the thermal noise of the amorphous coating used in Advanced LIGO (in green). The substrate of the Advanced LIGO mirrors are made of fused silica as well, so the noise contribution from the substrate is the same, so we assume that the difference between the green and the blue line comes only from the coatings. On the other hand, we have a crystalline AlGaAs coating transferred on sapphire substrate (in red) that gives a noise higher than the one transferred on the silica substrate (in blue), and comparable with the amorphous coating deposited on fused silica (in green). Since this measurement system can't discriminate the noise contribution of the substrate from the one of the coating, we believe that this difference comes from the substrate thermo-elastic noise. With this setup, there is not a direct thermal noise measurement of Advanced LIGO amorphous coating deposited on a sapphire substrate yet, but in that case, we expect this kind of measurement to give a larger value than both the green and the red curves. At cryogenic temperature, instead, we expect the sapphire substrate noise not to limit the thermal noise measurement anymore. For a detailed explanation, see the text.

from the substrate.

The main contribution from the substrate is the thermo-elastic noise, that depends on the coefficient of thermal expansion. At room temperature (i.e. our experimental conditions), a sapphire substrate has a thermo-elastic noise larger than a silica substrate, due to a factor of 10 larger coefficient of thermal expansion, see Table 6.3.

Material	Fused silica	Sapphire
Thermal expansion at 300 K	$0.51 \times 10^{-6}\,\mathrm{K}^{-1}$	$5.1 \times 10^{-6}\,\mathrm{K}^{-1}$
Thermal expansion at 20 K	$-0.25 \times 10^{-6}\,\mathrm{K}^{-1}$	$5.3 \times 10^{-10}\,\mathrm{K}^{-1}$

Table 6.3: Thermal expansion coefficient of fused silica and sapphire at room temperature and cryogenic temperature. The coefficient for sapphire drops by 4 orders of magnitude when going at cryogenic temperature.

These measurements are done at room temperature (T$\simeq$300 K), but the sapphire samples are designed to work at cryogenic temperature (T$\simeq$20 K), where fused silica can't be used for its bad thermal conductivity. Although there is not a direct measurement of thermal noise at cryogenic temperature yet, the sapphire's thermal expansion coefficient at cryogenic temperature is 4 orders of magnitude lower than at room temperature (see Table 6.3), therefore, the thermo-elastic noise from the substrate is expected not to be limiting the thermal noise measurement.

Moreover, the crystalline coating has a lower mechanical losses at cryogenic temperature, one order of magnitude, which will also contribute to the reduction of coating thermal noise.

6.5.5 Future plan for the estimation of coating thermal noise

The measurement of coating thermal noise in this setup does not distinguish the coating noise from the substrate noise. For a better understanding of the various contributions, and to be able to fit the data showed in the previous subsection, some calculation is needed. In this subsection, we explain our plan for a future investigation about the difference between the measured thermal noise of the coating on silica and on sapphire.

The estimation of thermo-optic noise (reminding that it is the combination of thermo-elastic and thermo-refractive noises) can be done using the formulas explained in the article [50].

The direct approach consists in applying the Fluctuation-Dissipation Theorem

as in Levin's derivation [51]. As already explained in Chapter 1, the temperature fluctuations δT are related to heat flow dissipation W. The procedure is to calculate the dissipated power (by heat flow) caused by an oscillating power injection in a small volume δV located at $\vec{r}$:

$$\frac{P}{\delta V} = TF_0 \sin(\omega t) q(\vec{r}) \tag{6.8}$$

where F_0 is a scale factor that will cancel out later, ω is the frequency at which we want to calculate the noise, and $q(\vec{r})$ is the form factor. The form factor $q(\vec{r})$ is of crucial importance because it contains the information about how the temperature fluctuations affect the reflected beam. In other words, the measurement variable $\hat{z}$ is connected to the mirror temperature fluctuations δT via

$$\hat{z} = \int \delta T(\vec{r}, t) q(\vec{r}) d^3 r \tag{6.9}$$

where the integral is over all space. Once the heat equation is solved, the power injection leads to the heat flow (therefore dissipation), that can be expressed as

$$W = \left\langle \int \frac{\kappa}{T} (\vec{\nabla} \delta T)^2 \right\rangle \tag{6.10}$$

where the average is over cycles of the oscillating power injection.
Then, the noise for $\hat{z}$ is calculated as

$$S^{\hat{z}} = \frac{8 k_B T W}{F_0^2} \tag{6.11}$$

To calculate the form factor $q(\vec{r})$ in the case of mirrors used in interferometric gravitational wave detectors, some approximations can be used. The beam size is very large (order of few cm) compared to the coating thickness (order of few µm) and also very large compared to the thermal diffusion length:

$$r_T = \sqrt{\frac{\kappa}{C\omega}} \tag{6.12}$$

which is of the order of ∼100 µm for silica at $\omega = 2\pi 100$ Hz. Because of the large beam size, in the calculation presented in [50], the heat flow is only directed toward the substrate, so the diffusion in the transverse dimensions is ignored. In this experimental setup, such approximations are no longer valid because the beam size is very small, ∼50 µm, same order of the thermal diffusion length, and only ∼10 times larger than the coating thickness.

In literature, most of the analytic calculations of thermal noises are based on the TEM00 shape for the impinging beam. But in this experiment, the noise is sensed by high order modes. In particular, the readout is the difference between the two higher modes TEM02 and TEM20. Therefore, the heat flow between the two regions impinged by the two modes can't be neglected.

For these reasons, it is convenient to calculate the form factor $q(\vec{r})$ and the heat flow W using a Finite Element Method (FEM) software. A similar calculation is reported in the first article that describes this experiment [47]. In that case, the FEM analysis was a calculation of strain and stress in the coating, in order to calculate the correction factor between the Brownian noise sensed by the TEM00 and the one sensed by the TEM02/20. In the case of thermo-optic noise, the dissipation mechanism is different, so the approach is different.

To calculate the form factor we have to take into account the thermal expansion (thermo-elastic) and the refractive index change (thermo-refractive). In general, the form factor $q(\vec{r})$ evaluated at a certain position $\vec{r}_0$ is the effect of a small temperature change of a small volume around $\vec{r}_0$ on the reflected beam phase. Let's say that it is the derivative:

$$q(\vec{r}_0) = \frac{\partial \hat{z}}{\partial T(\vec{r}_0)} \tag{6.13}$$

The temperature change $\Delta T(z_0)$ of a small volume at depth z_0 generates thermal expansion in the whole volume, therefore a bump on the surface. It also generates a refractive index change in the small volume according to the dn/dT. These two effects are included in the phase shift $\Delta\phi^{z_0}(x, y)$ that the reflected beam experiences.

The form factor layer at depth z_0 is the convolution between the phase shift map and the intensity of the beam:

$$q(z_0, x, y) = \int\int \Delta\phi^{z_0}(u - x, v - y) I_{02\text{-}20}(u, v) du dv \tag{6.14}$$

where $I_{02\text{-}20}(x, y)$ is the shape of the beam at the surface. In the case of this experiment the shape is the overlap of the TEM02 and TEM20 modes with opposite sign

because the readout is the difference of the two modes:

$$I_{02\text{-}20}(x,y) = \left[H_0\left(\frac{\sqrt{2}x}{w_0}\right) e^{-\frac{x^2}{w^2}} H_2\left(\frac{\sqrt{2}y}{w_0}\right) e^{-\frac{y^2}{w^2}} \right]^2 + \tag{6.15}$$

$$- \left[H_2\left(\frac{\sqrt{2}x}{w_0}\right) e^{-\frac{x^2}{w^2}} H_0\left(\frac{\sqrt{2}y}{w_0}\right) e^{-\frac{y^2}{w^2}} \right]^2 = \tag{6.16}$$

$$= e^{-\frac{2x^2}{w^2}} e^{-\frac{2y^2}{w^2}} \left[\left(\frac{8y^2}{w^2} - 2\right)^2 - \left(\frac{8x^2}{w^2} - 2\right)^2 \right] \tag{6.17}$$

where H_k are the Hermite polynomials and w is the beam size at the mirror surface.

Using a FEM software, we will calculate the phase shift and the form factor for a small volume at depth z_0, and then repeat for all the depths to finally get the whole form factor $q(\vec{r})$.
Then, in another FEM simulation, we will solve the heat equation with the injected power in Equation 6.8 for each frequency ω, calculate the heat flow using Equation 6.10, and finally put it in Equation 6.11 to get the thermo-optic noise.

To control the correctness of the simulations, we will use a large TEM00 beam shape and compare the results with the analytic formulas.

6.6 Conclusion

These results, in particular the measured absorption of the order of 1 ppm and the measured large-area scattering losses below 10 ppm, are remarkable. The direct measurements that we did at MIT confirm that these coatings have better thermal noise than the amorphous coatings currently employed by LIGO and Virgo.We find that substrate-transferred crystalline coatings are a promising alternative to ion-beam sputtered amorphous coatings for applications in precision interferometry, and in particular for KAGRA.

Future efforts will focus on continued improvements in the manufacturing process for increasingly larger coating areas, with a major focus on reducing the density of large defects at the bond interface. The absorption map done with the PCI setup developed in this thesis and the defects counting show that the number of defects is higher than the current mirrors employed in LIGO and Virgo. In order to apply these coatings on gravitational wave detector test masses, the number of defects needs to be decreased, and, even more importantly, the size of the optics must be increased. The crystalline coating technology is admittedly new, but is

maturing extremely rapidly, primarily driven by efforts relating to the development of ultrastable cavities for metrology (optical atomic clocks and inertial navigation being key drivers). For cm-scale coatings, the yield is now excellent [41]. Employing high-quality epitaxial films together with super-polished substrates we can reach manufacturing yields of nearly 100% for defect-free bonded coatings. As the coating size increases, the process becomes challenging, but we are confident that similar yields can be achieved with dedicated tooling. Interestingly, upon initial contact, the coating is bonded by Van der Waals forces only and can be removed if the defect density doesn't meet the requirements. Only after a modest anneal (temperatures on the order of 100 °C) will the bond be permanently fused. Thus, critical substrates will not be destroyed by poor initial contact.These initial results on roughly 5-cm diameter coatings motivate us to continue developing this novel low-noise coating technology.

Conclusions

KAGRA will be the first km-scale laser interferometer gravitational wave detector to be operated at cryogenic temperature with the goal to reduce thermal noise. Two effects limit the reduction of the thermal noise that KAGRA can achieve. On one side the absorption of light in the sapphire composing the mirror substrate requires the cryogenic system to remove of the order of 1 W of heat from the mirror. This imposes to use thick fibers to suspend the mirrors thus limiting the reduction of the pendulum thermal noise. On the other side, the reduction of the mirror thermal noise is limited by the size of the beam in the interferometer, the latter being limited by the size of the sapphire mirror. Moreover, the internal friction in the amorphous coatings used for the mirror does not improve (according to some measurements it degrades) thus limiting the reduction of the mirror thermal noise. For the reasons described above it is essential to develop larger sapphire crystals with lower optical absorption and to look for coatings with low optical absorption and lower internal mechanical losses at low temperatures. In this thesis, we developed and tested an optical absorption measurement system based on the so-called Photo-thermal Common-path Interferometer (PCI) technique. The setup initial configuration was developed by the SPTS company. We did numerical simulations where we modeled the readout of the experimental setup. The simulations output are in good agreement with the experimental results. It helped us in deeply understanding the details of the setup, optimizing the parameters, and get the best absorption signal. We further improved the setup by designing, assembling and testing an upgraded version of the system that is able to measure large KAGRA mirrors (22 cm in diameter and 15 cm in thickness). We performed the alignment optimization, the responsivity maximization, and the noise reduction. The sensitivity of our setup on sapphire bulks is better than 2 ppm/cm. We tested some sapphire substrates and compared the results with the SPTS laboratory to confirm and validate the calibration. The results are compliant with SPTS within 20%. We made maps and studied the absorption of several the sapphire substrates. In particular, we measured the

3D absorption map inside a KAGRA substrate. We found very interesting absorption structures in the substrate. We could recognize the crystal growth axis and direction. Since the absorption is mainly due to the crystal structure dislocations and it's strongly related to the growth method, sharing this results with the crystal maker will contribute to further improvements in the fabrication process.

We characterized the optical performance of the first large-area (5 cm diameter) crystalline coatings in collaboration with CMS and CNRS/LMA. The results of this characterization were published in the paper "Optical performance of large-area crystalline coatings" on Optics Express [2]. We measure the absorption at CNRS/LMA and found a value below 1 ppm. To measure the absorption with our PCI setup we assembled and tested an additional infrared probe, reaching a precision better than 0.2 ppm. This sensitivity was enough to see a clear absorption signal of 3 ppm in the crystalline coating. A discrepancy appears between our value and the LMA one, but it is explained by SPTS that noticed an important contribution from the coating, and a thermal resistance of the interface between the coating and the substrate, that can give the observed factor of 3 in the calibration. We run some simulations and confirmed that the different thermal properties between the crystalline coatings and the calibration sample affect the result. To experimentally confirm and solve the discrepancy, the plan is to calibrate the crystalline coating independently using a pump that is completely absorbed in GaAs.

In collaboration with CNRS/LMA, we also measured transmission, defects number, scattering maps, roughness. The coatings show excellent optical performances. We did a direct measurement of the crystalline coating thermal noise at MIT that confirms that these coatings have better thermal noise than the amorphous coatings currently employed by LIGO and Virgo. Further investigation is needed to understand the contributions from thermo-elastic and thermo-refractive noise. Future efforts will focus on continued improvements in the manufacturing process for increasingly larger coating areas, with a major focus on reducing the density of large defects at the bond interface.

Bibliography

[1] B.P. Abbott et al. (LIGO Scientific Collaboration and Virgo Collaboration). Observation of Gravitational Waves from a Binary Black Hole Merger. *Physical Review Letters*, 116(6):061102, 2 2016.

[2] Manuel Marchiò, Raffaele Flaminio, Laurent Pinard, Daniéle Forest, Christoph Deutsch, Paula Heu, David Follman, and Garrett D. Cole. Optical performance of large-area crystalline coatings. *Optics Express*, 26(5):6114–6125, 3 2018.

[3] E Müller. Gravitational radiation from core-collapse supernovae. *Classical and Quantum Gravity*, 14(6):010, 6 1997.

[4] Peter R. Saulson. *Fundamentals of interferometric gravitational wave detectors*. World Scientific, 1994.

[5] Eleonora Capocasa, Yuefan Guo, Marc Eisenmann, Yuhang Zhao, Akihiro Tomura, Koji Arai, Yoichi Aso, Manuel Marchiò, Laurent Pinard, Pierre Prat, Kentaro Somiya, Roman Schnabel, Matteo Tacca, Ryutaro Takahashi, Daisuke Tatsumi, Matteo Leonardi, Matteo Barsuglia, and Raffaele Flaminio. Measurement of optical losses in a high-finesse 300 m filter cavity for broadband quantum noise reduction in gravitational-wave detectors. *Physical Review D*, 98(2):022010, 7 2018.

[6] Peter R. Saulson. Terrestrial gravitational noise on a gravitational wave antenna. *Physical Review D*, 30(4):732–736, 8 1984.

[7] Herbert B. Callen and Richard F. Greene. On a Theorem of Irreversible Thermodynamics. *Physical Review*, 86(5):702–710, 6 1952.

[8] A. Gillespie and F. Raab. Thermally excited vibrations of the mirrors of laser interferometer gravitational-wave detectors. *Physical Review D*, 52(2):577–585, 7 1995.

[9] Yu. Levin. Internal thermal noise in the LIGO test masses: A direct approach. *Physical Review D*, 57(2):659–663, 1 1998.

[10] V.B. Braginsky, M.L. Gorodetsky, and S.P. Vyatchanin. Thermodynamical fluctuations and photo-thermal shot noise in gravitational wave antennae. *Physics Letters A*, 264(1):1–10, 12 1999.

[11] Bruin Benthem and Yuri Levin. Thermorefractive and thermochemical noise in the beamsplitter of the GEO600 gravitational-wave interferometer. *Physical Review D*, 80(6):062004, 9 2009.

[12] Gregory M Harry, Andri M Gretarsson, Peter R Saulson, Scott E Kittelberger, Steven D Penn, William J Startin, Sheila Rowan, Martin M Fejer, D R M Crooks, Gianpietro Cagnoli, Jim Hough, and Norio Nakagawa. Thermal noise in interferometric gravitational wave detectors due to dielectric optical coatings. *Classical and Quantum Gravity*, 19(5):897–917, 3 2002.

[13] Rana X. Adhikari. Gravitational radiation detection with laser interferometry. *Reviews of Modern Physics*, 86(1):121–151, 2 2014.

[14] The LIGO Scientific Collaboration and the Virgo Collaboration. GWTC-1: A Gravitational-Wave Transient Catalog of Compact Binary Mergers Observed by LIGO and Virgo during the First and Second Observing Runs. *arXiv e-prints*, November 2018.

[15] I. Andreoni, K. Ackley, J. Cooke, A. Acharyya, J. R. Allison, G. E. Anderson, M. C. B. Ashley, D. Baade, M. Bailes, K. Bannister, A. Beardsley, M. S. Bessell, F. Bian, P. A. Bland, M. Boer, T. Booler, A. Brandeker, I. S. Brown, D. A. H. Buckley, S.-W. Chang, D. M. Coward, S. Crawford, H. Crisp, B. Crosse, A. Cucchiara, M. Cupák, J. S. de Gois, A. Deller, H. A. R. Devillepoix, D. Dobie, E. Elmer, D. Emrich, W. Farah, T. J. Farrell, T. Franzen, B. M. Gaensler, D. K. Galloway, B. Gendre, T. Giblin, A. Goobar, J. Green, P. J. Hancock, B. A. D. Hartig, E. J. Howell, L. Horsley, A. Hotan, R. M. Howie, L. Hu, Y. Hu, C. W. James, S. Johnston, M. Johnston-Hollitt, D. L. Kaplan, M. Kasliwal, E. F. Keane, D. Kenney, A. Klotz, R. Lau, R. Laugier, E. Lenc, X. Li, E. Liang, C. Lidman, L. C. Luvaul, C. Lynch, B. Ma, D. Macpherson, J. Mao, D. E. McClelland, C. McCully, A. Möller, M. F. Morales, D. Morris, T. Murphy, K. Noysena, C. A. Onken, N. B. Orange, S. Osłowski, D. Pallot,

J. Paxman, S. B. Potter, T. Pritchard, W. Raja, R. Ridden-Harper, E. Romero-Colmenero, E. M. Sadler, E. K. Sansom, R. A. Scalzo, B. P. Schmidt, S. M. Scott, N. Seghouani, Z. Shang, R. M. Shannon, L. Shao, M. M. Shara, R. Sharp, M. Sokolowski, J. Sollerman, J. Staff, K. Steele, T. Sun, N. B. Suntzeff, C. Tao, S. Tingay, M. C. Towner, P. Thierry, C. Trott, B. E. Tucker, P. Väisänen, V. Venkatraman Krishnan, M. Walker, L. Wang, X. Wang, R. Wayth, M. Whiting, A. Williams, T. Williams, C. Wolf, C. Wu, X. Wu, J. Yang, X. Yuan, H. Zhang, J. Zhou, and H. Zovaro. Follow Up of GW170817 and Its Electromagnetic Counterpart by Australian-Led Observing Programmes. *Publications of the Astronomical Society of Australia*, 34:e069, 12 2017.

[16] The LIGO Scientific Collaboration. Advanced LIGO. *Classical and Quantum Gravity*, 32(7):74001, 2015.

[17] The VIRGO Collaboration. Advanced Virgo: a second-generation interferometric gravitational wave detector. *Classical and Quantum Gravity*, 32(2):24001, 2015.

[18] Yoichi Aso, Yuta Michimura, Kentaro Somiya, Masaki Ando, Osamu Miyakawa, Takanori Sekiguchi, Daisuke Tatsumi, and Hiroaki Yamamoto. Interferometer design of the KAGRA gravitational wave detector. *Phys. Rev. D*, 88(4):43007, 2013.

[19] Muzammil A. Arain and Guido Mueller. Design of the Advanced LIGO recycling cavities. *Optics Express*, 16(14):10018, 7 2008.

[20] Raffaele Flaminio and KAGRA collaboration. The cryogenic challenge: status of the KAGRA project. *Journal of Physics: Conference Series*, 716(1):012034, 5 2016.

[21] bKAGRA Sensitivity Curve. https://gwcenter.icrr.u-tokyo.ac.jp/en/researcher/parameter.

[22] T. Akutsu et al. The status of KAGRA underground cryogenic gravitational wave telescope. In *15th International Conference on Topics in Astroparticle and Underground Physics (TAUP 2017) Sudbury, Ontario, Canada, July 24-28, 2017*, 2017.

[23] Chen Dan. *Study of a cryogenic suspension system for the gravitational wave telescope KAGRA*. PhD thesis, The University of Tokyo, 2015.

[24] Kentaro Somiya. Detector configuration of KAGRA-the Japanese cryogenic gravitational-wave detector. *Classical and Quantum Gravity*, 29(12):124007, 6 2012.

[25] L. Pinard, C. Michel, B. Sassolas, L. Balzarini, J. Degallaix, V. Dolique, R. Flaminio, D. Forest, M. Granata, B. Lagrange, N. Straniero, J. Teillon, and G. Cagnoli. Mirrors used in the LIGO interferometers for first detection of gravitational waves. *Applied Optics*, 56(4):C11, 2 2017.

[26] R Flaminio, J Franc, C Michel, N Morgado, L Pinard, and B Sassolas. A study of coating mechanical and optical losses in view of reducing mirror thermal noise in gravitational wave detectors. *Classical and Quantum Gravity*, 27(8):084030, 4 2010.

[27] Garrett D. Cole, Wei Zhang, Michael J. Martin, Jun Ye, and Markus Aspelmeyer. Tenfold reduction of Brownian noise in high-reflectivity optical coatings. *Nature Photonics*, 7(8):644–650, 8 2013.

[28] Garrett D. Cole. Cavity optomechanics with low-noise crystalline mirrors. In Kishan Dholakia and Gabriel C. Spalding, editors, *Optical Trapping and Optical Micromanipulation IX*, volume 8458, page 845807. International Society for Optics and Photonics, 10 2012.

[29] The LIGO Scientific Collaboration, the Virgo Collaboration, J. Abadie, B. P. Abbott, R. Abbott, M Abernathy, T. Accadia, F. Acernese, C. Adams, R. Adhikari, and et al. Sensitivity to Gravitational Waves from Compact Binary Coalescences Achieved during LIGO's Fifth and Virgo's First Science Run. *arXiv e-prints*, March 2010.

[30] "T-NA Series Linear Actuator User's Manual". https://www.zaber.com/wiki/Manuals/T-NA.

[31] W. B. Jackson, N. M. Amer, A. C. Boccara, and D. Fournier. Photothermal deflection spectroscopy and detection. *Applied Optics*, 20(8):1333, 4 1981.

[32] "OSCAR: An optical FFT code to simulate Fabry Perot cavities with arbitrary mirror profiles". https://it.mathworks.com/matlabcentral/fileexchange/20607-oscar.

[33] "Software/Zaber Console". https://www.zaber.com/wiki/Software/Zaber_Console.

[34] Peter R. Saulson. Thermal noise in mechanical experiments. *Physical Review D*, 42(8):2437–2445, 10 1990.

[35] Massimo Granata, Emeline Saracco, Nazario Morgado, Alix Cajgfinger, Gianpietro Cagnoli, Jérôme Degallaix, Vincent Dolique, Danièle Forest, Janyce Franc, Christophe Michel, Laurent Pinard, and Raffaele Flaminio. Mechanical loss in state-of-the-art amorphous optical coatings. *Physical Review D*, 93(1):012007, 1 2016.

[36] G. D. Cole, P. Heu, D. Follman (CMS LLC), C. Deutsch, T. Zederbauer, and C. Pawlu (CMS GmbH). Cms inspection report, crystalline coatings on suprasil fused silica. Personal communication.

[37] G. D. Cole, P. Heu, D. Follman (CMS LLC), C. Deutsch, T. Zederbauer, and C. Pawlu (CMS GmbH). Cms inspection report, crystalline coatings on sapphire. Personal communication.

[38] Bernard Cimma, Danielle Forest, Patrick Ganau, Bernard Lagrange, Jean-Marie Mackowski, Christophe Michel, Jean-Luc Montorio, Nazario Morgado, Renee Pignard, Laurent Pinard, and Alban Remillieux. Original optical metrologies of large components. In *SPIE 5252, Optical Fabrication, Testing, and Metrology*, page 322. International Society for Optics and Photonics, 2 2004.

[39] E. Welsch and D. Ristau. Photothermal measurements on optical thin films. *Applied Optics*, 34(31):7239, 11 1995.

[40] Vincent Loriette and Claude Boccara. Absorption of low-loss optical materials measured at 1064 nm by a position-modulated collinear photothermal detection technique. *Applied Optics*, 42(4):649, 2 2003.

[41] Garrett D. Cole, Wei Zhang, Bryce J. Bjork, David Follman, Paula Heu, Christoph Deutsch, Lindsay Sonderhouse, John Robinson, Chris Franz, Alexei Alexandrovski, Mark Notcutt, Oliver H. Heckl, Jun Ye, and Markus Aspelmeyer. High-performance near- and mid-infrared crystalline coatings. *Optica*, 3(6):647, 6 2016.

[42] "Newport: Neutral Density Filter Selection Guide". https://www.newport.com/g/neutral-density-filter-selection-guide.

[43] "SHIMADZUUV-VIS-NIR Spectrophotometer Solidspec-3700 datasheet". https://www.ssi.shimadzu.com/products/literature/Spectroscopy/C101-E101D.pdf.

[44] The VIRGO Collaboration. The VIRGO large mirrors: a challenge for low loss coatings. *Classical and Quantum Gravity*, 21(5):S935–S945, 3 2004.

[45] Tevis D B Jacobs, Till Junge, and Lars Pastewka. Quantitative characterization of surface topography using spectral analysis. *Surface Topography: Metrology and Properties*, 5(1):013001, 1 2017.

[46] C. Deumié, R. Richier, P. Dumas, and Claude Amra. Multiscale roughness in optical multilayers: atomic force microscopy and light scattering. *Applied Optics*, 35(28):5583, 10 1996.

[47] S. Gras, H. Yu, W. Yam, D. Martynov, and M. Evans. Audio-band coating thermal noise measurement for Advanced LIGO with a multimode optical resonator. *Physical Review D*, 95(2):022001, 1 2017.

[48] S. Gras and M. Evans. Direct measurement of coating thermal noise in optical resonators. *Physical Review D*, 98(12):122001, 12 2018.

[49] Eric D. Black. An introduction to Pound-Drever-Hall laser frequency stabilization. *American Journal of Physics*, 69(1):79–87, 1 2001.

[50] M. Evans, S. Ballmer, M. Fejer, P. Fritschel, G. Harry, and G. Ogin. Thermo-optic noise in coated mirrors for high-precision optical measurements. *Physical Review D*, 78(10):102003, 11 2008.

[51] Yuri Levin. Fluctuation-dissipation theorem for thermo-refractive noise. *Physics Letters A*, 372(12):1941–1944, 3 2008.